Title

Dual Processing Approaches to Fabricate Nacre-like Alumina with a Metallic Compliant Phase for Damage Tolerance

Author

Wat, Amy

Publication Date

2018

Dual Processing Approaches to Fabricate Nacre-like Alumina with a Metallic Compliant Phase for Damage Tolerance

By

Amy Wat

A dissertation submitted in partial satisfaction of the

requirements for the degree of

Doctor of Philosophy

in

Engineering – Materials Science and Engineering

in the

Graduate Division

of the

University of California, Berkeley

Committee in charge:

Professor Robert O. Ritchie, Chair

Professor Mark Asta

Professor Lisa A. Pruitt

Fall 2018

Abstract

Dual Processing Approaches to Fabricate Nacre-like Alumina with a Metallic Compliant Phase for Damage Tolerance

By

Amy Wat

Doctor of Philosophy in Engineering – Materials Science and Engineering

University of California, Berkeley

Professor Robert O. Ritchie, Chair

Ceramics have great properties, such as low density, high creep resistance, and high corrosion resistance, but it fractures in a very brittle fashion. This limits the applications of ceramic materials for structural applications due to the potential for catastrophic failure. Many scientists have studied nacre, or the mother-of-pearl portion of abalone shells as an inspiration for creating a tough and strong ceramic material. It has garnered a lot of interest because its fracture toughness is 40x higher (3000x higher in energy terms) than its constituent parts, which is 95 vol% calcium carbonate and 5 vol% biopolymers arranged in a brick-and-mortar structure.

The polymer mortar phase prevents viable applications of this ceramic at higher temperatures, which is critical for applications in aerospace, nuclear materials, and transportation. In lieu of a polymeric mortar, a metallic mortar can improve the high temperature resistance of the material. Unfortunately, capillary forces prevent infiltration of metals into porous ceramics. The thesis presents a “top-down” processing approach and a “bottom-up” processing approach to overcome these capillary forces.

The “top-down” approach uses reactive wetting to infiltrate alumina scaffolds with bulk metallic glass without any added pressure. The results illustrate the effects of infiltration temperatures on the mechanical properties of the materials. The infiltration temperature affects the mechanical properties of the brick-and-mortar materials by changing the interfacial properties of the materials. At higher infiltration temperatures, the interface fails to allow for extrinsic toughening mechanisms, but it leads to significantly lower flexural strength. At lower infiltration temperatures, the material is very brittle and shows will no crack deflection or extrinsic toughening, but the flexural strength is higher.

The alternative (“bottom-up”) approach to synthesize “nacre-like” structures ceramics containing a metallic nickel compliant phase. These materials were fabricated using core-shell alumina/nickel platelets that are aligned using slip casting and rapidly sintered using spark-plasma sintering (SPS). With this process, nacre-like ceramic/metal nanostructures have been fabricated with various microstructural features. By casting NiO-coated platelets along with Ni-coated platelets and very rapid SPS processing, there was limited dewetting of the nickel mortar. As a result, we have produced a “nacre-like” alumina ceramic displaying a resistance-curve toughness up to ~16 $MPa \cdot m^{1/2}$ with a flexural strength of ~300 MPa.

To Michael Tecson,

you have emboldened me to pursue the marvelous life I was afraid to admit I wanted.

With you, I am constantly fulfilled as a human, yet hungry for more adventure.

To my family back in Los Angeles:
Mom and Dad, you are a magnificent example of ambition and a strong work ethic.
Dennis, you reached out when I needed someone to hear me and
taught me how to pursue happiness on my own terms.

Table of Contents

List of Figures

Acknowledgements

This work was only possible due to the work and the help from countless people and this section is merely the tip of the iceberg. I am a deeply fortunate person to have so many generous, intelligent people who were willing to lend me their time and give their two cents.

I must begin my expressing my gratitude to my doctoral advisor, Professor Robert O. Ritchie. Your guidance and mentorship have shown me how to be academically excellent, push for my ideas, to teach students, and be an effective mentor. My time in your lab was challenging, deeply engaging, and filled with camaraderie. You have done so much to enable me to pursue this work and I am eternally grateful for the time I spent on the various projects in your group, the wonderful conferences you have sent me, and the various connections I have built because of you. I have learned what it means to be a leader in the scientific community through your example and I plan on using these lessons in my career. I hope to make you proud and continue producing great work in the next phase of my journey.

I also must thank Dr. Antoni P. Tomsia. You have taught me so much about how to navigate the challenges around creating a bioinspired material. Our long conversations about science, life, and its various complications helped me grow as a person. Thank you for being such a valuable resource and sounding board during my graduate career.

I also want to thank my committee members, Professors Mark Asta and Lisa Pruitt, and Professor Oscar Dubon. Your guidance and advice ensured that I kept a long-term vision of my career and kept me motivated to continue pursuing scientific work. I hope I can come back to you for advice in the future.

To Dr. Jein Lee and Professor Eun Soo Park, thank you so much for your work and support through the BMG project. You were invaluable for making this project a reality. Your feedback and analysis really illuminated many key issues about the work and it was a joy to work with you.

To my collaborators, Dr. Ferraro Claudio and Professor Eduardo Saiz, your resources and expertise made the spark plasma sintering project a reality. Without your help, this work would not have been possible.

To the members of the Ritchie group, thank you so much for teaching me during my time as a student and enduring my endless questions. To Professor Bernd Gludovatz, your feedback and wealth of knowledge was crucial for me to study these materials. To Dr. Valentina Naglieri, you taught me so much about cast and processing ceramics. To Professor Claire Acevedo, thank you for working with me and teaching me how to manage multiple projects. I also want to thank Professor Hao Bai, Professor Xu Deng, and Dr. Benjamin Delattre for their processing expertise. I also want to thank Shinhoo Woo, Francisco B. Ojeda, and Andrew Sweet for their time and hard work to finish these projects. Also, to Ryan and Keli, it’s been quite an adventure.

I also want to thank James Wu, Grace Lau, and Brad Takasuka. Your support and invaluable advice at the Lawrence Berkeley National Laboratory were irreplaceable. I want to thank Ariana Castro, Daisy Hernandez, and Catalina Estrada. Their compassionate nature and dedication to supporting my academic pursuits made a major impact in this work.

Finally, to my friends and family from Los Angeles, thank you for listening to me every holiday and every time I make a reappearance in Southern California. I want to thank the many mentors I have at California State University, Los Angeles. Professors Margaret Jefferson, Trinh K. Pham, Adel Sharif, Darrell Guillaume, Stephen F. Felszeghy, and Frank A. Gomez, you have had an extraordinary impact on my life when I entered your campus. You were the first people who took me seriously when I said I wanted to pursue a doctorate degree. Now that I am nearing the end, I must express my gratitude for your impact on my life.

I want to thank my mother and father for their continuous support and their influence in my life. I cannot be happier to keep showing you what I can accomplish with the launchpad you have given me. I also want to express my gratitude to my brother, Dennis, who taught me the value of keeping calm, talking things through, and finding release through the finer things in life. Honestly, knowing you are in Southern California granted me the freedom to run off to this purely academic pursuit.

To my dear partner, Michael Tecson, you gave me the sweetest and warmest home. You kept me focused on being the best person I can be and helped me breathe through the various challenges this part of my life has presented me. Your partnership was what I needed to push myself through the finish line and gave me the chance to pursue the happiest and most fulfilling life beyond my wildest dreams and expectations.

I also must show my appreciation for the financial support that made this work possible. This work was supported by the Mechanical Behavior of Materials Program (KC 13) at the Lawrence Berkeley National Laboratory, funded by the U. S. Department of Energy, Office of Science, Office of Basic Energy Sciences, Materials Sciences and Engineering Division, under Contract No. DE-AC02-05CH11231. This material is based upon work supported by the National Science Foundation Graduate Research Fellowship under Grant No. DGE 1106400.

Chapter 1
Introduction

New materials for structural applications in industries such as aerospace, energy and transportation often have the requirement to operate safely at high temperatures in aggressive environments and, for aviation applications, to additionally have low density. Ceramic materials are an ideal solution to this problem, but their use has been severely compromised by the fact that they display near-zero tensile ductility and low fracture toughness values, which makes them prone to sudden catastrophic failure. Nature is particularly adept at designing damage-tolerant ceramic-like materials with excellent strength and toughness, despite a small palette of materials with relatively meager mechanical properties. This is possible through sophisticated hierarchical, multiple length-scale architectures that optimize the mechanical properties of the hard mineral and soft organic phases, often through the incorporation of ingenious compositional, orientation, or structural gradients and graded interfaces.[1–4] A notable example here is nacre, or the mother-of-pearl portion of abalone shells, which is known to have a fracture toughness which in energy terms is some three orders of magnitude higher than that of its constituents. Nacre is comprised of ~95 vol.% aragonite mineral (calcium carbonate) and ~5 vol.% biopolymer,[1,2,4,5] formulated into a brick-and-mortar microstructure which enables multiple toughening and strengthening mechanisms.

The brick-and-mortar microstructure facilitates the creation of damage-tolerance; in simple terms, the mineral “bricks” provide strength, whereas limited displacements a few micrometers within the biopolymeric “mortar” act to dissipate locally high stresses, thereby providing a degree of ductility that promotes toughness. The salient toughening mechanisms are principally extrinsic[6] and involve crack deflection and primarily brick pull-out leading to crack bridging.[4] The sliding behavior within the mortar is essential for toughening, but it must be limited to retain the strength.[1] It is restricted due to the presence of mineral bridges that connect the platelets[2,7], the roughness on the platelet surfaces[8], and the tensile and shear strength of the biopolymers that act as a glue between the platelets;[9] in certain organisms, tablet interlocking due to the dovetail geometry of the platelets can also play a role.[10] Nature creates optimal damage-tolerant properties by employing high-aspect mineral “bricks” with a tensile/shear-resistant “mortar”. Nature’s precise tailoring of its structures and constituents’ properties generates mechanical performance that is comparable with advanced engineering ceramics.[5] Computational models and biomimetic approaches therefore suggest that there is potential to create new lightweight structural materials with current engineering ceramics by utilizing the design principles and strength/toughening mechanisms active in nacre and other biological materials.[11–13]

A promising method to recreate nacre-like ceramics using a top-down approach is freeze-casting followed by infiltration of a compliant (mortar) phase, such as a polymer or metal.[14–16] Freeze-casting is a method of creating a porous ceramic scaffold by mixing ceramic particles in water and then freezing the water with a temperature differential to induce lamellar ice growth. Once the ice freezes, it largely repels the ceramic particles into the pores between the ice lamellae.[17] Subsequently, the ice can be sublimated leaving a porous ceramic structure in the negative image of the ice structure. This technique has been used to create ceramic materials that have complex hierarchical microstructures that can be controlled depending on the casting conditions and additives used in the solvent.[18–23] One notable example is a freeze-cast alumina scaffold that was pressed and infiltrated with PMMA as a compliant phase to mimic the nacre architecture.[14] With 80 vol.% ceramic in a brick-and-mortar structure, it displayed a strength of ~225 MPa and an extremely high toughness in excess of 30 MPa·m^{½} , making it one of the toughest ceramic materials reported to date.

Following this work, there has been sustained interest in creating ceramic structures with a nacreous microstructure, particularly as computational models have suggested that the strength of nacre-inspired ceramics could increase, without sacrificing toughness, if the polymer compliant phase was replaced by a metal.[11] This direction has the best potential to create exciting new lightweight structural materials with high strength, high toughness, and a capability for high-temperature functionality. To make such biomimetic materials, melt infiltration after freeze-casting a ceramic scaffold represents a liquid processing technique that has the potential to fabricate ceramic-metal hybrid materials with strong interfacial bonding.[24] Hybrid ceramics with a lamellar structure have been fabricated by pressure-assisted infiltration with conventional Al alloys,[25,26] but those contained less than 40 vol.% of alumina ceramic, which is significantly lower than the mineral content in nacre. A conventional melt infiltration process requires a complex experimental setup to apply pressure on the melt. Furthermore, as the volume fraction of reinforcement increases and the pore spacing decreases in a scaffold, the pressure required to completely infiltrate the scaffold increases, leading to deformation or cracking of the scaffold.[27,28] Since the magnitude of the applied pressure is closely related to the wettability of the ceramic by a molten alloy, strategies such as the addition of a reactive element in the matrix alloy or coating the surface of reinforcements have been applied to improve the wettability and therefore feasibility of infiltration between the alloy and ceramic.[27] For example, recently Mg was used as a reactive element to fabricate bio-inspired hybrid materials using pressureless infiltration,[29] but the microstructure was lamellar with a low ceramic content compared to the brick-and-mortar structure.

In this dissertation, I describe two processing approaches to create a bioinspired ceramic material with a metallic compliant phase. I delineate between the two as a “top-down” and “bottom-up” processing approach with the same goal of creating a ceramic material with high damage tolerance.

In the top-down processing approach detailed in Chapter 3, we use reactive wetting to create a nacre-like, high volume fraction ceramic material containing a metallic compliant phase. We selected a Zr-based bulk-metallic glass (BMG) as the mortar phase as this alloy shows excellent wettability with alumina.[30,31] Zr-based BMGs have been shown to have high strength with some degree of toughness, which represent ideal properties as a compliant-phase (mortar) material. As a result, the combination of perfect wettability and mechanical properties of the BMG makes it an interesting candidate for infiltration into a brick-like ceramic scaffold. However, processing of BMGs can be difficult because they are prone to oxidation at elevated temperatures[32] and have a critical cooling rate required to solidify in the amorphous state; moreover, the final material must be used below the BMG’s glass-transition temperature as these glasses can embrittle if they are allowed to crystallize.[33] While fibrous or particulate BMG matrix composites have been developed by melt infiltration,[34,35] this study relates their their infiltration behavior to the thermo-physical properties and wettability of the BMG. This can be used to tailor the properties of the ceramic/metal interfaces while maintaining the BMG in the fully amorphous state as a metallic mortar in nacre-like material.

In this study, we demonstrate the synthesis of alumina-glass ceramics with nacre-like (high volume fraction) alumina scaffolds using pressureless infiltration. Infiltration behavior, investigated from contact-angle measurement and electrostatic levitation, was used to indicate that the length-scale of the scaffolds and the excellent wettability of a ceramic with a liquid alloy are crucial factors to warrant the successful synthesis of these materials. Near-perfect wetting within seconds for the Zr-based BMG on alumina was achieved, indicating that a conformal bond can be attained at the interface of the two materials, which in turn implies high strength may be realized in an Al_2O_3/BMG hybrid material.[36,37] However, depending upon the infiltration temperature, after solidification of the metallic phase, the interfacial strength can markedly change due to the formation of brittle interfaces, which can potentially compromise strength and toughness of the processed material. Accordingly, in addition to describing the processing of brick-and-mortar, high volume fraction (~80 vol.%) alumina containing a metallic compliant phase, we examine how processing conditions can affect the ceramic-metal interfaces in order to discern the fundamental mechanisms underlying the flexural strength and fracture toughness of these bioinspired nacre-like ceramics.

However, freeze-cast materials have an upper limit of approximately 80 vol.% ceramic, which is a very low ceramic content compared to the ceramic content of its natural counterpart at 95 vol.%. The objective of the bottom-up processing study in Chapter 4 is to an develop alternative processing procedure that can make lightweight structural materials in the form of alumina with a fine-scale nacre-like brick-and-mortar structure, consisting of 90 vol.% or more ceramic with a metallic nickel compliant (mortar) phase.

The alternative "bottom-up" processing approach used alumina platelets, which were modified by coating the surfaces of the platelets with a nickel-based precipitate[38], to form the building blocks. Nickel is an ideal metallic mortar because of its high melting point along with good strength and ductility. The alumina platelets were coated with nickel or nickel oxide before the nacre-like structure was built using these core-shell nickel/alumina platelets. Then, using slip casting and spark-plasma sintering, well-aligned core-shell platelets microstructure were achieved. While a similar approach has been used to create materials with a nacre-like structure[39], the toughness in these materials are an order of magnitude lower than the materials we report in this paper. This is potentially caused by limited bonding strength between the ceramic and metallic phase. We focus here on the optimal sintering temperatures and sample composition to create materials with a strong interphase between the ceramic and metal, in order to develop advanced ceramics with high toughness and acceptable strength for structural applications.

Chapter 2
Background

SECTION 2.1. MECHANICAL PROPERTIES OF ENGINEERING MATERIALS

The scientific community is very interested in developing new materials that is tough, strong, and withstands high temperatures. Strength describes a material's capability to withstand a force without any deformation or shape change. It is measured using the force required to deform a material with a measured cross-sectional area. Fracture toughness describes a material's capability to resist crack propagation using a measure of the energy required for the material to completely fail. Most engineering materials display a tradeoff between toughness and strength, as illustrated in Figure 1. Metals tend to have high toughness, but relatively low strength and low temperature resistance. Ceramics have high strength and are stable at high temperatures; however, they have low toughness. As a result, ceramics tend to fail catastrophically. Scientists and engineers are interested in improving the toughness of ceramics to create an exciting new structural material with potential applications in nuclear energy, turbines, engines, and armor. Past efforts did not manage to break the strength and toughness tradeoff, but there has been renewed interest.

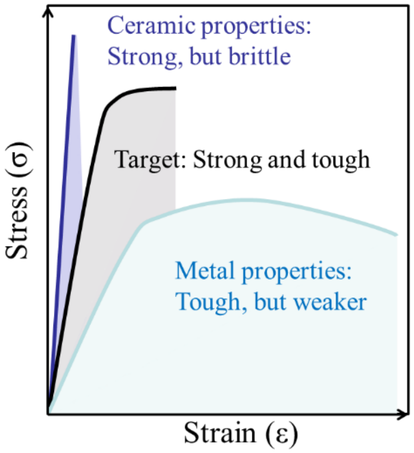

Figure 1: General properties of structural engineering materials

The cause of this tradeoff between strength and toughness is the deformation mechanisms found within the two different classes of materials. Crystalline metallic materials can undergo limited deformation due to metallic bonds whose directionless nature enables dislocation motion. This dislocation movement allows local dissipation of high stresses which results in higher fracture toughness and higher ductility before fracture. Due to this dislocation movement, metallic materials generally display lower strength compared to ceramics. However, ceramic materials are formed through a combination of highly directional ionic and covalent bonds, whose higher bonding energy leads to higher strength, but does not enable dislocation motion. As a result, its fracture toughness is low and it fails in a very brittle fashion. However, there are methods to impart fracture toughness in brittle materials that do not require ductility.

In order to consider how to impart damage tolerance in a brittle material, it is helpful to consider different mechanisms that affect strength and fracture toughness. These can be sorted into two categories called intrinsic toughening and extrinsic toughening. Intrinsic toughening is how ductile materials develop fracture toughness through plasticity and dislocation motion at the crack tip to resist crack propagation. Extrinsic toughening is how brittle materials can develop fracture toughness because it uses a wide variety of different microstructural features at the wake of the crack to reduce the local stresses and strains at the crack tip. Monolithic ceramic materials have used grain bridging, transformation toughening, and oxide wedging. The major difference between intrinsic and extrinsic toughening is that intrinsic toughening operates ahead of the crack tip and extrinsic toughening occurs behind the crack tip, as illustrated in Figure 2.

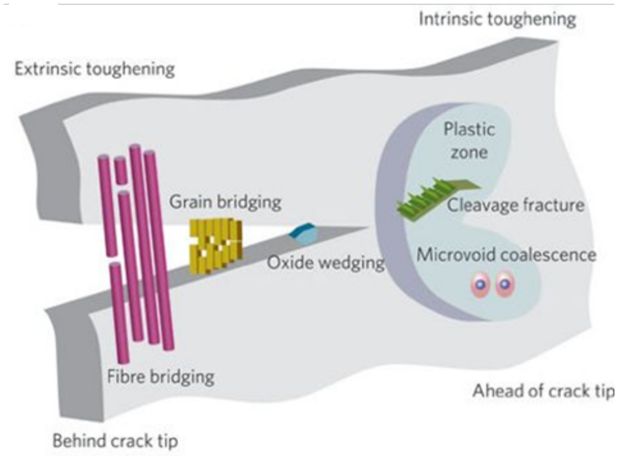

Figure 2: Illustration of extrinsic versus intrinsic toughening in materials

This has major effects on how to study the fracture toughness of ductile versus brittle materials. Intrinsic toughening mechanisms found in ductile materials can improve fracture toughness at the initiation and propagation of a crack. Extrinsic toughening mechanisms do not affect the inherent fracture toughness of the material and can only be effective once a crack appears. As a result, extrinsic toughening mechanisms found in brittle materials have no effect on crack initiation and is very dependent on crack length. Brittle materials display fracture toughness through rising crack-resistance curves, which characterize how extrinsic toughening mechanisms ensure stable, subcritical crack growth by increasing the required crack-driving forces in order to propagate a crack through the material. An example of rising R-curve behavior compared to catastrophic, unstable crack growth behavior is shown in Figure 3.

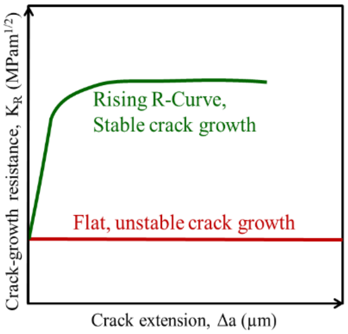

Figure 3: Comparison of stable, rising r-curve behavior compared to catastrophic crack growth

Extrinsic toughening is a critical mechanism to break the strength and toughness tradeoff found in modern structural materials. Intrinsic toughening is the primary mechanism to impart damage tolerance in ductile materials, but it forces them to display this strength and toughness tradeoff. If the metallic material has high strength, then there is less dislocation mobility and therefore plasticity for intrinsic toughening. However, extrinsic toughening only occurs at the wake of the crack and does not affect the inherent properties of the material. As a result, well-designed microstructural features can impart this increase in fracture toughness without impacting its strength. This strategy to designing new materials have been thoroughly studied in monolithic and composite ceramic materials.

Typical extrinsic toughening mechanisms include transformation toughening, crack bridging, crack deflection, and crack wedging. These mechanisms can impart modest increases in fracture toughness in monolithic ceramic materials. For example, crack deflection and crack bridging can elevate the fracture toughness of silicon carbide (SiC) from ~2 $\mathrm{MPa{\cdot}m^{1/2}}$ to 10 $\mathrm{MPa{\cdot}m^{1/2}}$. Transformation toughening is known to improve the fracture toughness of zirconia from 1.1 $\mathrm{MPa{\cdot}m^{1/2}}$ to up to 9 $\mathrm{MPa{\cdot}m^{1/2}}$.[40] However, these increases in fracture toughness is rather meager compared to the increases in fracture toughness found in natural materials. Natural materials have mastered extrinsic toughening by developing sophisticated, hierarchical microstructures that can generate multiple extrinsic toughening mechanisms to relieve locally high stresses. As a result, materials such as nacre, or the mother-of-pearl portion of mollusk shells, displays a 40-fold increase in fracture toughness, compared to the nine-fold increase found in man-made materials. Therefore, natural materials make ideal inspirations for the design of new ceramic materials.

SECTION 2.2. HISTORY AND PROGRESS OF NACRE-INSPIRED MATERIALS

The scientific community has realized that nacre, or the mother-of-pearl portion of abalone shells, can be used as inspiration to create a new composite material due to a brick-and-mortar microstructure it possesses, as shown in Figure 4.[14]

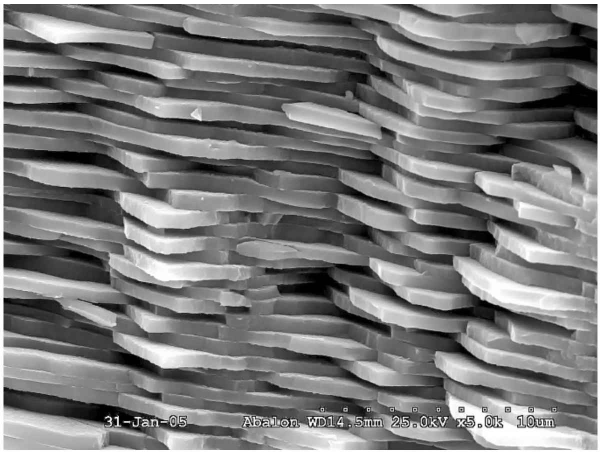

Figure 4: Brick-and-mortar microstructure of nacre[14]

Nacre being used as inspiration for new materials started with John D. Currey's study on the tensile strength of nacre.[41] He conducted this work during his time as a professor in University of York, England. In this work, he studied the tensile (as opposed to compression) strength of mother-of-pearl, which inspired an interest in the other mechanical properties of the material. At the time, he pointed out that the majority of the material is formed by plates of aragonite, which is essentially chalk, arranged in sheets that are held together by a protein, as shown in Figure 5.[41] Despite being made of these materials with meager mechanical properties, it displays a wide variety of strengths and a curious method to prevent cracks from fracturing the material. However, he never tested the materials for fracture toughness because he was a biologist, rather than a materials scientist or mechanical engineer. As a result, his understanding of the various properties necessary to get a quantitative number to characterize the material was limited. Subsequent papers from Currey reports other mechanical properties, but he tested the materials for their tensile properties, even though most of the stresses the material would experience would be in compression or bending. Future tests with these materials tend to measure their properties when bent. Nonetheless, the paper ignited interest in testing biological materials for mechanical properties.

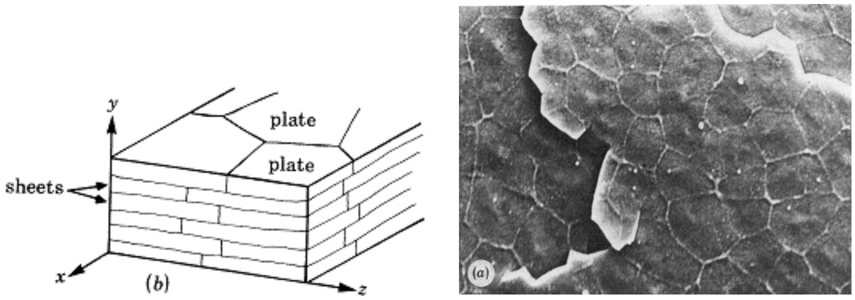

Figure 5: Microstructure of nacre as sheets[41]

It was not until 1990, when the fracture toughness of nacre was measured by Mehmet Sarikaya, who was trained as a materials scientist. He published a paper that measured both the strength and fracture toughness of nacre. This work highlighted how despite the fact that nacre was composed of 95 volume percent of calcium carbonate and 5 volume percent polymers, nacre displayed mechanical properties that made it comparable with many engineering ceramics that were used at the time, as shown in Figure 6.[5] The paper suggested using the microstructure of nacre as inspiration for a new composite material. However, he did not introduce a full understanding of what mechanisms allowed for this composite material to be tough and strong. With this gap in knowledge, there were many efforts in explaining what mechanisms and structural features enabled these properties in nacre.

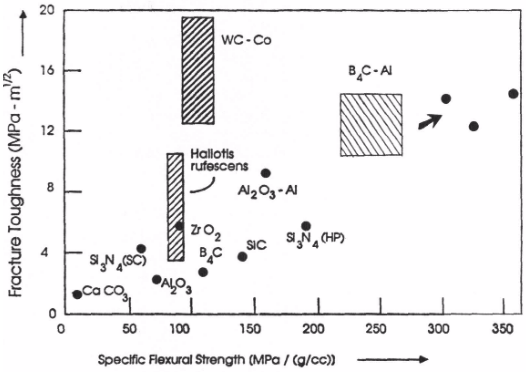

Figure 6: Comparison of nacre properties to engineering materials[5]

There are four mechanisms that are known to play a role in the remarkable mechanical properties of nacre. The mechanisms are listed below in Figure 7.[1] They are the mineral bridges that connect the platelets, surface roughness and platelet geometry that prevents platelet sliding, and the properties of the polymers that hold the platelets together. The discoveries are discussed in chronological order in this chapter.

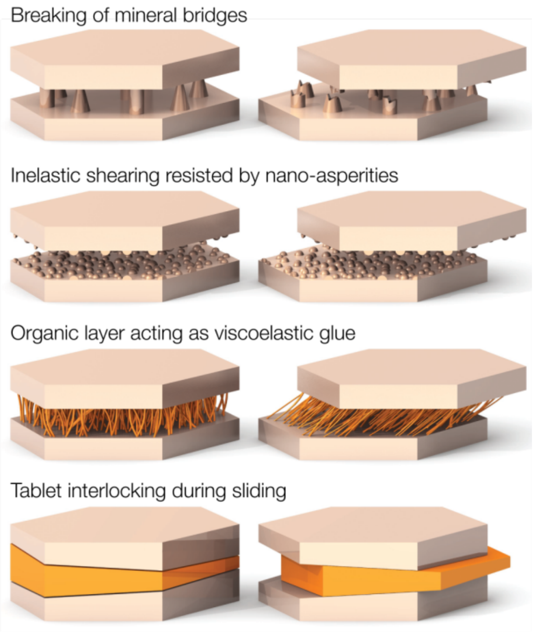

Figure 7: Nacre toughening mechanisms[1]

In 1999, Bettye L. Smith and Tilman E. Schäffer from University of California, Santa Barbara and the Max-Planck Institute, respectively, worked together to prove that the unique properties of the polymer contribute to the mechanical properties of the material. The polymers were structured in loops that become unwound in "steps".[9] This is modeled in Figure 8 using the load-extension curves. It demonstrates that the modules combine the traits of the short and long molecule to create a material that must experience a higher force in order to extend farther.

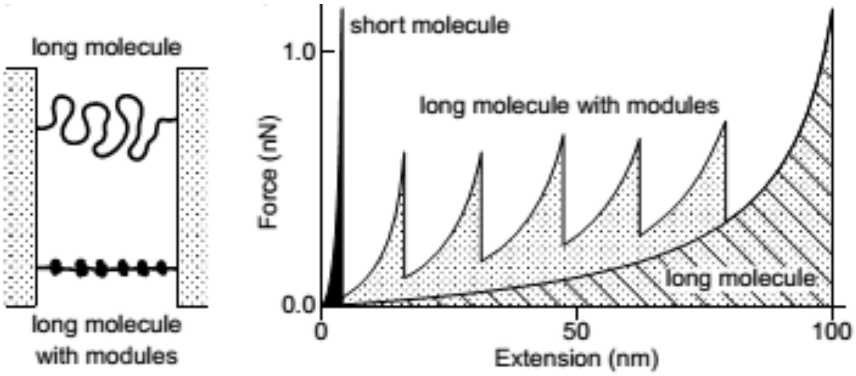

Figure 8: Model of polymer in nacre[9]

Another mechanism that has been attributed to give the structure its properties was found in 2001 by Anthony G. Evans, who was at Princeton University at the time. He posited that another factor that led to the mechanical properties of nacre is the surface roughness on the platelets found on nacre. This roughness makes it difficult for the platelets to slide. This was proven using computer simulations with the finite element method.[8]

The next breakthrough in understanding the mechanisms involved in improving the mechanical properties of nacre came two years later, when Fan Song from the Chinese Academy of Sciences published his scanning electron microscopy and transmission electron microscopy results that prove that the platelets have bridges that connect them together.[7] The results are shown in Figure 9 below.

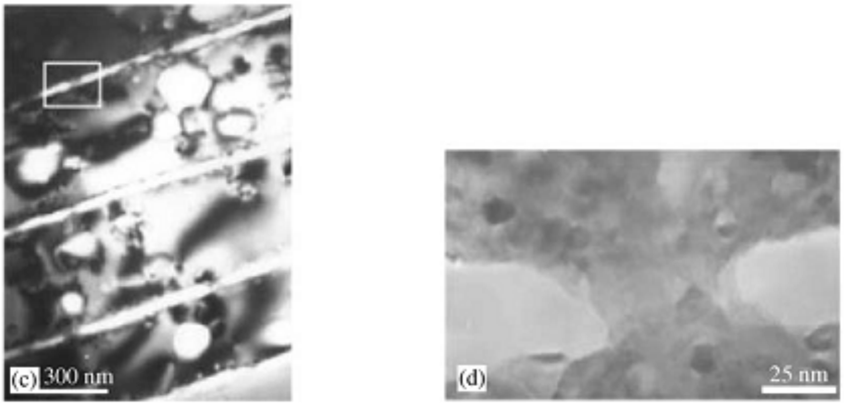

Figure 9: Evidence of nacre bridging between platelets[7]

One recent breakthrough in gaining a mechanistic understanding of the microstructural features was in 2011, where Francois Barthelat, who was at Northwestern University at the time, pointed out that the platelet geometry have a "wavy" structure.[42] The platelet shape prevents them from sliding past each other. This was found using scanning electron microscopy (Fig. 10) and imitated using a series of bolts and acrylic "bricks". Barthelat and his collaborator, Horacio D. Espinosa, submitted and was awarded a patent for nacre-based composites.[43]

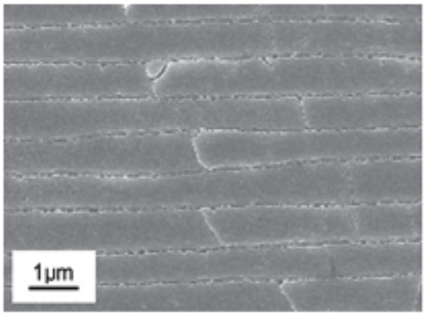

Figure 10: Dovetail shapes of nacre platelets[42]

With this understanding of the mechanisms to impart damage tolerance, there have been many efforts in recreating the material. In some literature reviews on the field, the techniques have been split between bulk materials and coatings. The difference between these distinctions is how thick the material grown is and how likely it can be a free-standing material. The two types and the techniques associated with each are shown in the flow chart below in Figure 11.[44]

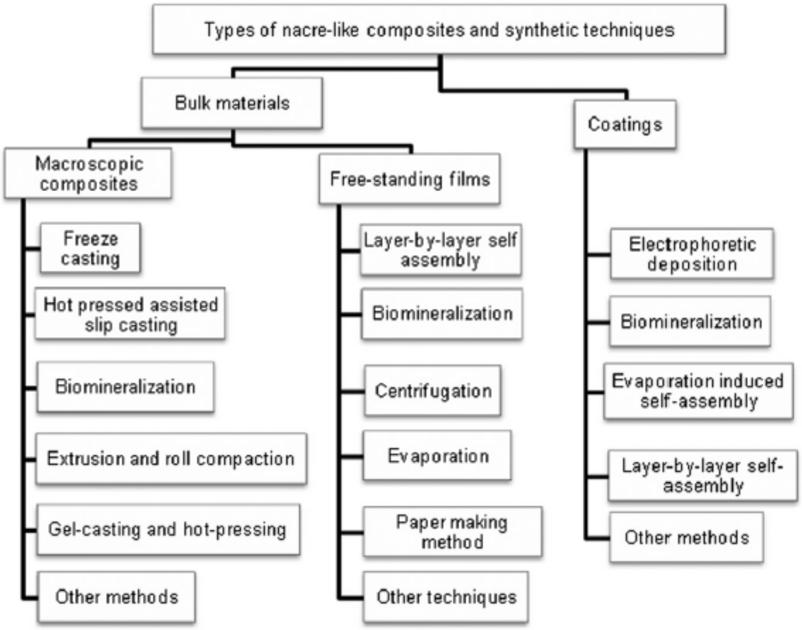

Figure 11: Flowchart of processing techniques for nacre-inspired materials[44]

One promising method to recreate the material was through freeze-casting. The technique was used to create a material that demonstrated many of the mechanisms for nacre toughening listed above. The material displayed a fracture toughness that defeated the rule-of-mixtures. The rule of mixtures is a general rule used to predict the potential upper and lower bounds for a composite material's properties based on its constituent parts. This material had a relatively high strength and toughness. When compared to other engineering materials, it was considered to be the toughest material ever made.[14] This is considered to be the most promising technique because it also created a rather large-scale laboratory sample and its processing technique is very scalable and flexible compared to many other methods used.

Freeze-casting is a method of creating a porous ceramic scaffold by mixing ceramic particles into a suspension and then freezing it with a temperature gradient to induce lamellar ice growth. Once the suspension freezes, it repels the ceramic particles in the pores between the ice lamellae. Then, the ice is sublimated away to leave a porous ceramic scaffold that is a negative image of the ice. The scaffold is used as the base to create the ceramic platelets in a nacre-based composite. Figure 12 is a diagram attached below to explain how freeze-casting physically works.[45]

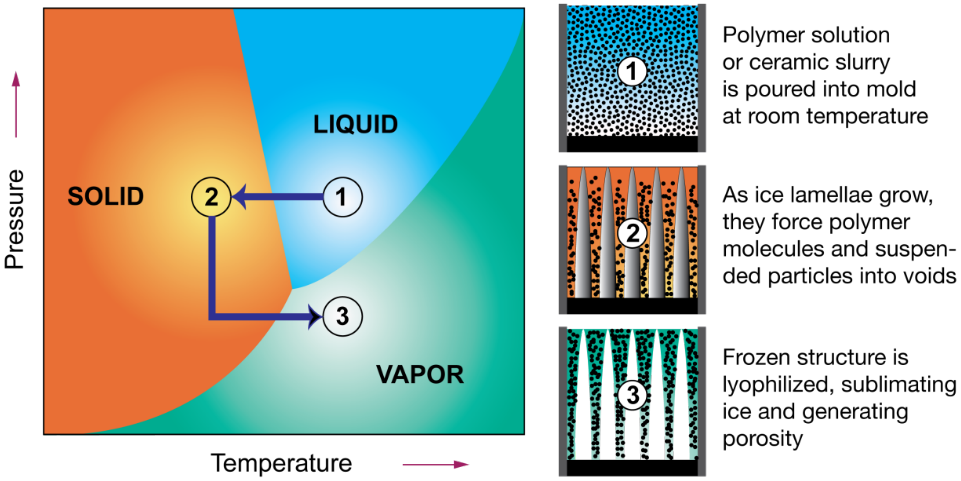

Figure 12: Freeze-casting diagram emphasizing the various phases of water that enables freeze-casting.[45]

After this material was developed, there was work in creating a material that would withstand higher temperatures. The material was made with alumina, which is an engineering ceramic, and acrylic. The acrylic melts too quickly for high temperature applications. Therefore, there was interest in creating a ceramic/metal composite with the same microstructure. The group progressed with creating a composite with alumina or aluminum oxide as the platelet phase and aluminum-silicon as a metallic mortar phase in 2009.[25] Unfortunately, due to the physical reality of infiltration of metals into ceramics, it is difficult to create a material that perfectly mimics nacre. Molten metal does not readily wet ceramics, which means that the liquid-liquid molecular interactions are much more favorable than the liquid-solid molecular interactions. Therefore, to infiltrate the materials, unfeasibly high pressures must be applied for infiltration to occur. Therefore, the material was only 40 volume percent ceramic (Fig. 13), as opposed to the 95 volume percent ceramic found in the nacre microstructure.

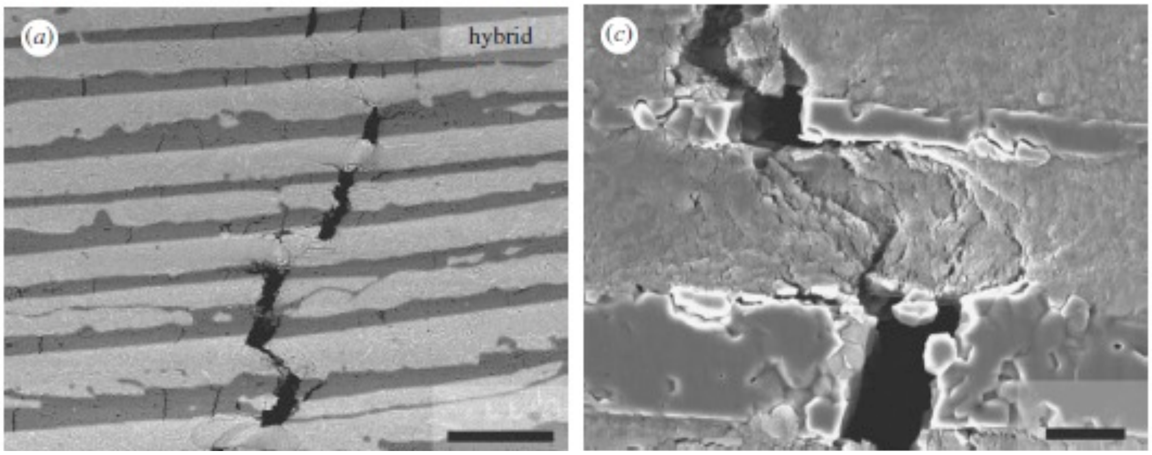

Figure 13: Ceramic/metal composite with a 40 volume percent ceramic created using melt infiltration of aluminum-silicon alloy into freeze cast alumina[25]

Despite these issues, there is sustained interest in creating a ceramic-metal composite because recent computational models from Matthew R. Begley from University of California, Santa Barbara suggest that the strength of nacre-inspired composites would increase, without sacrificing fracture toughness, if the polymer component of the composites were replaced with a metal.[11] The data is graphed below in Figure 14. In the first chart, it shows that the stiffness of the material will remain constant, but the failure to work, which is a primitive measure of toughness, would increase. In the second chart, it shows that the toughness would remain constant, but the strength would significantly increase with a metallic component in the composite. As a result, this direction has the best potential to realize the ideal material with high temperature resistance, strength, and toughness.

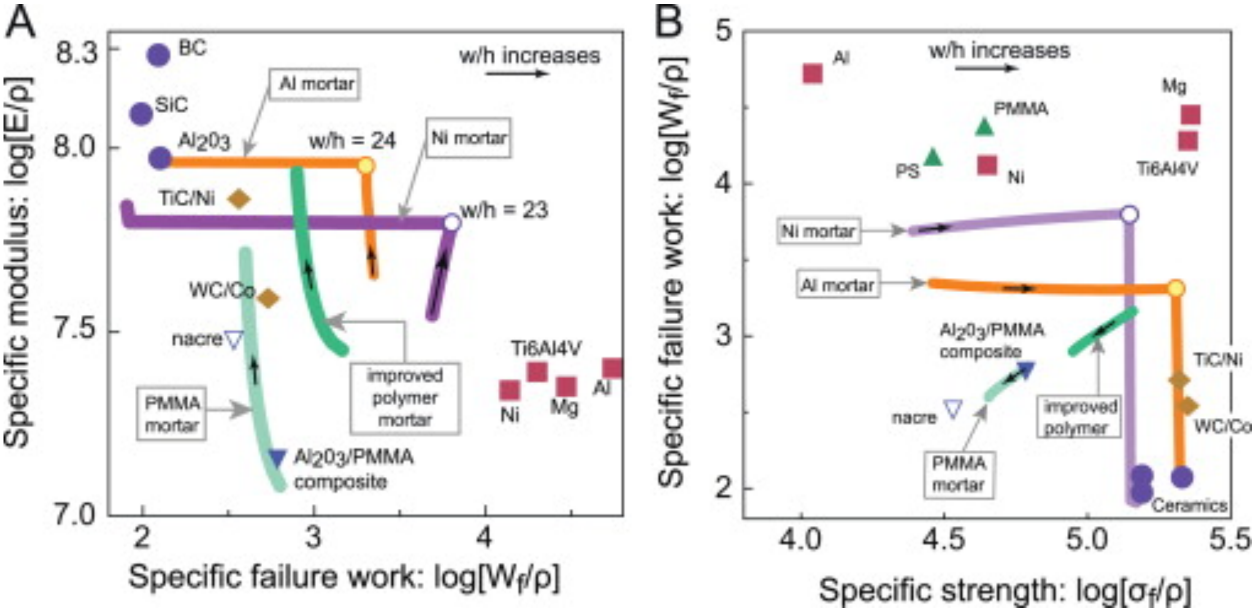

Figure 14: Results of computational work indicating how specific strength and specific toughness increases when using a metallic mortar as opposed to a polymer mortar[11]

The dissertation discusses two techniques to create nacre-like ceramics with a metallic compliant phase.

SECTION 2.3. INFILTRATION OF POROUS CERAMIC USING MOLTEN METAL

There is interest in creating a ceramic/metal composite with this microstructure since the ceramic phase will impart its high strength and the ductile metal phase along with the microstructural toughening mechanisms will substantially increase the toughness of the material. However, there are many challenges in mimicking the microstructure as a metallic matrix composite.

Many ceramic metal-matrix composites are formed by infiltrating porous ceramics with molten metals. Infiltration is advantageous for ceramic metal-matrix composites because it has the potential for near-net shape production. However, many issues arise due to poor wetting of the molten metal on ceramics. This is particularly true for brick-and-mortar materials, which can have pores that are less than a micron wide. They are typically addressed by studying the interfacial forces that affect the wettability of molten metals and capillary phenomena during wetting. By studying the interface of the ceramic/metal composite, the critical processing parameters necessary to infiltrate the samples can be found. Different processing parameters of infiltration can be manipulated to account for the different capillary and fluid-drag forces that occur during infiltration. For example, the initial composition and morphology of the ceramic or metal can be manipulated to aid in wetting by instigating a reaction at the ceramic/metal interface. Another commonly used processing parameter is the temperature and external force applied to the system to aid infiltration. The external force is particularly interesting because it is critical for infiltration of nonreactive metals.

To characterize the ceramic/metal interface, the sessile drop experiment is a standard method used to measure interfacial bond energies. It provides a good means to measure the time the system takes to reach equilibrium during reactive infiltration, which is critical for infiltration kinetics. However, this technique does not provide any information about capillary forces. It is also unsuitable for substrates that are not flat and large. The information it produces is very limited in terms of melt infiltration. Therefore, other techniques and models have been developed to analyze capillary pressures.

One such technique uses the slug-flow assumption to measure infiltration rates. This type of analysis assumes that infiltration occurs similarly to a liquid in a straight capillary tube. This means that there is a gradient in saturation in the infiltration direction due to the curved menisci of the infiltrating liquid surface. As a result, there is a pressure difference between the infiltrating phase and the unfilled phases. [46] This simplifies the system because pressure boundary conditions and thermodynamic analysis is sufficient for characterizing capillary phenomena during infiltration. Wetting is described using the Young-Dupree equation. The wetting angle is then related to the capillary pressure drop using energy balance. The capillary pressure drop is the difference between the pressure in the fluid phase immediately behind the infiltration front and the pressure in the unfilled solid phase. Therefore,

$$\Delta P_\gamma = \frac{A_v \gamma_{ma} \cos\theta}{(1 - V_f)}.$$

where ΔP_γ = capillary pressure drop,

A_v = area of ceramic/metal inferface per unit composite volume

γ_{ma} = surface energy of metal/air interface

θ = contact angle of metal/air interface

V_f = solid volume fraction [46].

This equation can be used to asses the wettability of a liquid in a porous solid because if $\Delta P_\gamma < 0$, then it is a wetting system. If $\Delta P_\gamma > 0$, then it is a non-wetting system. Also, assuming $\cos\theta \approx 1$, then the importance of capillary phenomenon of infiltration can be measured by comparing the surface tension of the liquid matrix. Based on this assumption, it is clear that the effects of capillary phenomenon are much more pronounced for metal-matrix composites as opposed to polymers because molten metals have stronger interatomic bonds compared to polymers, whose behavior is governed by weaker Van der Waals bonds. These assumptions are experimentally verified since pressure drop of molten metal with non-wetting conditions is near 1 MPa as opposed to polymer matrixes, which has values in the kPa scale. Therefore, this assumption is very suitable for analyzing and comparing capillary phenomenon between different systems. However, this assumption is not an accurate representation of infiltration into a porous ceramic because it does not take into account the different pressures across the various, irregularly shaped pores. The slug-flow model assumes that a single pressure difference can represent all of the pores of a scaffold.

A more rigorous approach to measure infiltration rates and capillary pressures in a porous ceramic is the Brooks–Corey correlations that is used in soil science.[47] The flow is assumed to be saturated, which means that that are bubbles of air trapped in the pores or the pores are not completely filled in areas where the infiltration front has passed. As a result of this assumption, infiltration proceeds over a range of pressures, as opposed to the single pressure difference that is used in the slug-flow model. Due to mass conservation, change in the volume of fluid passing through a cross sectional area of the porous ceramic per unit time (v_o) with respect to length has the same value as the local liquid volume fraction (V_l) change with respect to time. This statement is expressed mathematically below.

$$\frac{\partial v_o}{\partial x} = -\frac{\partial V_1}{\partial t}$$

The Boltzman transformation can be used to find the relationship between the dimensionless infiltration front kinetic parameter (F) and dimensionless applied pressure (p). Assuming the system is a unidirectional infiltration that is driven by a constant pressure, it can be described as:

$$\varphi = \frac{x}{\sqrt{t}} \ ,$$

where x is length in one dimension and t is time in seconds.[48]

This equation can be solved using the conservation of mass equation above, Darcy's law (expressed below), and the position of the infiltration front for a system with a constant total pressure differential (ΔP_T). These terms are expressed using the permeability of the ceramic scaffold (K), viscosity (η), local gradient pressure in fluid (∇P), and volume fraction of the solid (V_s).

Darcy's law:

$$v_o = -\frac{K}{\eta} \nabla P$$

Position of the infiltration front for $x=L$:

$$L^2 = \frac{2Kt}{\eta(1 - V_s)} (\Delta P_T - \Delta P_\gamma)$$

The combination of these equations leads to the governing equation:

$$\varphi = \frac{\mathrm{d}\left[-2 \frac{K}{\eta} \frac{\mathrm{d}P}{\mathrm{d}V_l} \frac{\mathrm{d}V_l}{\mathrm{d}\varphi}\right]}{\mathrm{d}V_l} \ .$$

This governing equation is solved using a combination of boundary conditions and prior information about $V_l(P)$ and $K(V_l)$. These are found using the Brooks–Corey correlations. For systems with a wetting angle less than 90°, the correlation is:

$$S_l = \frac{V_l}{1 - V_s} = 1 - \left(\frac{P_b}{P}\right)^{\lambda}$$

and

$$K = K_{sat} S_l^2 \left[1 - (1 - S_l)^{\frac{(2+\lambda)}{\lambda}}\right].$$

This indicates that liquid saturation S_l is a function of pressure P, the pressure when the liquid begins penetrating the ceramic (P_b), and the variability of the pore size (λ). For most experimental conditions, the λ is typically near two since smaller values indicates higher pore size variability. The permeability of the porous scaffold is dependent on liquid saturation and the permeability of a fully saturated scaffold (K_{sat}). The correlations for liquid saturation and permeability can be substituted into the Boltzman transformation and integrated once to obtain a solution for find the infiltration front position. The results of this calculation is formulated and plotted below (Fig. 15), where φ_{front} is the value of φ at the tip of the liquid front.

$$F = (\varphi_{front})^2 \frac{(1 - V_s)\eta}{2K_{sat}P_b}$$

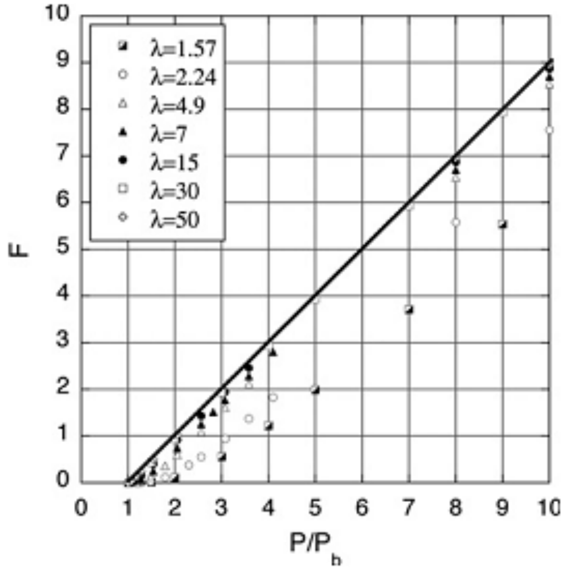

Figure 15: Adimensional infiltration front kinetic parameter *F* as a function of *P/P*$_b$, for various values of *λ*.[48]

The dark line in the figure above represents the infiltration parameters analyzed using the slug flow assumption. When the variability of pore sizes is accounted for in the model using the Brooks–Corey correlation, the system parameters have a nonlinear portion of the curve. Since a large proportion of the curve is linear, it is possible to extrapolate a relationship between the pressure and infiltration velocity if a large range of applied pressures are studied, but this extrapolation will not be accurate for lower pressures because the relationship between *F* and *p* is nonlinear. This is nonlinear region of the figure is particularly interesting for reactive wetting, where infiltration can occur without any added pressure.

Measurements of capillary pressure drop using the slug-flow assumption do not reflect the conditions of infiltration kinetics because it is highly dependent on perfect saturation of the ceramic scaffold. Perfect saturation of the ceramic scaffold is not possible when the capillary pore sizes vary, which leads to a wide range of pressures. Therefore, the Brooks–Corey correlations must be used to analyze the system because it assumes that there is unsaturated flow. In order to use Brooks–Corey effectively, the experiment must include data for the lowest pressure possible at P_b and high-pressure infiltration to get a complete description of capillary flow and wetting within the infiltration process.

While pore size, saturation, and pressure play a crucial role in infiltration kinetics, a more controllable and critical parameter that can be used to infiltrate ceramics are the compositions of the ceramic and metals. The composition of the samples control the wetting angles of the sample, which affects the applied pressure necessary to facilitate infiltration. Wetting angles are largely affected by any interfacial interactions between the molten metal and the porous ceramic. These interfacial interactions will be categorized as reactive and nonreactive systems. In nonreactive systems, the ceramic/metal interface does not undergo any transformations or reactions. These systems tend to have poor wettability, making it difficult to infiltrate samples. In reactive systems, the ceramic/metal interface reacts to form a new layer in between the ceramic/metal interface. This typically can aid infiltration, but it can also backfire and transform the metallic or ceramic phase into a material with undesirable properties. Therefore, there is a strong interest in studying interfacial reactions to tailor the resulting composite properties and promote infiltration of the molten metal into the porous ceramic.

To study interfacial reactions during infiltration, the system is characterized using the change in free energies at the interface. One variable used to study this system is the surface energies, labeled with σ and a subscript that will indicate which surface is being studied. The variable of highest concern is the work of adhesion, W_a. Work of adhesion is the sum of the surface energies of the metal/vapor interface and the ceramic/vapor interface subtracted by the surface energy of the ceramic/metal interface. This is expressed mathematically below. The larger W_a is, the more thermodynamically likely it is to spontaneously form a composite.

$$W_a = \sigma_{CV} + \sigma_{MV} - \sigma_{CM}$$

For nonreactive systems, there are slight differences in wetting behavior depending on what type of ceramic system is being investigated. In this chapter, oxide ceramic scaffolds will be studied in nonreactive systems. For an oxide ceramic scaffold, wetting is very poor. However, the kinetics of the interfacial interaction is very rapid because the system reaches equilibrium at the order of 10^{-3} seconds.[49] There are multiple proposed models of what bonds a nonreactive metal and an ionocovalent oxide. It has been proposed that the only possible type of interaction between metal and oxide is in the form of physical, Van der Waals interactions from dispersion [49]. However, Li has also been proposed that interfacial bonding of nonreactive metals and ionocovalent oxides are caused by electron transfer between the valence bands of the oxides and the metals [50]. He supported this argument by comparing the work of adhesion of the metal/oxide system using the electron density of the metal and the concentration of holes in the oxide valence band. Based on this study, the wetting properties of oxides with liquid metals are correlated to the energy bandgap of the oxide. This is illustrated in Figure 16. [50]

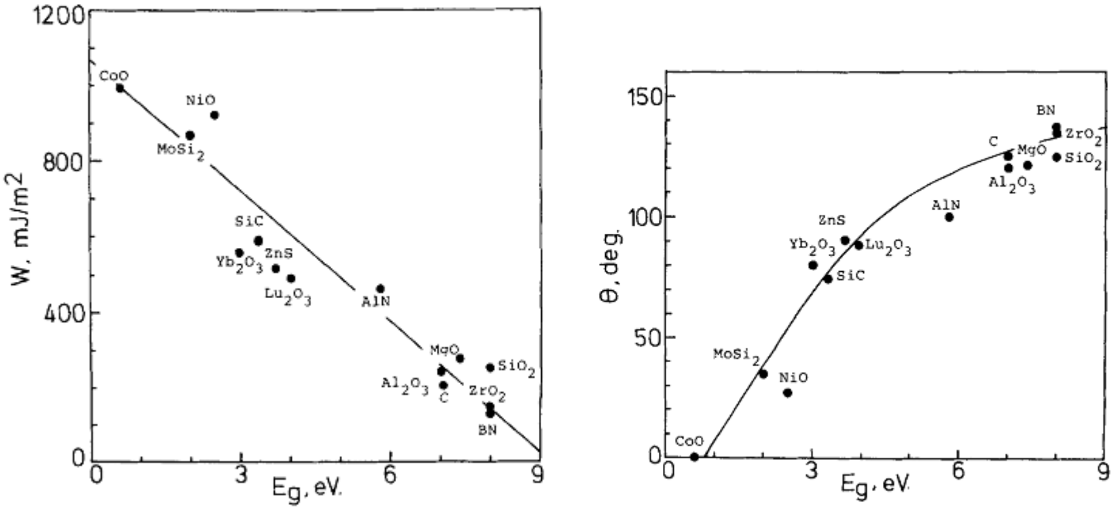

Figure 16: The work of adhesion W and the contact angle θ of liquid tin on various solid ceramics against the bandgap energies E_g of the corresponding solids.[48]

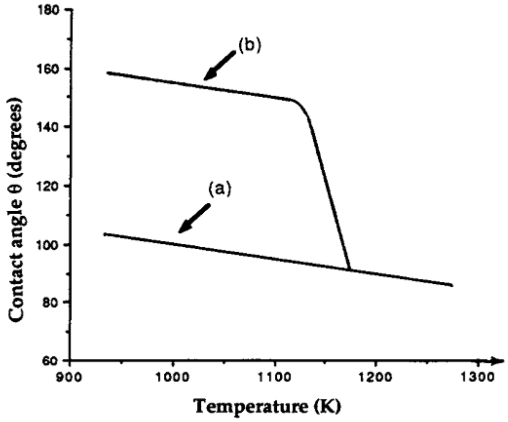

Figure 17: Schematic variation with temperature of the contact angle measured on a flat substrate for pure aluminum on alumina for two vacuum levels. (a) $P=10^{-5}$ Pa and (b) $P=10^{-3}$ Pa. The difference between the two curves arises because of an oxide layer covering the metal at higher pressures. At 1150 K, the oxide layer evaporates, which causes curve (a) to join curve (b). [48]

The addition of oxygen gas during infiltration can improve wetting in metal/oxide systems. Dissolution of oxygen gas into the liquid metals increases its wettability of oxides. [49] This is effective at concentrations as low as a few tenths of ppm. One possible explanation of the phenomenon was the oxygen that is dissolved into the metal can form bonds with the metal atoms to form small ionic clusters in the liquid. This ionic character leads to charge transfer between the metal and oxygen atoms, which as discussed in the last section, can improve wettability of the molten metal. The effectiveness of the addition of oxygen gas during infiltration is shown in Figure 17.[49]. It is clear from this example that instigating a reaction at the ceramic/metal interface is an effective method of increasing wettability.

Typically for nonreactive metal infiltration, pressure is applied to the system during infiltration to force the metal into the ceramic. Since metal does not readily wet ceramic, the mechanical force is necessary to overcome the capillary forces, but it is also used to decrease processing time and control chemical reactions. The pressure is applied using either an inert gas, such as argon, or using the piston of a hydraulic press. The gas driven processes can apply forces from 1 to 10 MPa. However, the applied pressures are limited by safety concerns. [49] A hydraulic press can apply forces from 10 to 100 MPa. Therefore, it can be very promising for creating ceramic/metal composites because this technique can form a pore-free matrix. However, the high pressures can damage the ceramic phase during infiltration. [49] While external forces can be used to overcome capillary forces during infiltration, the solution introduce safety issues and potential damage the ceramic phase of the composite, making it infeasible for fabricating ceramic/metal composites with an ordered microstructure. Therefore, there is interest in modifying the wettability at the ceramic/metal interface to manipulate of the kinetics of infiltration.

Reactive wetting is a process where the interface of the materials transforms to another product. Ideally, this would aid wetting and infiltration into a scaffold. Reactive wetting has some very significant differences to nonreactive wetting. First, reactive wetting is significantly more sensitive to the addition of alloying elements [49]. In fact, it can be used to obtain very low contact angles using only 1 atomic percent of an alloying element. Nonreactive wetting, on the other hand, typically requires more than 10 atomic percent of an alloying element to see any improvement to wettability. In this case, the improvements are very limited compared to what can be achieved through reactive wetting. Another important difference is how interfacial reaction kinetics can affect the efficacy of reactive wetting. As mentioned before, nonreactive wetting reaches equilibrium at 10^{-3} seconds. Conversely, reactive wetting can take 100 seconds to stabilize for Cu-Ti/Al_2O_3 systems. [49] It will take over 20 minutes to reach equilibrium for an Al-Si alloy on the basal face of hexagonal SiC crystals. The rate is limited by dissociation of SiC and equilibrium will not be reached until the aluminum is saturated with carbon and silicon. Lastly, reactive wetting is also strongly affected by the temperature of the system. The temperature can change the interfacial reaction occurring in the system. Temperature also plays a critical role in the kinetics of interfacial reactions, which affects the rate the system reaches equilibrium.

Reactive systems are difficult to study because it combines the issues of time-dependent interfacial reactions and the kinetics of wetting. To describe wetting in a reactive system, one proposed description is:

$$\cos(\theta_{\min}) = \cos(\theta_o) - \frac{\Delta\sigma_r}{\sigma_{MV}} - \frac{\Delta G_r}{\sigma_{MV}}$$

Where θ_o = contact angle of the liquid on ceramic without any reaction

$\Delta\sigma_r$ = change in interfacial energies due to interfacial reaction

ΔG_r = change in free energy per unit area due to reaction of material adjacent to interface

In order for the above equation to apply for the system, the interaction must be limited to the triple line. Otherwise, the interfacial reactions do not drive wetting as described by the equation. Two common examples of reactions that are not characterized by the equation are phase transformations of the ceramic phase and when the triple line precedes the interfacial reaction. Unlike nonreactive systems, the kinetics of reactive systems is limited by diffusion in the solid, liquid, or through the reaction layer. The rate of the reaction is highest at the first moment of contact and eventually slows down as the interface becomes saturated with the product of the reaction. As a result, the contact angle will increase as the molten metal reaches equilibrium with the new interface.

Reactive wetting can lead to large, uncontrollable reactions between the matrix and the scaffold. To control this, a nonreactive metal can be alloyed with a small amount of a reactive solute. This technique is often used for brazing alloys for ceramics. It was also used to infiltrate aluminum oxide using nickel containing a reactive solute, titanium. With this technique, the reactive solute can form a continuous intermetallic or oxide layer. Ideally, the product would have high metallicity to allow for good wetting results. There are examples of perfect wetting as a result of the technique with a Cu-Ti/Al2O3 system. [49] The effectiveness of this technique is shown in the graph below. One important result is that partial wetting can occur with the addition of less than 10 atomic percentage of a particularly effective solute, such as titanium. In this case, the strong O-Ti interaction forms a titanium oxide layer that is semimetallic and very beneficial for wettability. The effectiveness of titanium is shown in Figure 18. [49]

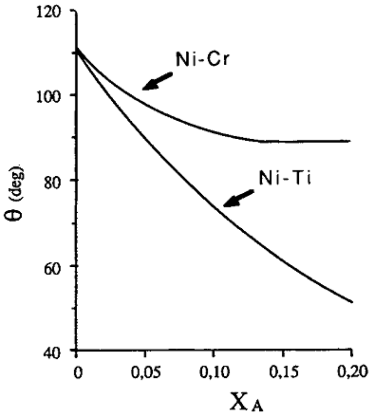

Figure 18: Variation in contact angle θ of Ni-based alloys on alumina with molar fraction X of Cr and Ti at 1773 K. The effect of Cr results from adsorption only, whereas the effect of Ti results from a combination of adsorption and the formation of a new phase at the interface. [48]

In conclusion, there are many parameters that control the wetting and infiltration behavior of ceramic/metal systems. This problem can scale from wetting and spreading kinetics of liquid metals, capillary forces, and interfacial interactions. To study the capillary forces in the pores as they are infiltrated by a molten metal, it is important to account for the unsaturated nature of most infiltration, the pressure applied to the system, and the various pore size of the ceramic scaffold using the Brooks–Corey correlation, rather than the slug-flow assumptions. Another very important processing parameter is the composition of the samples in the system. With additions of reactive metallic species or oxygen gas, a typically inert gas can have substantial increases in wettability. Otherwise, external pressures must be applied to aid infiltration and overcome capillary forces that typically prevent molten metals from infiltrating ceramics. There are many processing parameters that are critical for infiltrating a micron-scale ceramic pore with molten metals. Understanding of these capillary forces and interfacial reactions can lead to fabrication of new ceramic/metal composites with an ordered, brick-and-mortar microstructure such as nacre.

Chapter 3

Bioinspired "Nacre-Like" Alumina/Bulk-Metallic Glass Ceramics

We selected a Zr-based bulk-metallic glass (BMG) as the mortar phase as this alloy shows excellent wettability with alumina.[30,31] Zr-based BMGs have been shown to have high strength with some degree of toughness, which represent ideal properties as a compliant-phase (mortar) material. As a result, the combination of near-perfect wettability and mechanical properties of the BMG makes it an interesting candidate for infiltration into a brick-like ceramic scaffold. However, processing of BMGs can be difficult because they are prone to oxidation at elevated temperatures[32] and have a critical cooling rate required to solidify in the amorphous state; moreover, the final material must be used below the BMG's glass-transition temperature as these glasses can embrittle if they are allowed to crystallize.[33] While fibrous or particulate BMG matrix composites have been developed by melt infiltration,[34,35] this study relates their infiltration behavior to the thermo-physical properties and wettability of the BMG. This can be used to tailor the properties of the ceramic/metal interfaces while maintaining the BMG in the fully amorphous state as a metallic mortar in nacre-like material.

In this study, we demonstrate the synthesis of alumina-glass ceramics with nacre-like (high volume fraction) alumina scaffolds using pressureless infiltration. Infiltration behavior studied using contact-angle measurement and electrostatic levitation indicates that the length-scale of the scaffolds and the excellent wettability of a ceramic with a liquid alloy are crucial factors to warrant the successful synthesis of these materials. Near-perfect wetting within seconds for the Zr-based BMG on alumina was achieved, indicating that a conformal bond can be attained at the interface of the two materials, which in turn implies high strength may be realized in an Al_2O_3/BMG hybrid material.[36,37] However, depending upon the infiltration temperature, after solidification of the metallic phase, the interfacial strength can markedly change due to the formation of brittle interfaces, which can potentially compromise strength and toughness of the processed material. Accordingly, in addition to describing the processing of brick-and-mortar, high volume fraction (~80 vol.%) alumina containing a metallic compliant phase, we examine how processing conditions can affect the ceramic-metal interfaces in order to discern the fundamental mechanisms underlying the flexural strength and fracture toughness of these bioinspired nacre-like ceramics.

SECTION 3.1. METHODS

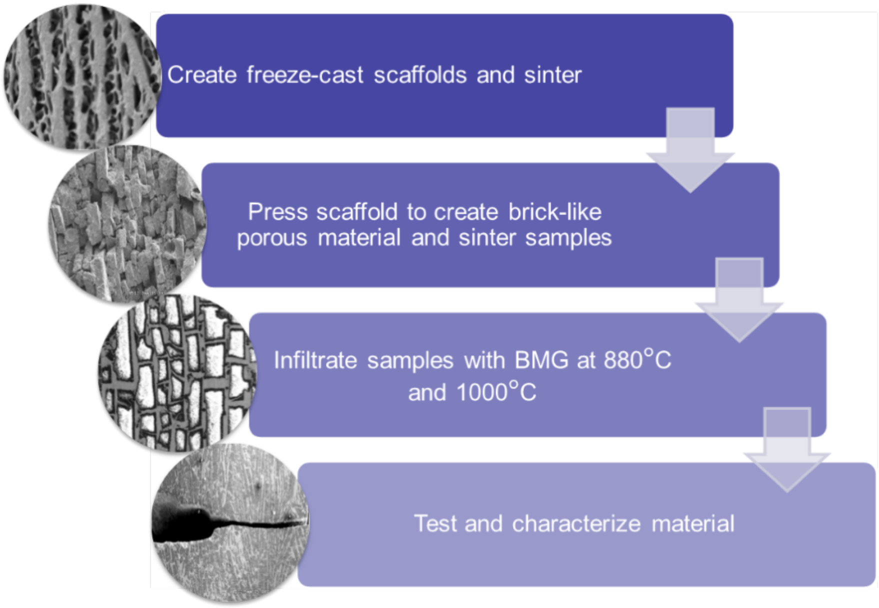

Figure 1: Overview of methods to create the bioinspired materials using a top-down reactive melt infiltration approach

SECTION 3.1.1. Materials processing

To examine the conditions for metal infiltration into the freeze-cast alumina scaffolds, both lamellar and the final brick-and-mortar structures were processed, as summarized in Figure 1. These ceramic scaffolds were first fabricated by freeze-casting a water-based suspension consisting of 37 vol.% alumina powder (Nanocrystalline, sub-micrometer α-Al_2O_3 powder, Inframat Advanced Materials, Manchester, CT). The suspensions were formulated with 2.5 powder wt.% of polyacrylic acid (PAA) (98-99% hydrolyzed, high molecular weight, Alfa Aesar, Tewksbury, MA) which was added as a dispersant. Hydrochloric acid (25% (v/v) Aqueous Solution, Ricca Chemical Company, Arlington, TX) was also used to maintain a pH at about 2 to prevent agglomeration. The samples were milled to mix and homogenize for a minimum of 12 hr.

The samples were placed in a cylindrical Teflon mold with a copper cold finger at the bottom. The suspension in the mold was subjected to controlled directional freezing, which allows lamellar scaffolds to form. The cold finger was cooled to 113 K at a rate of -5 K/min, with its temperature controlled with a liquid nitrogen cold bath and ring heater. To prepare samples with a lamellar structure aligned over several centimeters, the materials were first cast using a polydimethylsiloxane (PDMS), 20° angle, wedge to induce bidirectional freezing, as discussed elsewhere.[45] After complete freezing, the samples were removed from the mold and placed in the freeze drier (Freeze Dryer 8, Labconco, Kansas City, MI). By holding the samples for three days in a low pressure (0.06 mbar), ambient temperature environment, the ice was sublimated to form green ceramic lamellar scaffolds, which were subsequently fired for 2 hr in air at 873 K to eliminate the organic additives before being sintered at 1823 K for 3 hr (Air furnace: 1216BL, CM Furnaces Inc., Bloomfield, NJ) to densify the ceramic lamellae. To convert these lamellar structures into a brick-and-mortar form, they were infiltrated with paraffin wax and then compacted in a hydraulic press at a pressure of 1200-1400 MPa to ensure a high ceramic content, with plates heated at 353

K to allow the wax to flow. After pressing, the samples were fired and sintered using the same procedure described above and subsequently cut into 2.5 x 2.5 x 12-15 mm pieces before infiltration with the BMG.

The $Zr_{46}Cu_{30.14}Ag_{8.36}Al_{8}Be_{7.5}$ (at.%) BMG ingots, which have a high glass forming ability that can be cast up to a critical diameter of 73 mm,[46] were fabricated by arc melting a mixture of their constituent elements (Ag, Al, Cu, and Zr with a purity of above 99.9%) and a commercial Cu-Be alloy ($Cu_{77.3}Be_{22.7}$) under a Ti-gettered Ar atmosphere. The ingots were re-melted three times to ensure compositional homogeneity before the alloys were cast into a copper mold (4 mm in diameter, 50 mm in length).

The alumina/BMG compliant-phase ceramic was prepared by pressureless melt infiltration into the alumina scaffold. Specifically, the scaffold was placed in a quartz tube with inner diameter of 5 mm, and then the tube was necked 3 mm above the scaffold to prevent floatation during the infiltration. The as-cast BMG rod was placed on the neck, and then the tube was sealed *in vacuo* using a rotary pump to prevent the oxidation of the as-cast rod during the processing. The sealed tube was placed in an electric resistance furnace heated to 1153 K or 1273 K, *i.e.,* above the melting temperature of the BMG (1103 K). After holding for 3 min, the tube, where the molten BMG was trapped on the neck due to its high viscosity and surface oxide layer, was tapped on the bottom of the furnace to dispense fresh BMG melt under the neck. The scaffold immersed in the BMG melt was held for 10 min during which the scaffold was infiltrated without external pressure. The tube after infiltration was removed from the furnace and quenched in ice water.

SECTION 3.1.1. Measurement of thermophysical and wetting properties.

Thermophysical properties of the BMG were determined by an electrostatic levitation method (ESL) in Japan Aerospace Exploration Agency (JAXA). Ball-shaped samples of ~2 mm in diameter were prepared by arc melting pieces of the as-cast BMG rods. The spherical samples were levitated in a high-vacuum environment (~ 10^{-5} Pa) using electrostatic forces. Samples were heated and melted by CO_2 lasers, and the temperature was measured using pyrometers at 120 Hz acquisition rate. Surface tension and viscosity of the $Zr_{46}Cu_{30.14}Ag_{8.36}Al_{8}Be_{7.5}$ alloy were determined using the oscillation-drop method, as described elsewhere.[47]

Contact angles of the BMG on the polycrystalline alumina substrate were measured in a vacuum of ~10^{-4} Pa by the sessile-drop method, utilizing a stainless steel vacuum chamber equipped with a drop dispenser and a tube furnace.[48] About 100 mg of the BMG sample was prepared by arc melting pieces of the as-cast BMG rods. The alumina substrates were prepared by polishing with diamond pastes to give an average surface roughness below 100 nm. The substrate was positioned ~5 mm below the BMG sample in the dispenser which was then heated with a tube-shaped Mo resistance wire furnace. The BMG melt was pushed through a 1 mm diameter hole by increasing the argon pressure and then dropped on the substrate. The experiment was observed through a hole in the furnace, and images of the droplet were recorded at a speed of 10 frames per second by using a high-speed digital camera.

Phase constitution was confirmed by x-ray diffraction (XRD; New D8 Advance, Bruker Corporation, Karlsruhe, Germany) using monochromatic Cu Kα radiation operated at 40 kV and 40 mA. Thermal analysis of the alumina/BMG ceramic was conducted by differential scanning calorimetry (DSC, DSC 8500, Perkin Elmer, Waltham, USA) using a constant heating rate of 40

K/min. The microstructures of the Al_2O_3/BMG ceramic were analyzed using scanning electron microscopy (SEM; SU70, Hitachi Corp., Tokyo, Japan) equipped with energy-dispersive x-ray spectroscopy.

SECTION 3.1.2. Materials preparation and micro-scale interface characterization.

After casting, the samples were cut and polished for mechanical testing and characterization. Both ends of the ingot were machined off using a water-cooled low-speed circular saw to reveal the cross-sectional region of the material, which was then ground into rectangular beams (2.3-2.5 mm wide, 2.3-2.5 mm thick, 12-15 mm in length) using SiC papers with grits ranging from 60-1200, with a final polish with a 1 μm diamond suspension.

To determine the interface fracture strength between the ceramic bricks and the BMG mortar, samples from both infiltration temperatures were tested using notched micro-cantilever beams that were focused ion-beam (FIB, LEO 1540 XB, Carl Zeiss AG, Oberkochen, Germany) milled at 30 kV acceleration voltage with ion currents subsequently decreasing from 10 nA to 500 pA. The initial notch with a radius of ~20 nm was placed possibly close to the interface by utilizing a current of 100 pA. All micro-cantilever fracture experiments were subsequently conducted *in situ* in an SEM (DSM 982, Carl Zeiss AG, Oberkochen Germany) using a Hysitron picoindenter PI-85 (Bruker Corporation, Billerica, USA) equipped with a wedge-shaped conductive diamond tip (Synton-MDP AG, Nidau, Switzerland), operated in open-loop mode with a loading rate of 10 μN/s. To compare the interface fracture characteristics, the conditional stress intensity *vs.* displacement was calculated from the load-displacement data as outlined by Wurster *et al.*[49]

SECTION 3.1.3. Macroscale strength and toughness measurements.

The macroscopic flexural strength of the samples was measured using three-point bend testing on unnotched specimens, with a loading support span of 10 mm, at a displacement rate of 1 mm/sec, in general accordance with the ASTM Standard D790.[50] These tests were performed on an Instron 5944 electro-mechanical testing system (Instron Corporation, Norwood, MA, USA).

Fracture toughness measurements were conducted on single edged-notched bend (SE(B)) samples, which were notched using a low-speed diamond saw. The notch root was then sharpened using a micro-notching technique which involves polishing the end of the notch with a razor blade under load, immersed in a 6-μm diamond slurry; resulting notch root radii were typically on the order of 10 μm. These samples were loaded at a displacement rate of 0.55 μm/sec in three-point bending, with a loading span of 10 mm, in general accordance with ASTM Standard E1820.[40] Tests were performed using a Deben MicroTest 2kN (Deben, UK) bending stage embedded in a Hitachi S-4300SE/N (Hitachi America, Pleasanton, CA, USA) SEM to permit real-time observations of the crack path and its interaction with the prevailing microstructure during the measurement of the fracture toughness and crack-resistance curves.

Due to the relatively small size of the fracture toughness samples and the fact that these compliant-phase ceramic materials display some degree of inelasticity, nonlinear-elastic fracture mechanics measurements were made to determine J-based crack-resistance curves (J-R curves), where J is the J-integral, *i.e.*, the field parameter that characterizes the local nonlinear-elastic (Hutchinson-Rice-Rosengren, HRR) stress and displacements fields in the immediate vicinity of a crack tip in a nonlinear-elastic solid. The R-curve assesses the value of J required to sustain stable crack extension. In the current tests, such crack extension was measured using the elastic unloading compliance of the specimen, whereas corresponding J values were computed in terms of their elastic and plastic components ($J = J_{el} + J_{pl}$). The elastic component of J was calculated from the linear-elastic stress intensity value, K, i.e., $J_{el} = K^2/E'$, where $E' = E$ (Young's modulus) in plane stress and $E/(1 - \nu)^2$ in plane strain (ν is Poisson's ratio); the plastic component was determined in terms of the plastic portion of the area under the load-displacement curve, A_{pl}, using the expression $J_{pl} = 1.9A_{pl}/Bb$, where b is the uncracked ligament size and B is the sample thickness.[55] Equivalent stress-intensity values were then back-calculated from these measured J values using the standard mode I J-K equivalence, *i.e.*, $K_J = (J E')^{½}$.

SECTION 3.2. RESULTS

SECTION 3.2.1. Surface tension, viscosity, and contact angle.

Surface tension (γ) and viscosity (η) of the $Zr_{46}Cu_{30.14}Ag_{8.36}Al_8Be_{7.5}$ BMG-forming alloy were evaluated by electrostatic levitation (ESL) over the temperature range from 1180 K to 1310 K. The surface tension γ of the melt showed a negative temperature dependence (Fig. 2a) that can be described, in terms of the absolute temperature T (in Kelvin), as:

$$\gamma = 1.69 - 4.07\times10^{-4}\,T\,, \qquad (1)$$

and a negative temperature dependence of the viscosity η (Fig. 2b), which can be described by the Vogel-Fulcher-Tammann relationship[56] as:

$$\eta = \eta_0 \exp\left(\frac{D^* T_0}{T - T_0}\right), \qquad (2)$$

where η_0 is the viscosity in the infinite temperature limit (2.03×10^{-4} Pa·s), D^* is the fragility parameter (5.87) and T_0 is the absolute temperature (598 K) where the viscosity becomes infinite.[56]

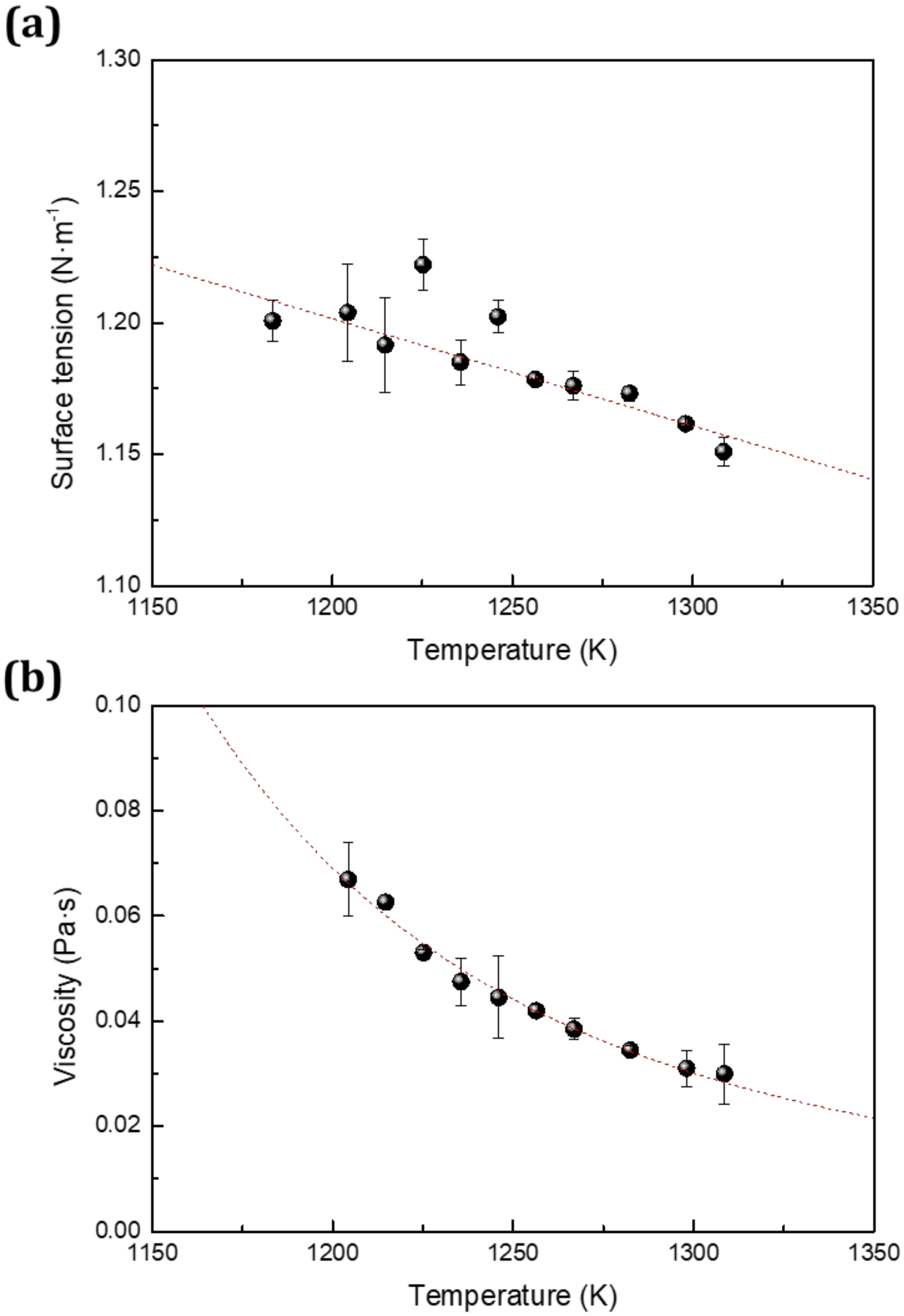

Figure 2. **Thermophysical properties of the bulk-metallic glass.** (a) Surface tension (γ) and (b) viscosity (η) of the $Zr_{46}Cu_{30.14}Ag_{8.36}Al_8Be_{7.5}$ BMG-forming alloy melt measured by electrostatic levitation (ESL) over the temperature range from 1180 K to 1310 K. The surface tension decreases by a mere 5% over the temperature range, while the viscosity for the melt decreases by ~50% with increasing temperature.

The wettability of alumina by the BMG was evaluated by the sessile-drop method at 1153 K and 1273 K (Fig. 3). As shown in the inset of Figure 3, the alloy melt that was dropped on the alumina substrate exhibited initial contact angles of ~14°, and decreased continuously within several tens of seconds. The final contact angles were 8° at 1153 K and 6° at 1273 K, showing the excellent wetting behavior of alumina by the BMG alloy melt.

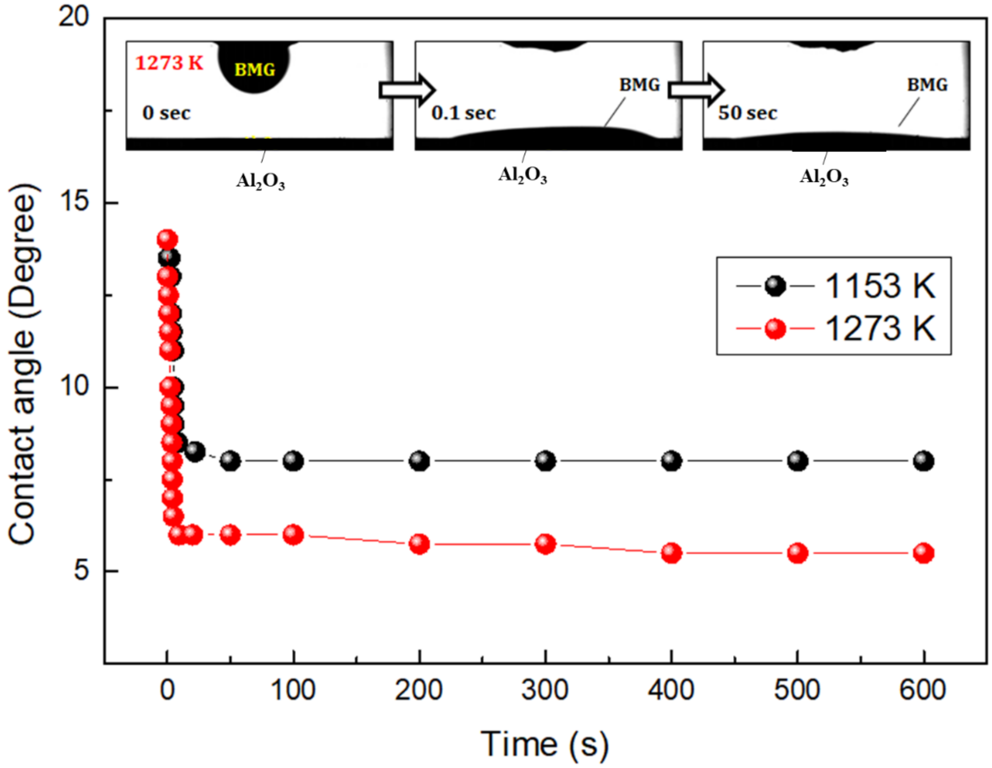

Figure 3. Rate and extent of wetting of bulk-metallic glass on alumina. Wetting angles, measured using a sessile-drop experiment, at temperatures of 1153 K and 1273 K. The wetting angles, when plotted with respect to time, show that the contact angle converges on 8° at 1153 K and 6° at 1273 K within 10 sec. This is a strong indication that the wetting kinetics are independent of any potential reaction occurring at the interface between the metal melt and the ceramic solid.

SECTION 3.2.2. Microstructure.

Figure 4a shows the phase constitution of the compliant-phase alumina/BMG materials with a lamellar structure infiltrated at 1153 K and 1273 K. In both curves, the peaks of crystalline phases were superimposed on the broad diffuse scattering, indicating the presence of large fractions of amorphous phase in the metallic mortar after the melt infiltration followed by water quenching. Both materials had dominant peaks of alumina and Zr_2Cu, which is one of the intermetallic compounds appearing in the $Zr_{46}Cu_{30.14}Ag_{8.36}Al_8Be_{7.5}$ BMG-forming alloy as heterogeneous nucleation occurs during solidification.[57,58] The peak intensity of Zr_2Cu phase increased as the infiltration temperature increased. Peaks of ZrO_2, which is one of the reaction products between alumina and the BMG-forming alloy melt,[31] were observed in the sample infiltrated at 1273 K.

The corresponding alumina/BMG materials with brick-and-mortar structure (Fig. 4b) had similar phase constitution as the lamellar samples but showed reduced peak intensity of metallic phases due to the decreased volume fraction of the metallic mortar. These results suggest that the phase constitution of these alumina/glass ceramics is independent of the alumina volume fraction, but dependent on the infiltration temperature.

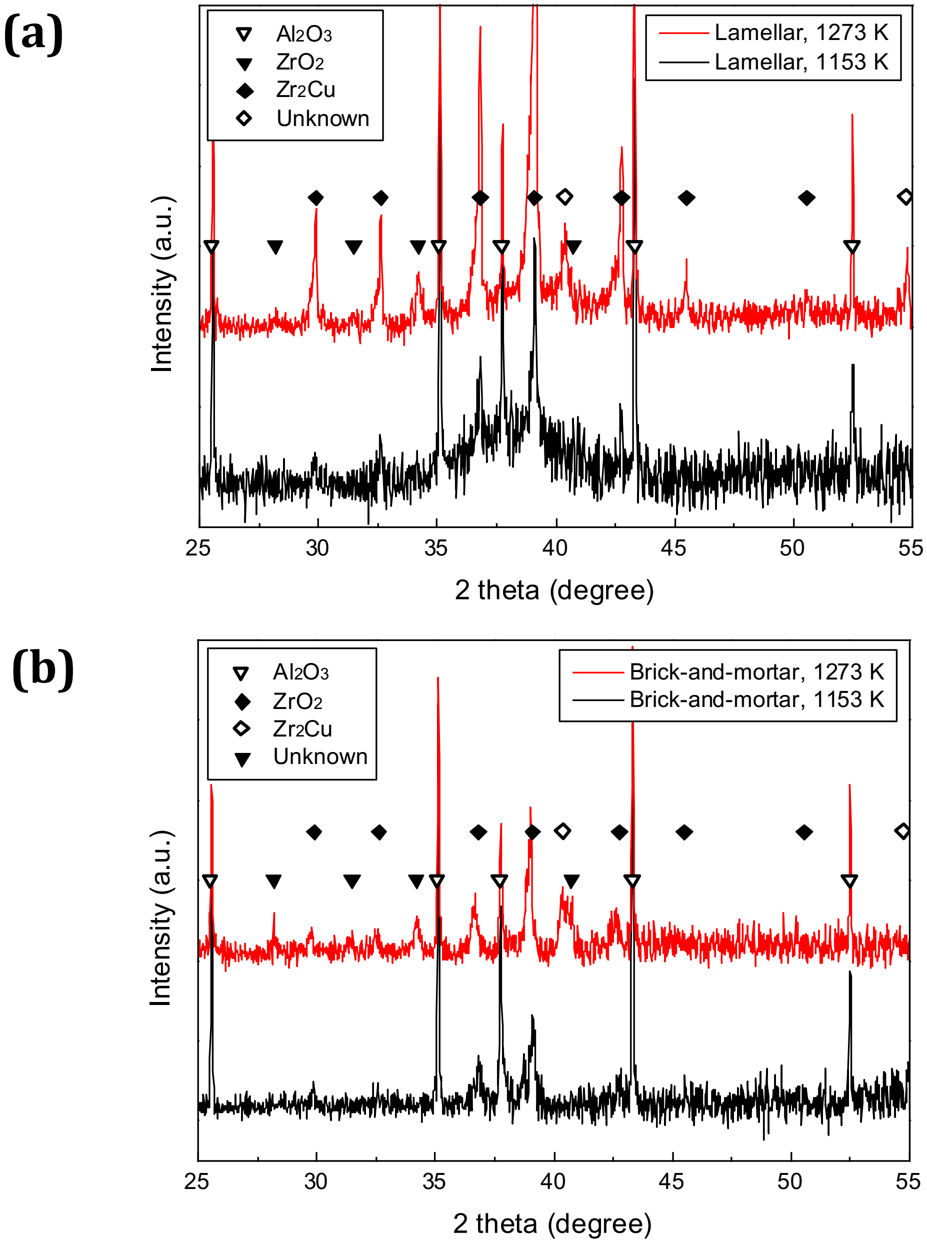

Figure 4. X-ray diffraction (XRD) of compliant-phase ceramics. XRD patterns of the alumina/BMG compliant-phase ceramics, with (a) lamellar structure and (b) brick-and-mortar structure, infiltrated at 1153 K and 1273 K. In both curves, the dominant peaks of alumina and Zr_2Cu were superimposed on the broad diffuse scattering, indicating the presence of an amorphous phase in the metallic mortar after the melt infiltration followed by water quenching. The results indicate that the phase constitution of the alumina/glass ceramics is dependent on the infiltration temperature, but independent of the alumina volume fraction.

Figures 5a and 5c show the microstructure of the alumina/glass ceramics with lamellar structure. A lamellae thickness of 7.7 ± 4.1 µm, metal thickness of 13.3 ± 4.7 µm, and alumina content of 37 vol.% were measured using image analysis. Figures 5b and 5d show the corresponding microstructure of the alumina/glass ceramics with brick-and-mortar structures, formed after spressing the alumina with paraffin wax and subsequently infiltrating with the $Zr_{46}Cu_{30.14}Ag_{8.36}Al_8Be_{7.5}$ BMG as the compliant (mortar) phase. The structure exhibits a brick thickness of 22.6 ± 11.2 µm, a metallic mortar thickness of 4.4 ± 3.4 µm, and an alumina content of 80 vol.%. All the materials prepared by pressureless infiltration display a well-formed lamellar and brick-and-mortar microstructure, apparently with complete infiltration, without pores, of the metallic mortar at both infiltration temperatures. Akin to natural nacre, both the lamellar and brick-and-mortar microstructures display pre-existing bridges that act as local connections between the alumina lamellae or between the bricks. The BMG-ceramic interfaces in the materials infiltrated at 1153 K and 1273 K are imaged in Figures 5e-5h. The materials infiltrated at 1153 K (Figs. 5e and 5g) show sharp interfaces between the alumina (black) and amorphous phase (gray), whereas the materials infiltrated at 1273 K (Figs. 5f and 5h) display evidence of erosion of the alumina surface with voids at the interface. The material with lamellar structure infiltrated at 1273 K (Fig. 5f) contains a faceted crystalline phase (dark gray) grown from the interface into the amorphous phase. This crystalline phase was identified as the intermetallic compound Zr_2Cu by EDS analysis, as shown in the XRD analysis in Figure 4. The material with brick-and-mortar structure infiltrated at 1273 K showed an irregular grain morphology in the metallic mortar, indicating the formation of multi-phase microstructure with Zr_2Cu and unknown phases, as shown in the XRD analysis. These results imply that the interfacial structure of our alumina/glass ceramics significantly changes as the infiltration temperature increases.

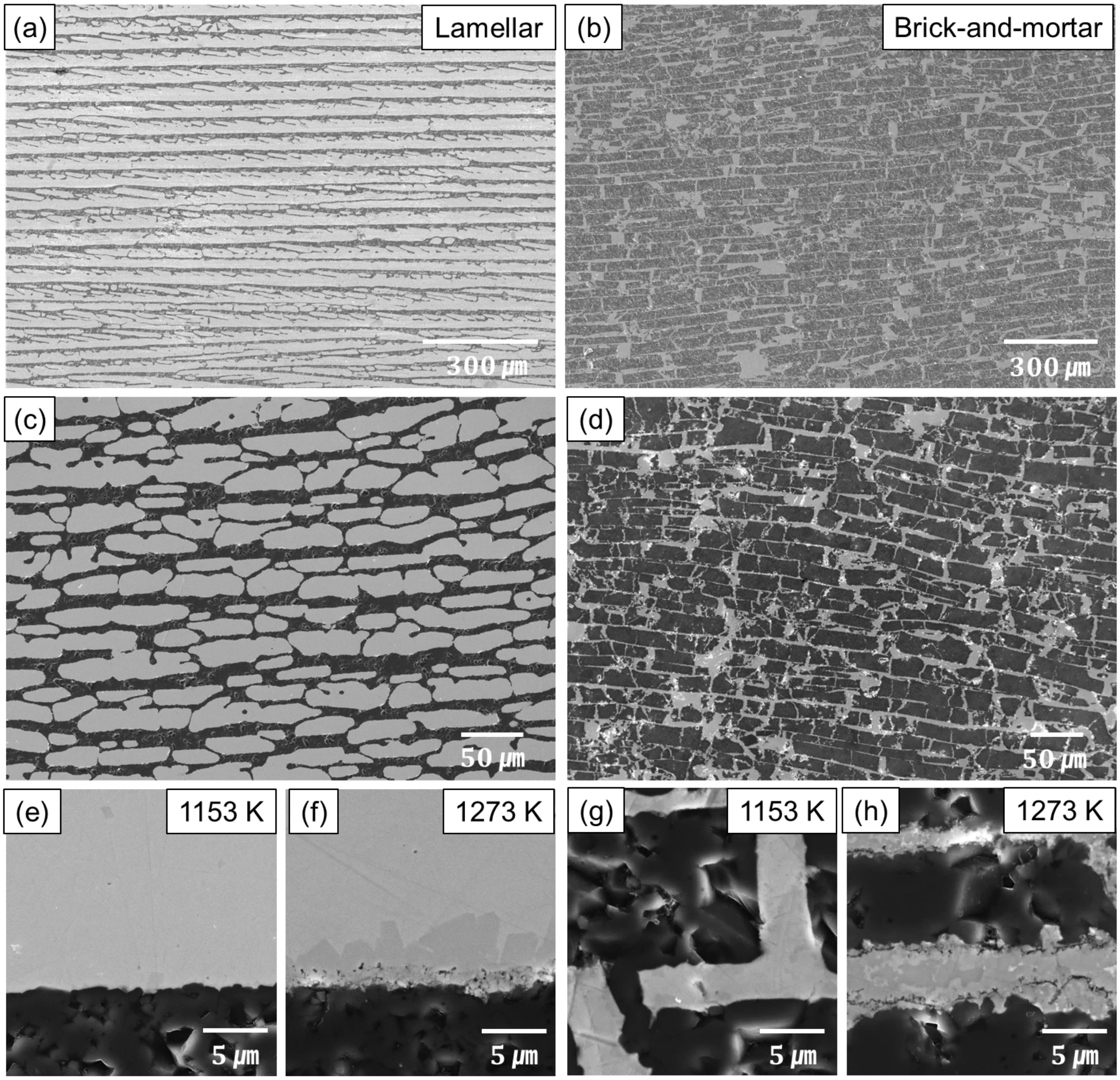

Figure 5. **SEM micrographs of the alumina/glass materials with (a,c) lamellar and (b,d) brick-and-mortar structures.** The metal-ceramic interfaces in these ceramics infiltrated at 1153 K and 1273 K are shown in (e,f) for lamellar structure and (g,h) for brick-and-mortar structures, respectively. The materials infiltrated at 1153 K (e,g) show a sharp interface between the alumina (black) and amorphous phase (gray), but the materials infiltrated at 1273 K (f,h) show erosion of the alumina surface and voids at the interface.

Differential scanning calorimetry (DSC) traces of the alumina/glass ceramics with different structures and infiltration temperatures are given in Figure 6. All materials showed a decrease in the crystallization onset temperature (T_x) compared to the monolithic BMG. The reduced thermal stability of the amorphous phase is attributed to the presence of the BMG-ceramic and BMG-intermetallic compound interfaces that act as heterogeneous nucleation sites during heating.[57] All the materials exhibited a similar glass transition temperature T_g of 705 K and crystallization onset temperature $T_{x.\mathrm{Hybrid}}$ of 790 K, indicating that the composition of the amorphous phase in the metallic mortar is very similar to that in the alumina/glass (hybrid) materials. The heats of crystallization were measured as 74.4 J·g^{-1} and 41.5 J·g^{-1} for lamellar structure, and 52.5 J·g^{-1} and 2.2 J·g^{-1} for brick-and-mortar structure infiltrated at 1153 K and 1273K, respectively; all being lower than in monolithic BMG. The results indicate that the volume fraction of amorphous phase present in the metallic mortar is lower while that of the crystalline phase increases with increasing infiltration temperature.

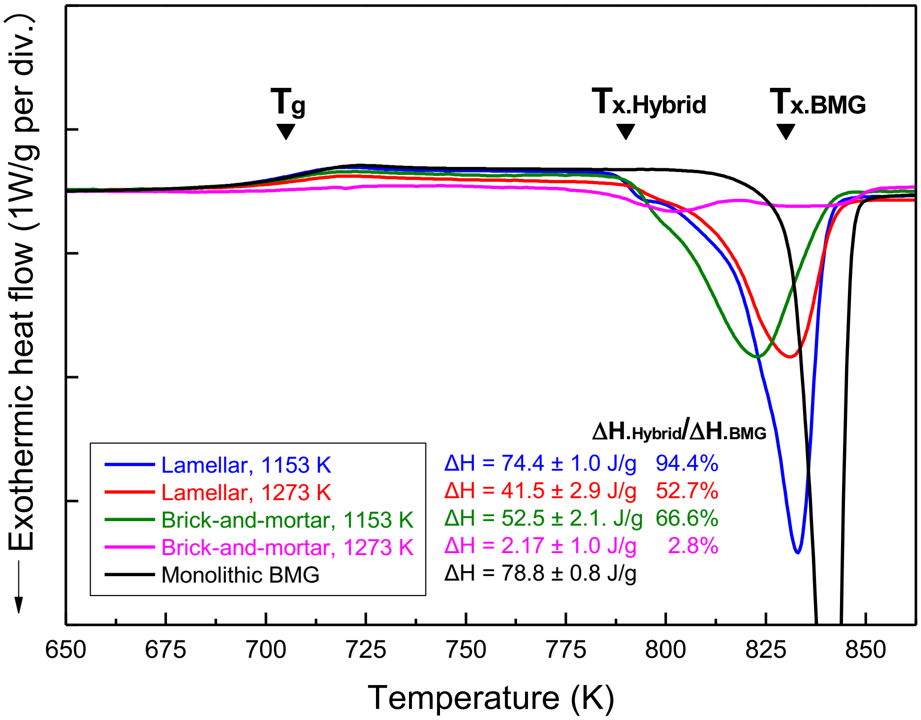

Figure 6. Differential scanning calorimetry results for the compliant-phase ceramics. DSC traces for the alumina/glass ceramics with lamellar and brick-and-mortar structures infiltrated at 1153 K and 1273 K. T_g is the glass transition temperature, T_x is the onset temperature of crystallization, and ΔH is the heat of crystallization. The amorphous fraction in the metallic phase is determined by comparing the change of enthalpy during this crystallization event in the infiltrated ceramic-glass samples to the change of enthalpy for the monolithic BMG.

SECTION 3.2.3. Mechanical Properties.

The flexural strength of the alumina/glass ceramics was found to be markedly affected by the infiltration temperature used to produce the material. Lamellar samples infiltrated at 1153 K had a flexural strength of ~797±60 MPa, whereas those infiltrated at 1273 K displayed a dramatically lower value of ~225±11 MPa. The brick-and-mortar specimens had a flexural strength of

~366±168 MPa when infiltrated at 1153 K and again showed a much lower strength, of ~88±28 MPa, when infiltrated at 1273 K. For both brick-and-mortar and lamellar structures, infiltrating at higher temperature resulted in an approximate four-fold decrease in strength, compared to those infiltrated at 1153 K (Fig. 7a). The strength was also affected by the ceramic content of the materials; alumina has a flexural strength of ~330 MPa, compared to the BMG at 1700 MPa. Accordingly, the strength of the brick-and-mortar samples, with their far higher volume fraction of ceramic, was significantly lower than that of the lamellar samples.

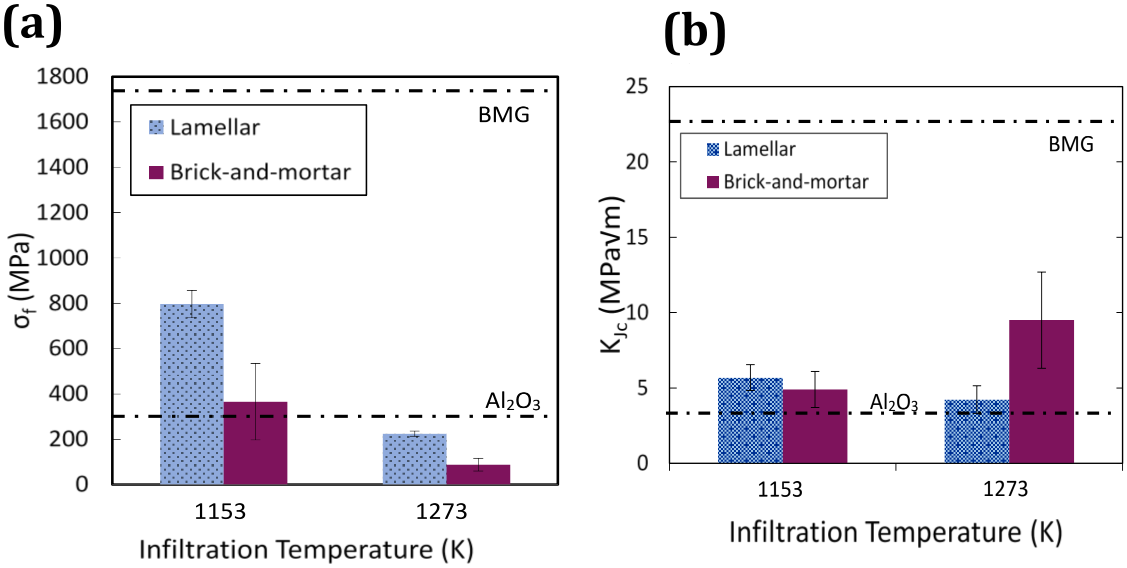

Figure 7. Flexural strength (a) and fracture toughness (b) results for compliant-phase ceramics. Influence of infiltration temperature on the flexural strength, σ_f, of the lamellar and brick-and-mortar samples. The strength of the samples can reach as high as 800 MPa for lamellar samples and 400 MPa for brick-and-mortar samples. While the flexural strength is dwarfed by its BMG constituent, its strength is significantly higher than in pure alumina, the main component of the brick-and-mortar materials. This flexural strength decreases by 75% when infiltrated at higher temperatures and relates to matrix crystallinity and interfacial strength between the ceramic and metallic phases. Effects of infiltration temperature on the fracture toughness of lamellar and brick-and-mortar samples are measured using single-edge notched three-point bend tests. The fracture toughness values of the materials are higher than for monolithic alumina, the main component of the brick-and-mortar materials. The significant impact of sample morphology is seen by the fact that the lamellar samples show very little changes in fracture toughness when infiltrated at different temperatures. However, the brick-and-mortar samples show a large increase in fracture toughness from about 5 MPa·m$^{1/2}$ to 8 MPa·m$^{1/2}$ (with the R-curve rising as high as 14 MPa·m$^{1/2}$), when infiltrated at higher temperatures.

Conversely, there was little change in the fracture toughness of the lamellar samples infiltrated at 1153 K and at 1273 K, which were measured to be 5.7±0.9 MPa·m$^{1/2}$ and 4.2±0.9 MPa·m$^{1/2}$, respectively (Fig. 7b); indeed, they are comparable when considering their standard deviations. However, the brick-and-mortar samples show very different properties. Brick-and-mortar samples infiltrated at 1153 K failed catastrophically with a fracture toughness of ~5 MPa·m$^{1/2}$ with no stable crack growth. In contrast, those infiltrated at 1273 K displayed a stable crack growth with crack extensions of almost 1 mm along the interface between the ceramic and metallic phases. As a result, the fracture toughness of these brick-and-mortar materials displayed markedly rising R-curve behavior (Fig. 8), with the toughness increasing from the intersect of the blunting line of roughly 5 MPa·m^{½} to 8 MPa·m^{½} after ~200 μm of stable crack growth and ultimately reaching as high as 14 MPa·m^{½} (although, as Figure 8 indicates, the higher toughness number is not strictly valid in terms of ASTM Standard E1820[40]). SEM micrographs in Figures 9b and 9d reveal that both lamellar and brick-and-mortar samples infiltrated at 1273 K failed with multiple crack-path deviations off the plane of maximum tensile stress caused by crack deflections along the ceramic/metal interfaces; this creates a rough fracture surface with significant evidence of pull-out of the ceramic bricks, and consequently higher toughness. In contrast, all samples infiltrated at 1153 K in Figures 9a and 9c failed catastrophically directly at the onset of crack initiation.

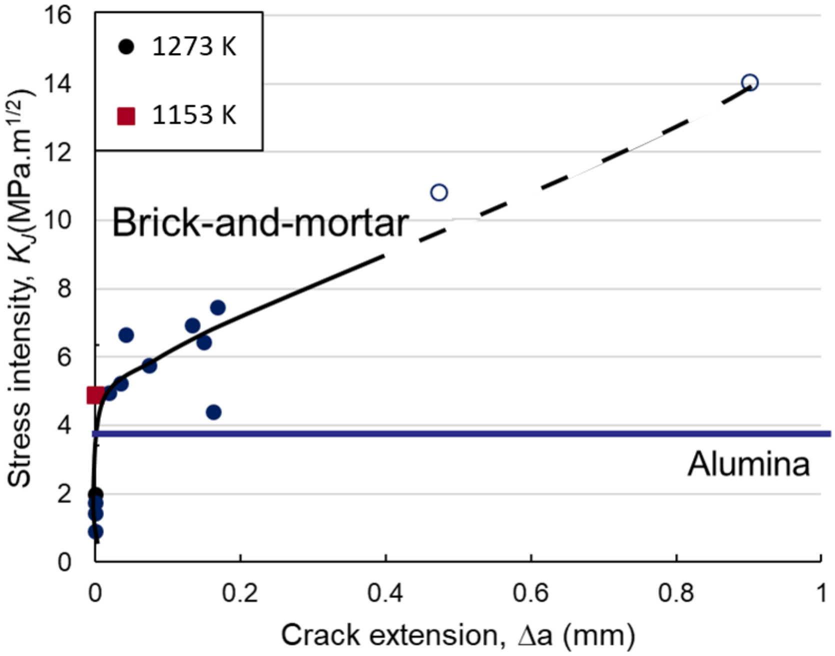

Figure 8. Crack-resistance curves (R-curves) for brick-and-mortar alumina/BMG ceramics infiltrated at 1273K. The onset of crack initiation and immediate catastrophic fracture of samples infiltrated at 1153 K is included for reference. Comparison of the fracture toughness between the ceramics infiltrated at the two infiltration temperatures indicates how an appropriately created brick-and-mortar microstructure can serve to stabilize the slow growth of incipient cracks, manifested in the form of a rising R-curve, rather than leading to unstable catastrophic fracture at the onset of crack initiation. (The open circles refer to data points that are not strictly valid according to ASTM Standard E1820, as they exceed the maximum crack extension capacity for the test specimens that were used.)

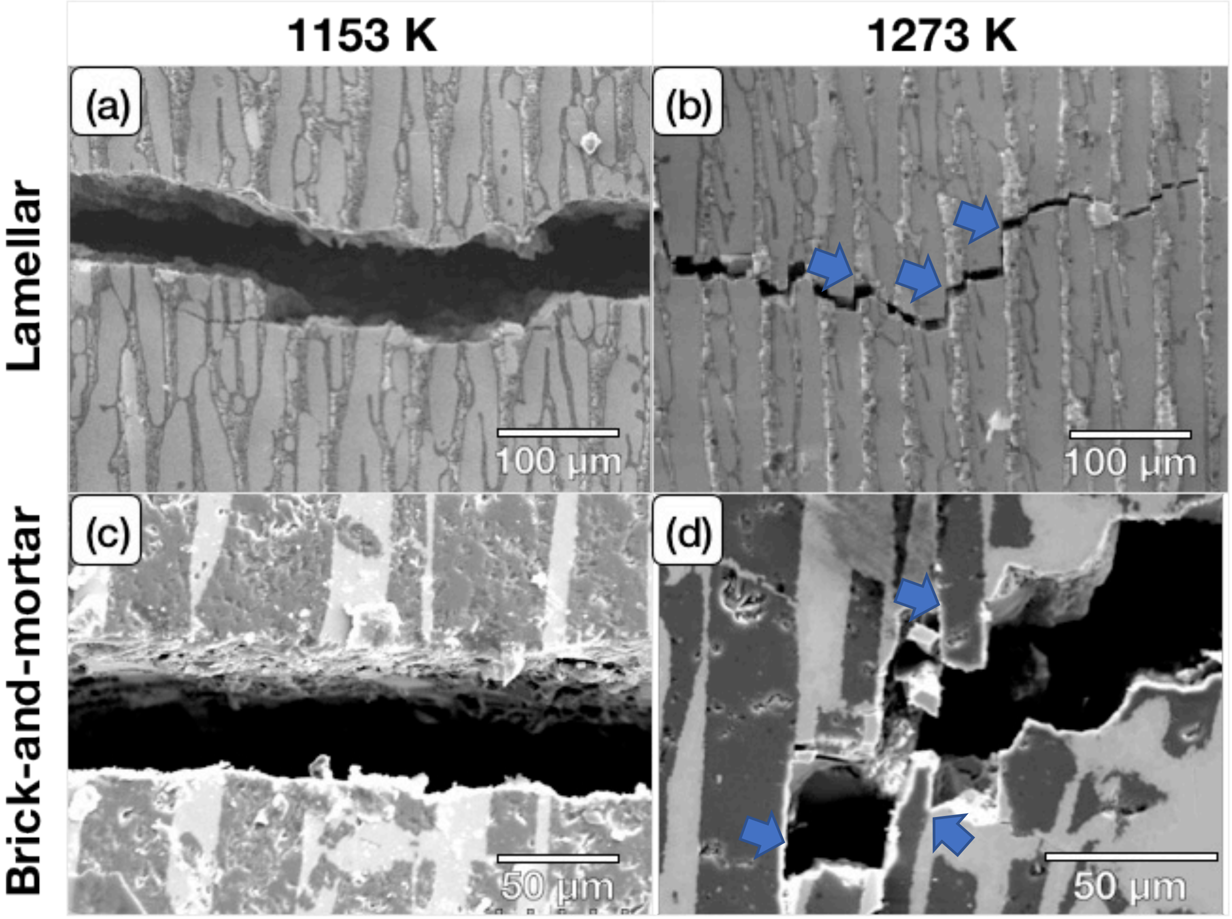

Figure 9. SEM micrographs of crack patterns of the infiltrated alumina/BMG compliant-phase ceramic samples. Lamellar (a,b) and brick-and-mortar (c,d) samples infiltrated at 1153 K (880°C) show little to no crack deflection behavior, in contrast to the corresponding samples infiltrated at 1273 K (1000°C) which exhibit crack deflection due to crack propagation along the interface of the ceramic and metallic components, which in turn leads to ceramic brick pull-out and hence extrinsic toughening from crack bridging. The arrows highlight where the cracks propagated along the interface of the ceramic and metallic phases. This behavior is critical for stable crack-growth behavior and increases the crack-growth fracture toughness in the brick-and-mortar samples primarily due to crack bridging; however, superior damage-tolerance would be generated if the inter-ceramic brick displacements occurred within the metallic mortar, rather than involving ceramic/metal interface failure.

To address the individual interfaces in more detail, micro-cantilever experiments, as depicted in Figure 10a, were conducted on lamellar as well as brick and mortar samples of both infiltration temperatures. Notably, whereas the hierarchical structure exhibited no influence on the local interfacial fracture behavior, the change in infiltration temperature resulted in a major discrepancy. Figure 10b shows the conditional stress intensity-displacement data for 1153 K and 1273 K specimens. Due to the non-linear elastic behavior and the fact that the 1153 K sample did not break at the interface, these values are to be taken predominantly as a means of comparison between each other. Nevertheless, the lower stress intensity at failure of the 1273 K specimen goes hand in hand with the fact that the adhesion between the Al_2O_3 matrix and the BMG-mortar was rather weak. The interface fracture surfaces (Figs. 10e and 10f) show high fractions of asperities and individual particles not connected to the BMG-mortar. Conversely, the 1153 K specimen did not break at the interface but the crack extended through the weaker BMG in a stable manner, leaving behind a large plastically deformed zone, as depicted in Figures 10c and 10d.

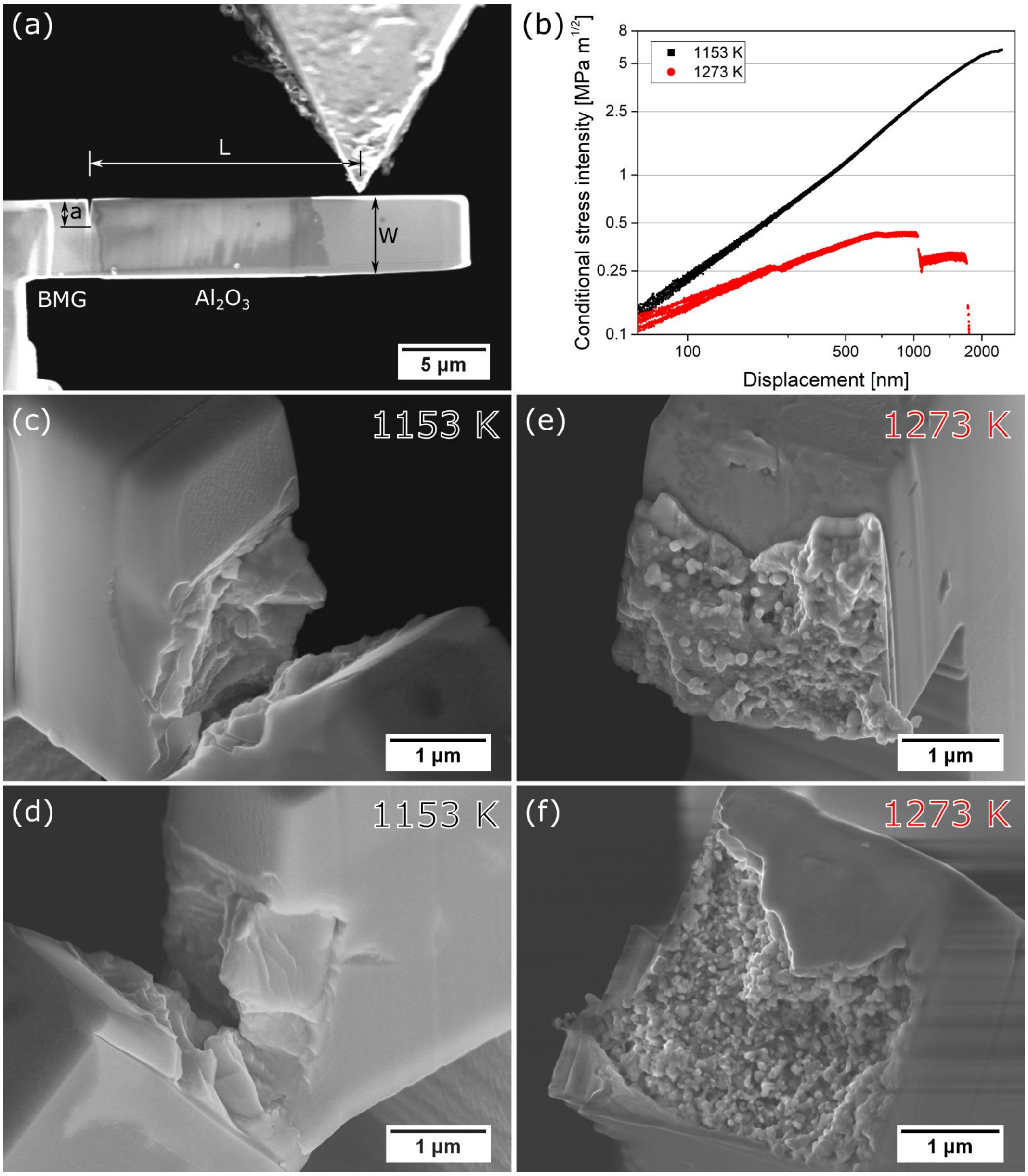

Figure 10. SEM micrographs and results of micro-cantilever tests. (a) Representative micro-cantilever specimen for interface toughness measurement. (b) Conditional stress intensity–displacement curves for 1153 K (black) and 1273 K (red) infiltrated specimens, respectively, on log-log scale. SEM micrographs of the fracture surfaces of the same (c, d) 1153 K and (e, f) 1273 K infiltrated specimens, showing a clear distinction between interfacial fracture (e, f) and fracture through the BMG phase (c, d).

SECTION 3.3. DISCUSSION

In this work, we have created a freeze-cast alumina ceramic with a bioinspired, nacre-like, brick-and-mortar structure with a Zr-based BMG as the infiltrated compliant-phase mortar. Our motivation is that nacre-like alumina infiltrated with a polymer compliant phase has been shown to have exceptional toughness,[11] and theoretical modeling has predicted that the mechanical properties may be even better with a metallic mortar.[13] To overcome the issues associated with infiltrating a metal into a ceramic scaffold, we have employed the concept of reactive wetting by utilizing a Zr-based BMG as the infiltrating phase. We discuss below the features of our processing procedures to create these materials, our associated attempts at "tailoring" the ceramic/metal interfaces, and finally how these factors can result in enhanced damage-tolerant properties in nacre-like structural ceramics.

SECTION 3.3.1. Infiltration Behavior

The excellent wettability allowed spontaneous infiltration of the nacre-like alumina scaffolds at very rapid rates (10 min hold time) without the need for applied pressure. This was possible due to the high bonding strength between the alumina and the BMG melt, which can be up to an order of magnitude higher than non-reactive metal/alumina couples. This was measured using the work of adhesion, which was calculated from surface tension and final contact angles, as shown in section 3.3.1.1. This high bonding strength also leads to high capillary pressures induced by the BMG melt. Based on the calculations in section 3.3.1.2, we found that the capillary pressures induced by the BMG melt is the same or higher than the external pressure applied for complete infiltration in other experiments, leading to spontaneous infiltration. This is true despite the high viscosity of the BMG melt because the length-scale of the ceramic scaffold is sufficiently large to accommodate the infiltration kinetics of the system according to Darcy's Law, as shown in section 3.3.1.3. However, infiltrating finer-scale scaffolds, *i.e.*, at the dimensions found in natural nacre, with this BMG would present a problem as the high viscosity of the BMG melt would prevent complete infiltration (Fig. 11). This indicates that for future synthesis of nacre-like materials using infiltration, it is critical to observe the viscosity, wettability, and length-scale of the scaffolds to find feasible processing conditions.

SECTION 3.3.1.1 Work of adhesion calculations

The excellent wettability allowed spontaneous infiltration of the nacre-like alumina scaffolds at very rapid rates (10 min hold time) without the need for applied pressure. To characterize the critical characteristics for this infiltration behavior, the thermophysical properties and wetting behavior of the BMG melt were evaluated. The surface tension of the Zr-based BMG at its melting point was estimated at 1.24 $N \cdot m^{-1}$, making it comparable to other Zr-based BMGs like Vitreloy 1 or Vitreloy 106.[59] Interestingly, this value showed only a small deviation (~6%) from the calculation based on the rule of mixtures (1.32 $N \cdot m^{-1}$) of the surface tension of the pure components (1.48 $N \cdot m^{-1}$, 1.35 $N \cdot m^{-1}$, 0.91 $N \cdot m^{-1}$, 0.87 $N \cdot m^{-1}$ and 1.1 $N \cdot m^{-1}$, respectively for Zr, Cu, Ag, Al, and Be at their melting point).[60] These estimates imply that the BMG melt did not display significant surface segregation, as is often found in molten alloys comprised of elements with low surface tension.[59] Moreover, it indicates that the wettability of the system was not affected by any segregation or evaporation of elements with low vapor pressure like Ag. Based on this assumption, the strength of bonding between the BMG melt and the alumina can be derived from the surface tension, γ, evaluated from Figure 2a and the final contact angles, θ, measured by the sessile-drop method (Fig. 3). Specifically, the alumina/BMG melt bond strength can be estimated by calculating the work of adhesion (W_i), *i.e.*, the energy required to reversibly separate the two materials, *viz*:

$$W_i = \gamma(1 + \cos\theta \ , \tag{3}$$

which yields values of W_i of 2.43 $J \cdot m^{-2}$ and 2.33 $J \cdot m^{-2}$ at 1153 K and 1273 K, respectively. These values are much higher than those for non-reactive metal/Al_2O_3 couples (0.2 – 1.5 $J \cdot m^{-2}$)[61], indicating the strong chemical interaction between the BMG melt and alumina. This confirms how reactive wetting of alumina by the BMG melt can induce spontaneous melt infiltration into the nacre-like ceramic scaffolds without the need for external pressure.

SECTION 3.3.1.2 Capillary pressure calculations

The spontaneous melt infiltration is driven by capillary pressure (ΔP), where:

$$\Delta P = \frac{4\gamma cos\theta}{D_e} \ , \tag{4}$$

and where D_e is the equivalent diameter of pores in the scaffold. The equivalent diameter, which is a function of reinforcement size and porosity, is equal to the capillary diameter for a single cylindrical tube. Considering that the pore structure in the nacre-like scaffolds is anisotropic, which is similar to a fibrous preform, here we use the relationship derived for fibrous preforms to describe the equivalent diameter of the nacre-like alumina scaffolds:[62]

$$D_e = \frac{4}{F}\frac{e}{(1-e)}D_{Al2O3} \ , \tag{5}$$

where F, e, and D_{Al2O3} are, respectively, the form factor, porosity and average thickness of lamellae in the scaffolds. The form factor, which is dependent on the flow direction of a liquid in a scaffold, is 4 for the flow parallel and 2 for the flow perpendicular to fiber alignment.[62] Assuming a value of $F = 3$, which is the average between these two boundary cases, and considering the measured alumina thickness and volume fraction shown in Figure 5 of the main text, the equivalent diameters of the lamellar and brick-and-mortar scaffolds were estimated to be 17.5 μm and 7.5 μm, respectively. The estimate is reasonable in that those values are close to the thickness of the metallic mortar (13.3 ± 4.7 μm and 4.8 ± 4.2 μm, respectively) in the alumina/glass materials. The capillary pressures induced on the BMG melt were estimated as 277 kPa and 270 kPa for the lamellar scaffolds and 418 kPa and 403 kPa for the brick-and-mortar scaffolds at 1153 K and 1273 K, respectively. The pressure values at both temperatures were similar to each other due to the weak temperature dependence of the surface tension and final contact angle (Figs. 2a and 3). The result is that we achieve spontaneous melt infiltration because the capillary pressures induced by the BMG melt is the same or higher than the external pressure necessary for complete infiltration in other experiments. The estimated pressure is on the same order of magnitude as the external pressure required to fabricate particulate BMG matrix composites[34] (550 kPa, 50 vol.% Mo, Nb, and Ta, 30 - 200 μm in diameter), and two orders of magnitude higher than the external pressure required for the fiber-reinforced BMG matrix composites[35] (6.9 kPa, 80 vol.% W, 250 μm in diameter). Thus, the spontaneous infiltration of the nacre-like scaffolds with the BMG melt can be deemed to result from the high capillary pressure.

SECTION 3.3.1. Calculation of the kinetics of infiltration

The viscosity of the BMG at its melting point was estimated to be 2.12 × 10^{-1} Pa·s, which is two orders of magnitude higher than that of pure components at their melting point (~10^{-3} Pa·s).[26,27] This high viscosity is typical for the BMGs with high glass-forming ability due to the small amount of free volume in the liquid state.[59,63] However, the higher viscosity is unfavorable for melt infiltration in that it delays complete infiltration, which is dependent on the fluid velocity in a scaffold. The infiltration kinetics between the BMG melt and nacre-like alumina scaffolds in this study can be evaluated by Darcy's law[27] assuming one-dimensional infiltration of the melt through the scaffold:

$$h^2 = \frac{2k\Delta P}{e\eta} t \,, \tag{6}$$

where h is infiltration height, t is infiltration time, and k is permeability of a scaffold. Figure 11 shows the infiltration height of the BMG melt at 1153 K under different values of permeability of the brick-and-mortar scaffold in the range from 10^{-18} m^2 to 10^{-15} m^2. The calculation indicates that the brick-and mortar scaffold, which has an actual infiltration height of 1.25 mm that is half of the width of the scaffold (2.5 mm), can be infiltrated within 10 min if the permeability of the brick-and-mortar scaffold is higher than 7 x 10^{-17} m^2. The estimated permeability is reasonable in that the scaffolds with ceramic fraction of up to 80 vol.%, showed their permeability in the range from 10^{-14} m^2 to 10^{-12} m^2.[27,28,64,65] Thus, the melt infiltration of the nacre-like scaffolds in this study can be completed within 10 min despite the high viscosity of the BMG melt.

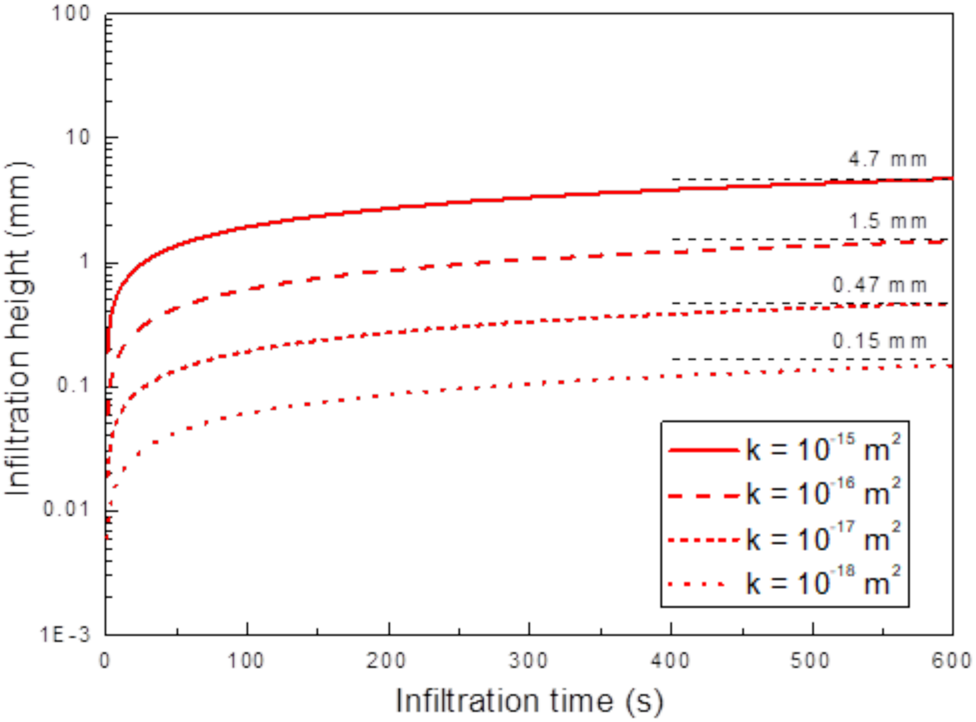

Figure 11. Estimated infiltration heights of bulk-metallic glass melts into alumina. Estimated infiltration heights of the BMG melt at 1153 K, assuming different values of permeability of the brick-and-mortar scaffold in the range from 10^{-18} m^2 to 10^{-15} m^2. The calculation shows that the melt infiltration of the nacre-like scaffolds in this study can be completed within 10 min despite the high viscosity of the BMG melt.

However, it should be noted that the permeability of a scaffold is proportional to the square of the reinforcement size.[27] In this study, the micron-scale brick-and-mortar scaffolds exhibited a lamellae thickness of 22 μm, whereas the brick-and-mortar structure of natural nacre is some two orders of magnitude finer, with a mineral thickness of ~250 nm.[66] Accordingly, synthetic nacre-like scaffolds made this fine-scale, although reflecting the true architectural scale of the natural material, would be far more difficult to infiltrate as the nano-scale features would induce a four orders of magnitude smaller permeability than for micron-scale structures, which would result in very slow kinetics of melt infiltration using the BMG (Fig. 11). Thus, for the future synthesis of nano-scale nacre-like hybrid materials by melt infiltration, the length-scale of the scaffolds, together with the viscosity and wettability of a molten alloy, will need to be carefully considered to design feasible processing routes.

Assuming the slowest case that the half of width (1.25 mm) of the brick-and-mortar scaffold was fully infiltrated by the BMG melt in 10 min at 1153 K, the minimum infiltration rate in this study can be estimated as 7.5 $\mathrm{mm \cdot hr^{-1}}$. The pressureless infiltration rate of Zr-based BMG into the brick-and-mortar alumina structure is higher than that of $Al_{94.5}Mg_{5.5}$ alloy into 62 vol.% particulate alumina scaffolds (3.3 $\mathrm{mm \cdot hr^{-1}}$ at 1173 K)[67]. Compared to the Al-Mg alloy which requires incubation time to wet the alumina due to the removal of the native oxide layer on the molten alloy, the BMG melt perfectly wets the alumina within several tens of seconds. Thus, the rapid infiltration in the alumina-BMG system is advantageous to control the interfacial strength that is affected by the chemical reaction at elevated temperatures.

SECTION 3.3.2. Nature of the ceramic/metal interface.

The temperature used for infiltration had a marked effect on the flexural strength and fracture toughness of both the lamellar and brick-and-mortar structures. This is particularly clear for the samples with a nacre-like architecture, where samples infiltrated at 1153 K compared to the materials infiltrated at 1273 K displayed a factor of four lower strength, yet a factor of three higher toughness, caused by stable crack growth (and rising R-curve behavior) rather than sudden catastrophic fracture. The latter characteristic of sustaining stable cracking following crack initiation, without immediate catastrophic failure, represents an essential property of structural materials. For the case of the 1273 K infiltrated brick-and-mortar materials, this resulted from significant crack propagation along the BMG-mortar/alumina-ceramic interfaces. Indeed, all these strength and toughness properties are primarily related to the nature of these interfaces.

In metal-ceramic systems showing reactive wetting, the interfacial bonding is affected by the chemical reaction between melt and ceramic.[41] Furthermore, as noted above, the BMG melt infiltrated into the scaffolds can be partially or fully crystallized during solidification due to the interface that acts as a site for heterogeneous nucleation. Thus, the effect of temperature on the reaction and crystallization of the BMG mortar are vital issues to be considered to evaluate the interfacial bonding in these nacre-like alumina/glass ceramics. Figures 12a and 12b show the interface of the alumina/glass ceramics with a lamellar structure that were infiltrated at 1153 K and 1273 K. The material infiltrated at 1153 K (Fig. 12a) shows sharp interfaces between the metallic mortar and alumina, and a faceted crystalline (Zr_2Cu) phase with a thickness of 0.3 ± 0.2 μm. Any reaction products like ZrO_2 were not observed at the resolution of the SEM, indicating the slow kinetics of the reaction ($3Zr + 2Al_2O_3 \rightarrow 4Al + 3ZrO_2$) at 1153 K. The material infiltrated at 1273 K (Fig. 12b) shows erosion of the interface, which produces a rough boundary, due to the reaction between the BMG melt and alumina. It should be noted that voids (marked by yellow arrows) and cracks are concentrated in the layer with a thickness of less than 2 μm between the faceted Zr_2Cu phase and alumina (marked as A in Fig. 12b). The layer also contained round-shaped pores (marked by blue arrows) that were generated from grain pullout during mechanical polishing. Examining this morphology, it is clear that the interfacial intermetallic layer provides a weak interface that creates a tortuous path for crack propagation. This is further supported by the micro-cantilever experiments, which showed a clearly weaker interface strength for the 1273 K material (Figs. 10e and 10f) compared to the 1153 K material (Figs. 10c and 10d).

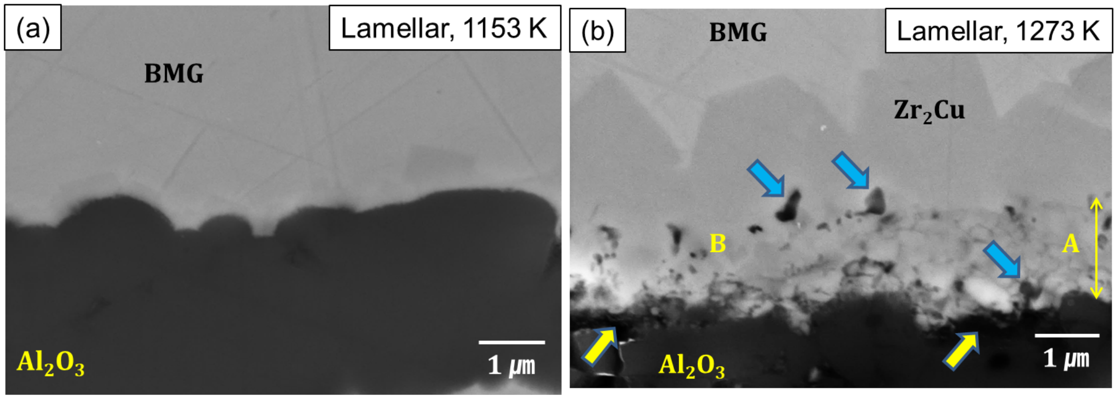

Figure 12. SEM micrographs showing the interface of the compliant-phase alumina/BMG ceramics with a lamellar structure infiltrated at 1153 K and 1273 K. (a) The material infiltrated at 1153 K shows sharp interface between the metallic mortar and alumina, and faceted crystalline (Zr_2Cu) phase with a thickness of 0.3 ± 0.2 μm. (b) In contrast, the interface of the material infiltrated at 1273 K displays the erosion of the interface, which produces a rough boundary, due to the significant reaction between the BMG melt and alumina.

During solidification, the undercooled BMG melt experiences abrupt volume contraction accompanied by crystallization. The Zr-based BMG used in this study shows about 1.5% volumetric contraction if the BMG melt is fully crystallized at its melting point.[42] To estimate the degree of volume contraction in the metallic mortar, the crystallinity of the metallic mortar is evaluated using a comparison of the heat of crystallization from the alumina/glass materials with the heat of crystallization from the monolithic BMG from the DSC analysis[43] (Fig. 6). The alumina/glass ceramics with a lamellar structure infiltrated at 1153 K and 1273 K has a crystallinity of 6% and 47%, respectively, which is comparable to the ratio between the thickness of the crystalline phase and that of metallic mortar in the materials with a lamellar structure (5% and 48%, respectively), as confirmed by microstructural analysis. Thus, a volume contraction of more than 0.7% takes place in the metallic mortar when the lamellar scaffold is infiltrated at 1273 K and then water quenched. Furthermore, the alumina/glass ceramics with the brick-and-mortar structure infiltrated at 1273 K experience a volume contraction of the metallic mortar of about 1.5% due to their high crystallinity (97%). The significant volume contraction within this material leads to the formation of interfacial cracks or voids, resulting in a low flexural strength in the nacre-like materials.

As the brittle interface forms at higher temperatures, the crack patterns are more tortuous, making it harder to propagate through the sample. The fracture toughness tests further support this hypothesis because the brick-and-mortar samples infiltrated at 1273 K show significant crack deflection compared to those infiltrated at 1153 K, as shown in Figure 8. The brick-and-mortar material infiltrated at 1153 K has a much higher flexural strength associated with its stronger ceramic/metal interface, but it appears to be too strong as the ceramic bricks fracture. In contrast, the brick-and-mortar samples infiltrated at 1273 K show several extrinsic toughening mechanisms (typical of natural nacre[1,4]), such as inter-brick displacements, brick pullout and crack deflections, leading to a significant increase in fracture toughness, compared to the corresponding structures infiltrated at 1153 K. However, the decreased flexural strength of samples infiltrated at 1273 K compared to the 1153 K ones is a strong indication that the alumina/BMG interfacial strength decreases with higher infiltration temperatures.

So, what do we learn from this work with respect to ceramic brick-and-mortar structures? Firstly, we have shown that it is possible to rapidly infiltrate a ceramic scaffold with a metal mortar without any applied pressure using reactive wetting. Moreover, this can result in a high strength structure due to a strong ceramic/metal (brick/mortar) interface in a high volume-fraction ceramic structure as shown for infiltration at 1153 K. However, for toughness we require a combined structure, ideally with high aspect-ratio fine-scale bricks, in conjunction with a mortar that permits some degree of inter-brick displacements to alleviate any locally high stresses. We achieved this with the structure infiltrated at 1273 K. Instead of outright catastrophic failure, the 1273 K infiltrated structures displayed markedly rising R-curve behavior (Fig. 8), where the inter-brick displacements serve to stabilize the growth of incipient cracks, over crack extensions up to 1 mm, with crack-growth toughness rising to the order of 14 $\text{MPa}\cdot\text{m}^{1/2}$. This is what nacre-like structures can offer. The limited inter-brick displacements can lead to crack deflection and most importantly brick pull-out and crack bridging, which act to stabilize crack growth; there is little change in crack-initiation toughness as the extrinsic toughening mechanisms solely enhance the crack-growth toughness.[6] This is also underlined by the microfracture experiments (Fig. 10), which clearly show that the interface strength is rather poor and most toughening arises from the microstructural alignment with respect to the crack path. A significant increase in initiation toughness is conceivable but must involve strengthening of the interface properties.

Clearly, the *Achilles' heel* of these structures is that the inter-brick displacements need to be *within* the mortar and not along the interface, as in the present high-toughness structure infiltrated at 1273 K. There are two problems with interface cracking. Whereas it still provides means to alleviate high local stresses and confer good toughness, weak interfaces invariably result in low strength, which one can readily appreciate by comparing the flexural strength of the 1273 K infiltrated structure to that infiltrated at 1153 K. Additionally, as noted above, the properties of metal-infiltrated nacre-like structures are predicted to be far superior to those of polymer-infiltrated structures because of the higher tensile/shear strengths of metal mortars;[13] however, for this to be realized, the inter-brick displacements naturally have to be within the mortar. For brick-and-mortar architectures, such behavior has been achieved in the high-toughness alumina-PMMA structures, where the ceramic-polymer interfaces were strengthened by grafting techniques,[14] and in coextruded (but very coarse-grained) alumina-nickel structures,[71] but to our knowledge it has yet to be achieved with nacre-like, fine-grained, metal-infiltrated ceramic structures.

SECTION 3.4. CONCLUSIONS

Concerning the damage-tolerant behavior of nacre-like (brick-and-mortar) alumina ceramics infiltrated with metallic mortar of a Zr-based BMG, the following conclusions can be drawn:

- Alumina-BMG ceramics with nacre-like structures with high alumina fraction up to 80 vol.% were rapidly synthesized using freeze-casting followed by melt infiltration. The excellent infiltration behavior, showing rapid and complete infiltration without any applied pressure, was attributed to the strong chemical interaction and excellent wetting behavior between the BMG melt and alumina. These results show that BMGs or any alloys with fast and excellent wettability on ceramic can be infiltrated in a ceramic preform with a high volume fraction and complex architecture to synthesize advanced bio-inspired structural materials with exceptional mechanical properties.
- The infiltration temperature has a marked effect on the interfacial properties of the resulting ceramic materials. The reactive wetting of BMG with alumina provided strong interfacial bonding when infiltrated at lower temperature (1153 K), but the chemical reaction at higher temperature (1273 K) and crystallization of the BMG melt resulted in the formation of weak ceramic-metal interfaces.
- These effects of infiltration temperature resulted in a trade-off between the strength and toughness of the compliant-phase ceramic materials. In samples infiltrated at 1153 K, the high interfacial strength led to higher strength in the alumina-glass ceramics, but low toughness due to the brittle nature of the metallic matrix. The samples infiltrated at 1273 K exhibited high fracture toughness, with stable crack growth, and hence resistance-curve behavior, up to stress intensities of 14 $\text{MPa}\cdot\text{m}^{1/2}$, due to interphase displacements between the bricks. However, their strength was low because these displacements (and ultimately failure) occurred along the interface as opposed to within the mortar layer, such that nacre-like failure mechanisms were not perfectly mimicked.

Chapter 4

Bioinspired Nacre-like Alumina with a Metallic Nickel Compliant-Phase Fabricated by Spark-Plasma Sintering

The objective of the present study is to an develop a “bottom-up” processing procedure that can make lightweight structural materials in the form of alumina with a fine-scale nacre-like brick-and-mortar structure but consisting of 95 vol.% ceramic with a metallic nickel compliant (mortar) phase because conventional top-down processing such hybrid ceramics with a metallic compliant phase is difficult as metals do not generally wet ceramics and thus cannot be readily melt-infiltrated into a (*e.g.*, freeze-cast) ceramic scaffold. Processing techniques such as freeze-casting (ice templating),[14,18,19,21,72–75] layer-by-layer alignment,[15,76] coextrusion,[71] magnetic platelet alignment and vacuum filtration assisted alignment[76,77] have been used to recreate brick-and-mortar microstructures. Using polymeric mortars, the nacre-like ceramics avoid sudden catastrophic failure by stabilizing slow crack growth in the form of crack-resistance (R-curve) behavior, although they cannot be used at elevated temperatures due to the presence of polymer phase.[14,15,76,78,79]

Theoretical micro-mechanical modeling[11] of synthetic “brick-and-mortar” materials though has indicated that metallic mortars may further enhance the strength and toughness properties (and naturally permit higher-temperature operation) due to their higher shear/tensile strength, provided the mortar strength does not exceed the brick strength. If the mortar strength does exceed the strength of the ceramic bricks, the bricks will simply fracture; this will immediately curtail the extrinsic toughening generated by crack bridging and brick pull-out, with the result that the structure will fracture catastrophically with a low toughness characteristic of the monolithic ceramic. However, to realize the full effect of a metallic mortar, the bonding between the mortar and the bricks must be strong enough so that the vital inter-brick displacements are *within* the mortar, and not along the brick-mortar interfaces. Nickel is an ideal metallic mortar because of its high melting point, strength, and ductility, but for it to function as a reliable compliant-phase surrounding the alumina bricks in the final nacre-like structure, it must not completely dewet from the ceramic.

We achieved this by coating alumina platelets with a comparable size to the mineral platelets in natural nacre with nickel oxide or nickel,[38] which were then aligned using slip casting prior to spark-plasma sintering (SPS) at 1100°C or 1200°C, as summarized in Figure 1. The advantage of the spark-plasma sintering is that it can limit grain growth and maintain the high aspect ratio of the platelets, given the correct composition and sintering conditions, due to its combination of high applied pressures and remarkably high heating rates of over 300°C/min, compared to conventional heating which is typically limited to ~20°C/min. Two batches of materials were cast: one made solely with Ni-coated platelets, the other with a mixture of NiO-coated and Ni-coated platelets. This study highlights the importance of including NiO-coated alumina platelets and optimal sintering temperatures to create materials with a strong interphase between the ceramic and metal, in order to develop bioinspired, “nacre-like”, ceramics with high toughness and acceptable strength for structural applications.

SECTION 4.1. METHODS

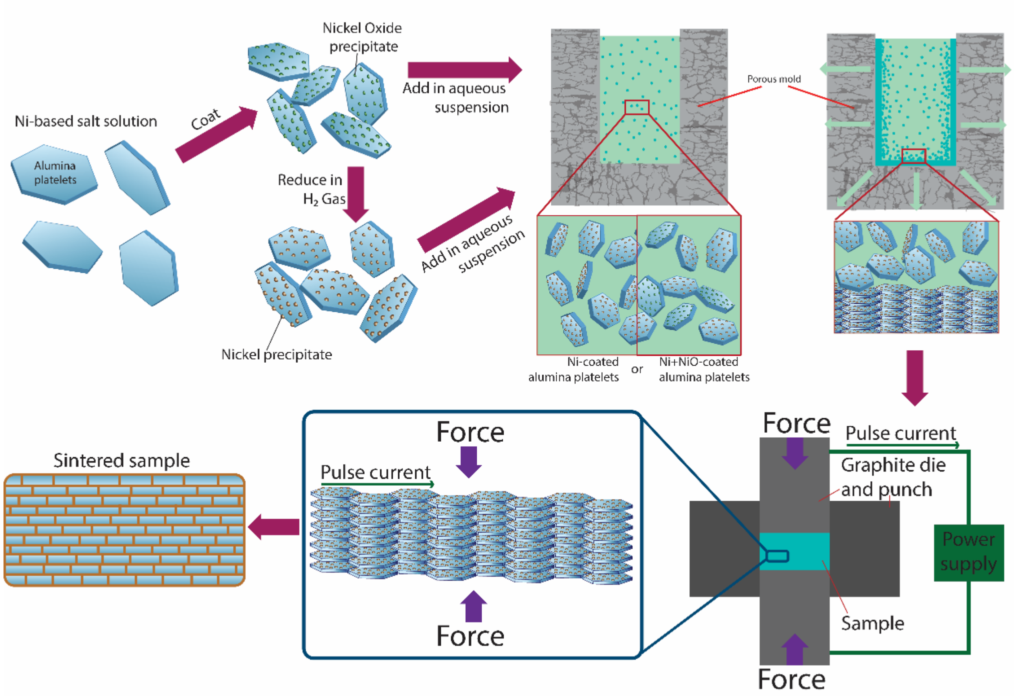

Figure 1. Schematic of slip casting and sintering of bioinspired materials

Slip casting of Ni- and NiO-coated alumina platelets, followed by spark-plasma sintering (SPS), was used to produce metal/ceramic bio-inspired composites. The starting alumina material (Alusion®, Antaria Limited, Australia) was in the form of platelet with a diameter of 8 ~ 10 µm and thickness of 500 nm ~ 800 nm (Fig. 2b). The aspect ratio of the diameter to thickness was ~10 – 20, which was selected to approximately match the size and aspect ratio as the aragonite mineral bricks in natural nacre[2].

SECTION 4.1.1. Coating Alumina Platelets

Before processing, the as-received alumina platelets were coated with a nickel shell using a coating procedure modified from Shen, *et. al.*[38], with a flow chart summarizing the processing of the core-shell platelets is shown in Figure 2a. The alumina platelets were suspended in deionized (DI) water with a concentration of 20g/L. The suspension was magnetically stirred and aqueous solutions of nickel sulfate heptahydrate (Sigma Aldrich, St. Louis, MO) and ammonium bicarbonate (Sigma Aldrich, St. Louis, MO), respectively with a molarity of 0.8M and 1.5M, were added into the suspension gradually to initiate the precipitation reaction. The solutions were maintained, with stirring, at 25°C for 12 hr. Subsequently, the platelets were washed and filtered four times with DI water, followed by drying in 60°C air for 12 hr. The dry platelets were calcinated at 600°C for 2 hr with a heating rate of 1°C/min in an air furnace (Thermolyne, Thermo

Scientific, Waltham, MA). A small subset of the platelets can be set aside as the NiO-coated platelets. The remaining platelets were treated for 2 hr under hydrogen at 600°C with a heating rate of 5°C/min using an Abar 90 furnace (Cherry Valley, IL) in order to reduce the NiO coating to nickel. The morphology and the element distribution of these platelets were characterized by scanning electron microscopy (SEM) (JSM-5700F, JEOL, Japan) and energy dispersive spectroscopy (EDS) (NORAN System 7, Thermo Fisher Scientific, Waltham, MA).

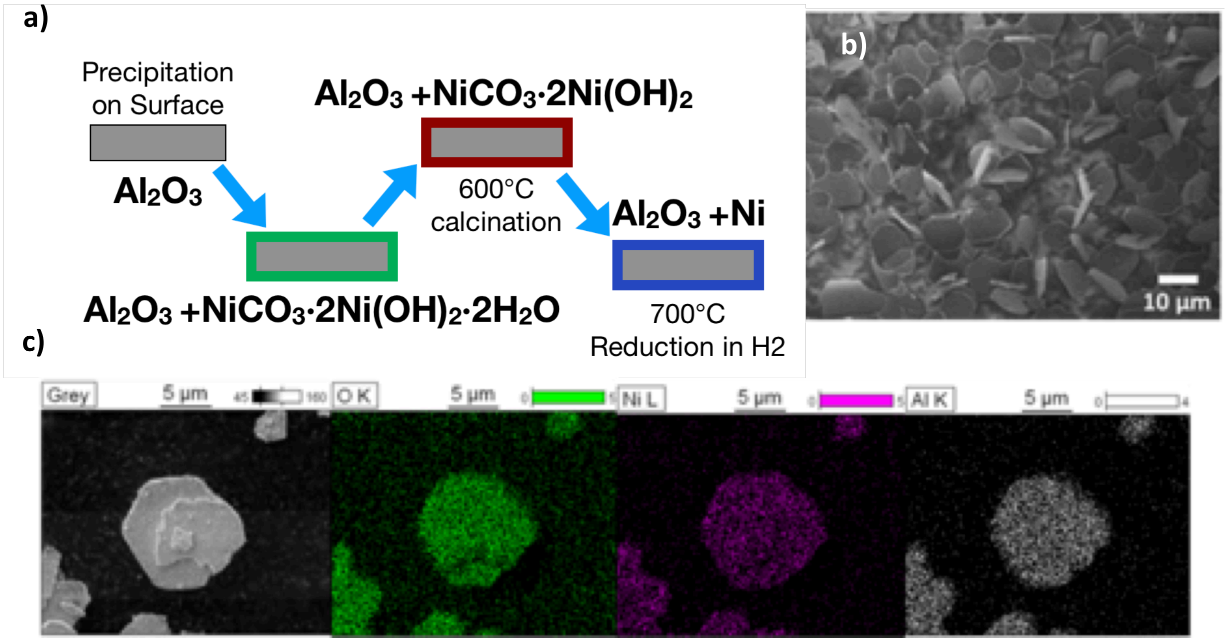

Figure 2. Fabrication of core-shell Ni/Al_2O_3 platelet (a) Flow chart summarizing procedure used to coat the alumina platelets with nickel. (b) SEM micrograph of alumina platelets after coating. (c) EDS mapping of nickel coated alumina platelets that indicate how the platelets have been completely coated with nickel.

SECTION 4.1.2. Slip Casting and Spark Plasma Sintering

In order to build nacre-like ceramic/metal composites, the coated alumina platelets have to be pre-aligned and subsequently densified, as summarized in Figure 1. Slip casting of slurries with ~50 wt.% solid loading was selected to pre-align the platelets and to produce green bodies with high packing density. To study the effects of composition on nickel wetting behavior over the ceramic platelets, slurries with two different compositions were prepared: one where only Ni-coated platelets were sintered together and another with a mixture of 20 wt.% NiO and 80 wt.% Ni-coated alumina platelets. The suspensions, which contained 10 vol.% polyvinyl alcohol (PVA) 22000 (VWR, Belgium) and 4 vol.% Dolapix CA (Zschimmer & Schwarz, Germany) to aid with green body strength and dispersion, were manually stirred and degassed under a vacuum. The suspensions were mixed with 63 vol% water using a Thinky ARE-250 planetary mixer for 2 mins at 2000 revolutions per minute and 800 rotations per minute with a 2-minute degassing step in between the mixing step. The slurries were then poured into a pre-prepared cast mold and left to settle for one day. The resulting samples were subsequently dried at 37°C for 24 hr and then baked at 100°C for 48 hr. The bulk pellets consisting of core-shell platelets were placed into a 20-mm cylindrical graphite die for uniaxial pressing. The polymer binder in the pellets was burnt out in an inert argon atmosphere at 500°C, using a conventional graphite furnace (FCT Systeme, Effelder-Rauenstein, Germany), with a 1-hr hold time, with an initial heating rate of 1°C per minute.

To form the actual compliant-phase ceramic, spark-plasma sintering was chosen as the sintering technique to bond the coated alumina platelets together. In the present work, the sample was compressed between two graphite punches inside a 20-mm diameter, cylindrical graphite die, and heated by passing an electrical current through it. Specifically, our materials were sintered using an SPS furnace (HPD 25/1 furnace, FCT Systeme, Germany) under vacuum at 1100°C and 1200°C for 10 mins with an applied compression load of 55 MPa, before being slowly cooled to room temperature. The resulting samples were measured using the Archimedes method. A cross-section of the aligned alumina platelets after uniaxial pressing is shown in Figure 3.

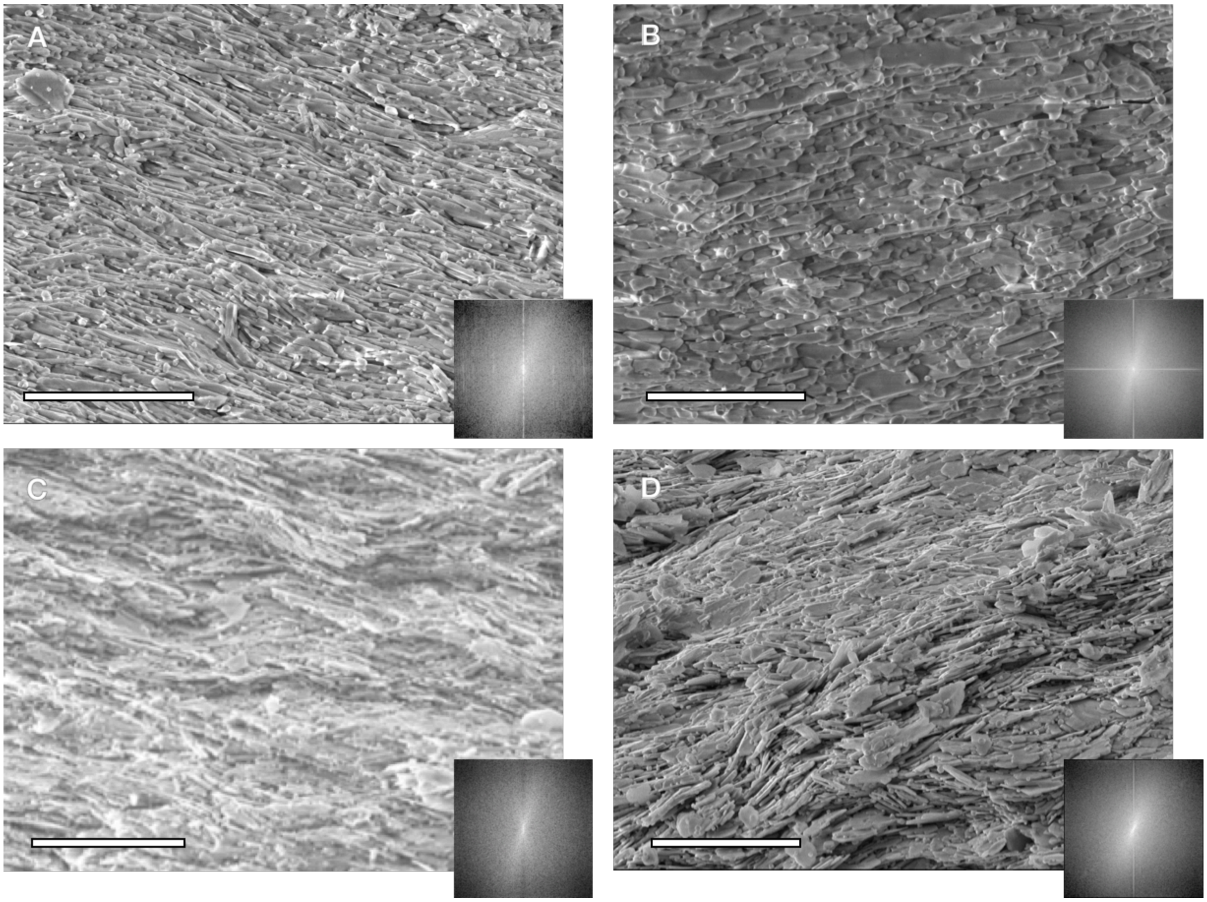

Figure 3. Scanning electron micrographs of the fracture surfaces of Ni+NiO-alumina samples sintered at 1100°C (A) and 1200°C (B) and Ni-alumina samples sintered at 1100°C (C) and 1200°C (D). The insets are fast Fourier transforms obtained from each SEM image. Based on the anisotropic nature of the fast Fourier transformed images, it is clear that samples were well aligned. It is particularly interesting to note how the basal planes are facing a uniform direction, avoiding any stacking card faults. All scale bars represent a length of 30 µm. In this image, it is clear that samples are well aligned and a particularly interesting note is how the basal planes are facing a uniform direction, avoiding any stacking card faults.

SECTION 4.1.3. Mechanical Testing

To prepare for microstructural characterization and mechanical testing, the sintered samples were cut perpendicular to the aligned direction with a diamond coated saw and carefully polished using a diamond grinding discs with a final polish at 0.5 µm. The resulting 12-mm long beams for flexural strength and fracture toughness testing had a square cross section of ~2.5 x 2.5 mm with a length of 12 mm, in general accordance with the respective ASTM D790[81] and ASTM E1820 Standards[55]. Flexural strength was measured on unnotched samples loaded in three-point bending (with a loading support span of 10 mm) on an Instron 5944 electro-mechanical testing system (Instron Corporation, Norwood, MA) at a displacement rate of 1 mm/sec.

Corresponding fracture toughness measurements were conducted using notched versions of the same samples, *i.e.*, single edged-notched bend SEN(B) samples. The notches were initially made using a low-speed diamond saw, before the notch root was sharpened using a micro-notching technique involving the polishing of the root with a razor blade immersed in a 6-µm diamond slurry under a steady load. With this technique, the resulting root radii of the notches averaged between 6 and 20 µm. The samples were then tested with an *in situ* Deben MicroTest 2kN (Deben, UK) three-point bending rig (with a 10 mm loading span) at a displacement rate of 0.033 mm/min mounted inside a Hitachi S-4300SE/N (Pleasanton, CA) scanning electron microscope (SEM) measure the crack-initiation fracture toughness and any subsequent subcritical crack growth, *i.e.*, the crack resistance or R-curve, while simultaneously measuring the crack path and imaging in real time the interaction of this path with the microstructural features.

Further details are given in the ASTM Standard E1820[55] and a previous study[14] for fracture toughness measurements.

SECTION 4.2. RESULTS

SECTION 4.2.1. Processing Methodology

By examining the fracture surfaces of sintered samples of the our compliant-phase Ni-Al_2O_3 and Ni+NiO-Al_2O_3 ceramics in the SEM (Fig. 3), it is readily apparent that slip casting successfully aligned the micron-scale alumina platelets coated with nickel. Moreover, following SPS, the materials were completely sintered, showing a dense texture with nickel content in the final processed material of ~5 wt.%.

The addition of the nickel oxide-coated platelets is key for improving the nickel wetting over the ceramic platelets and achieve a homogeneous distribution within the material.[82] Two different batches of materials were cast in order to study the effects of slip composition on the final sample. One batch had nickel-coated alumina platelets while the other had a mixture of nickel oxide-coated platelets and nickel-coated platelets. Nickel oxide was used because as the oxide of the metal, it can be used to create favorable wetting conditions with nickel. Past work on wetting angles between metals and oxides have shown that low oxygen concentrations, such as a heavily reducing graphite environment under vacuum, can lead to dewetting between the materials, as discussed in section 2.3.[61] However, with controlled increases in oxygen concentration, wetting angle decreases without any reaction at the interface. As a result, the addition of nickel oxide serves to limit dewetting by the nickel. After sintering at 1100°C, samples made with a blend of

Ni-coated and NiO-coated platelets were subject to limited nickel dewetting and platelet-to-platelet sintering (Fig. 4a), whereas those made with solely Ni-coated platelets were susceptible to dewetting (Fig. 4c), leading to small agglomerates of nickel between the alumina platelets. However, there are some discontinuities in the nickel layers when the Ni+NiO-coated alumina were sintered at 1100°C (Fig. 4e). Samples sintered at 1200°C and above, for both Ni+NiO-coated and Ni-coated alumina compositions showed evidence of more extensive nickel dewetting and alumina grain growth (Fig. 4b, 4d, and 4f), leading to a breakdown of the brick-and-mortar structure. This was confirmed using energy-dispersive x-ray spectroscopy (EDS) in the SEM; line scans shown in Figure 4a and 4b indicate larger aggregations of nickel in samples sintered at 1200°C, compared to the sheets of interphase nickel in the 1100°C samples. Samples sintered below 1100°C did not fully sinter, and thus were not considered for further study.

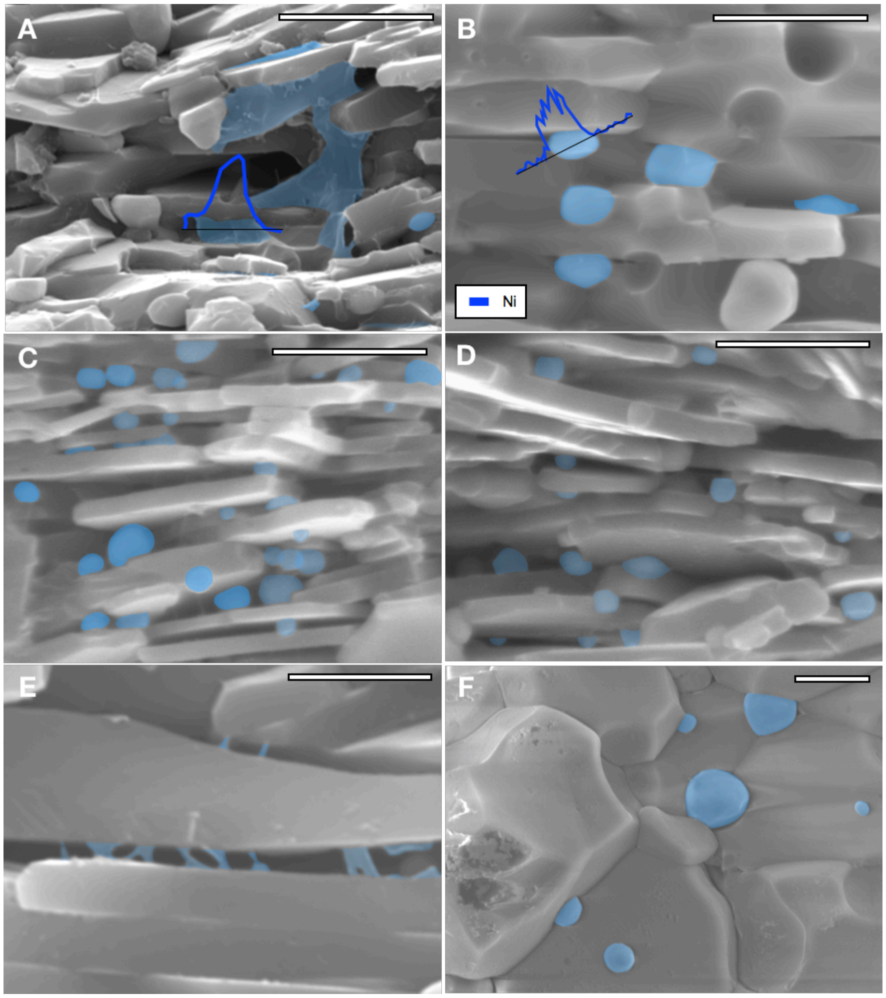

Figure 4: SEM micrographs illustrating the nature of the nickel "mortar" formed within Ni+NiO-coated alumina and Ni-coated alumina. In the Ni+NiO samples, sintering at (a) 1100°C generates sheets of nickel that sits between the alumina platelets with some discontinuities at higher magnification (e), whereas sintering at (b) 1200°C causes the nickel to dewet and act as ball-shaped impurities in the alumina. When sintered at (f) 1300°C, the Ni+NiO samples display further nickel dewetting and alumina grain growth. For the Ni-coated alumina material, dewetting of the nickel mortar, is observed at both sintering temperatures, (c) 1100°C and (d) 1200°C. The blue lines are EDS line scan results to show changes in nickel content. The scale bars are 5 μm for all images, except (e) where it is 2 μm.

SECTION 4.2.2. Mechanical Properties

The mechanical properties of the compliant-phase Ni-alumina and Ni+NiO-alumina ceramics, for the two conditions of spark-plasma sintering at 1100° and 1200°C, were evaluated with respect to their flexural strength and fracture toughness and compared with the corresponding properties of fine-grained monolithic alumina. The flexural strength of alumina is typically on the order of 410 MPa[83]; although it clearly depends on such factors as grain size, sample size, and so forth, an in-depth series of measurements gave values varying between 267 and 358 MPa.[84] The mean flexural strength of our Ni+NiO-alumina sintered at 1100°C was 297.1 ± 43.1 MPa with some samples displaying strengths as high as ~350 MPa. Conversely, when extensive dewetting of nickel occurred, as seen in the corresponding the Ni-alumina materials, the flexural strength of the sample decreases markedly to ~85± 9.15 MPa. The mean flexural strength of the Ni/NiO-alumina sintered at 1200°C was 246.5 ± 30.4 MPa, which again is nominally comparable to that of monolithic alumina (Fig. 5a), but it is 17% lower than that of our 1100°C Ni+NiO-alumina ceramic. The Ni-alumina sample sintered at 1200°C, which also displays extensive dewetting of nickel, has a flexural strength of ~118 ± 19.3 MPa, which is fairly comparable to the strength of its counterpart sintered at 1100°C.

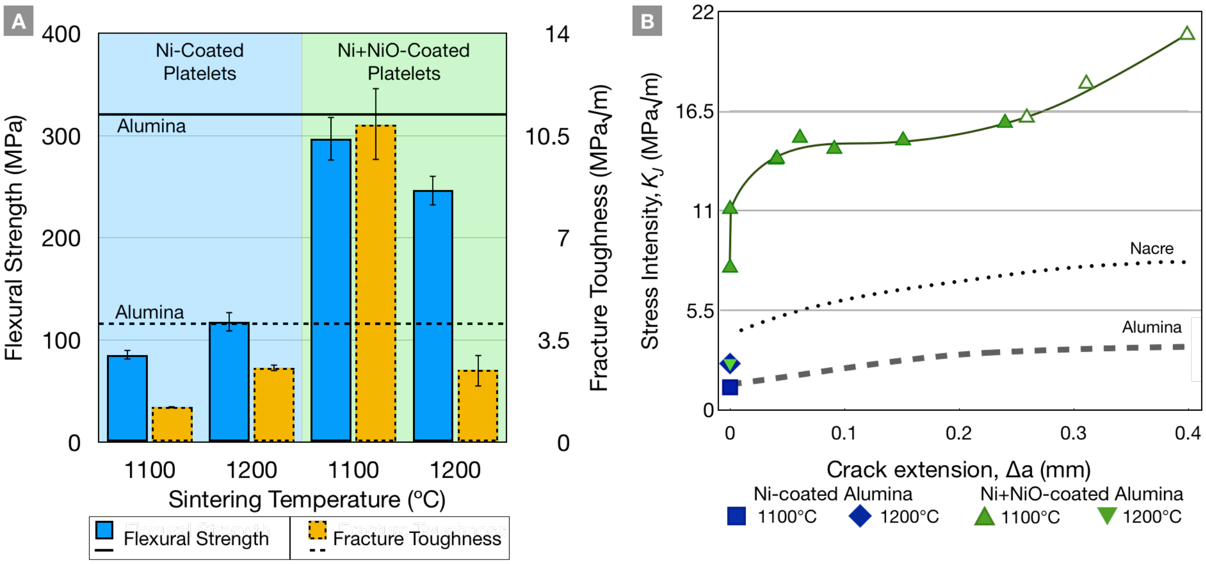

Figure 5- Mechanical testing results for samples summarized in bar graphs and crack-resistance curves. Summarized mechanical testing results in bar graphs, showing (A) flexural strength and fracture toughness test results. The Ni+NiO-coated samples sintered at 1100°C show (B) R-curve behavior that enhances the fracture toughness of the material from ~8 MPa·m^{½} to 16 MPa·m^{½} associated with slow (stable) crack growth, toughness behavior that is far superior to that of fine-grained monolithic alumina (and even nacre). In contrast, the samples sintered at 1200°C or with only Ni-coated platelets display no R-curve behavior and fracture catastrophically with a fracture toughness lower than alumina. The unfilled points are data points that are not strictly "valid" according to ASTM Standard E1820 because they exceed the maximum crack extension for the size of the test specimens. SEM micrographs with 5 µm scale bars illustrate salient toughening mechanisms in the Ni+NiO-coated alumina samples sintered at 1100°C.

Whereas the strength does not vary that much with the appropriately sintered compliant-phase aluminas and monolithic alumina, the fracture toughness shows stark differences between these materials. All the Ni-alumina samples fractured catastrophically at a particularly low toughness without any evidence of stable crack growth, *i.e.*, with no R-curve behavior (Fig. 5b). Specifically, Ni-alumina samples sintered at 1100°C had an average fracture toughness of 1.2 ± 0.05 MPa·m$^{1/2}$, whereas those sintered at 1200°C, had an average fracture toughness of the Ni-alumina samples are 2.55 ± 0.21 MPa·m$^{1/2}$. These values are even less than those reported for monolithic alumina.[85]

The most critical result is how the presence of NiO-coated as well as Ni-coated alumina platelets drastically affects the fracture toughness. Such Ni+NiO-coated alumina samples sintered at 1100°C display stable crack-growth behavior, as indicated by the rising R-curve behavior shown in Figure 5b, which elevates the toughness by a factor of two from ~7.8 MPa·m$^{1/2}$ to 15.9 MPa·m$^{1/2}$ by stabilizing the extension of subcritical cracks.[***] Such R-curve behavior for the Ni+NiO-alumina sintered at 1100°C represents a six-fold increase in fracture toughness compared to samples sintered at 1200°C, which suffer sudden catastrophic fracture at 2.48 ± 1.10 MPa·m$^{1/2}$ with no evidence of rising R-curve behavior. Indeed, our compliant-phase Ni/NiO-alumina samples sintered at 1100°C are also significantly tougher (by ~2-4 times) than monolithic alumina.

SECTION 4.3. DISCUSSION

In this work, we have made a bioinspired "nacre-like" alumina ceramic in the form of a "brick-and-mortar" structure where the size and aspect ratio of the alumina bricks approximately matches that of nacre, with a volume fraction of ceramic over 90%, again matching nacre. We have further accomplished the difficult task of creating a metallic (nickel) mortar between the alumina bricks by applying a nominally "bottom-up" approach of using Ni- and NiO-coated alumina platelets, oriented through slip casting, and bonded using spark-plasma sintering. With the current processing method of metal-coated ceramic platelets, slip casting followed by isostatic pressing within the SPS, clearly provides for relatively good alignment of the platelets. This is important as if the platelets are not well-aligned, porosity can be induced such that the material cannot be sintered to full density, with a resulting loss in strength and toughness.

Too high sintering temperature is clearly detrimental too, as seen in samples sintered at 1200°C. Despite the addition of NiO-coated platelets, the Ni still dewets and forms balls of metal. One contributing factor is the highly reducing atmosphere of the SPS which can deplete oxygen in the system at higher temperatures, making it difficult to prevent nickel dewetting. Additionally, the platelets are able to sinter together to form a material that can be best described as alumina with a long-grained microstructure and nickel-based inclusions, with a consequent dramatic loss in toughness comparable to pure alumina. The dewetted nickel phase clearly no longer functions as a compliant-phase mortar, but it introduces defects into the alumina microstructure, leading to a lower strength and fracture toughness than the monolithic alumina.

[***] Note that the data points beyond 15.9 MPa·m$^{1/2}$ are not representative of the fracture toughness of the material. The "concave-up" shape of the R-curve is a strong indication that the sample is too small compared to the extent of crack-tip shielding, such as crack bridging; as such, it is not indicative of the inherent properties of the material, similar to how plasticity affects the linear-elastic fracture mechanics fracture toughness of materials tested in specimens that are not large enough compared to the size of the crack-tip plastic zone. The result is that the measured fracture toughness values become size-dependent.

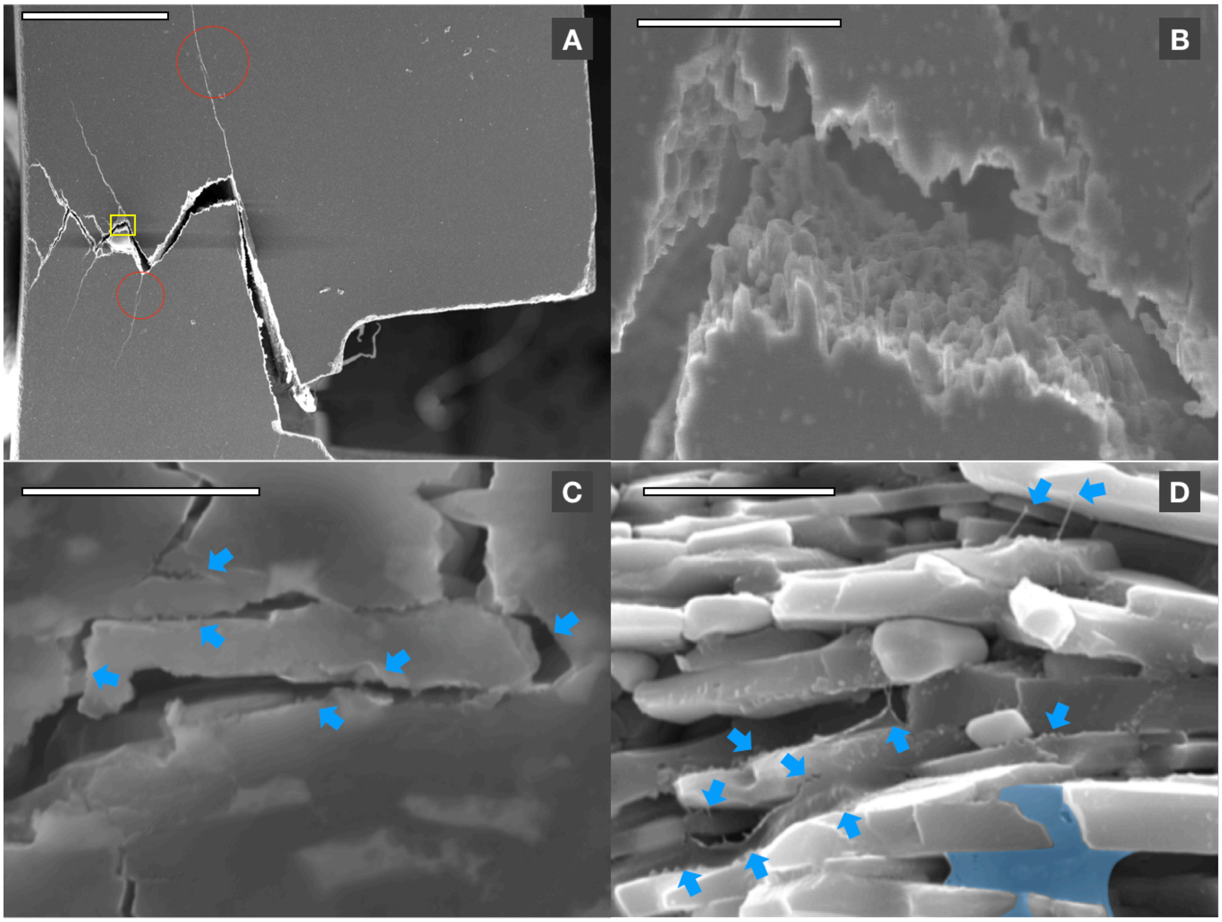

Figure 6: SEM images illustrating the salient toughening mechanisms in the Ni+NiO-coated alumina samples sintered at 1100°C. (a) Macroscopic crack path showing significant crack deflection and elastic bridging at the length-scale of hundreds of micrometers (the red circles indicate signs of uncracked ligament bridging). (b) Crack bridging by ceramic "brick" pull-out at the <10 µm length-scale; this image represents the yellow inset in (a). SEM micrographs with 5 µm scale bars for (C) and (D) illustrate evidence of nickel tearing. Although there is some Ni dewetting based on the brighter areas in (C), evidence of nickel tearing (highlighted by blue arrows) and ceramic "brick" pull-out are observed. The fracture surface in (D) shows more signs of nickel tearing in between the platelets, indicated by the blue arrows, with untorn nickel in the blue region. This suggests that the inter-brick displacements and the resulting inter-brick failures may occur *within* the nickel mortar phase rather than along the Al_2O_3-ceramic/Ni-metal interface.

In contrast, the Ni/NiO alumina materials sintered at 1100°C were left with a distributed nickel phase along the ceramic brick interfaces. The stretched and torn pieces of nickel shown in Fig. 6c and 6d suggest that the inter-brick displacements and hence the eventual failure path in these materials occurred *within* the nickel mortar layers. This phenomenon, which is very significant for the resulting toughness was likely caused by the combination of the rapid sintering using SPS, the pressure that aids flow of melted nickel, and the appropriate oxygen content to aid wetting. This allows for limited inter-block displacements – the key mechanistic feature in nacre-like materials for conferring toughness through the plasticity of the mortar phase.

This key for limited inter-block displacements is an even coating or “sheet” of Ni between the bricks, which was only possible due to the addition of NiO-coated, as well as the Ni-coated, alumina platelets, which acts to prevent the dewetting of nickel during sintering. Although SPS is very powerful due to its rapid sintering capabilities and continuous applied pressure, without any equivalent rapid cooling processes, the nickel will dewet during the cooling half of the sintering process. By including these NiO-coated platelets, the material is encouraged to spread across the platelets, as opposed to dewet. As a result, we attained fully dense samples with a coating of nickel acting as the mortar between the bricks. By allowing the material to display crack bridging and deflection (Fig. 6a), brick pull-out (Fig. 6b), as well as mortar phase tearing (Fig. 6c, 6d), as observed in nacre, SPS processing at 1100°C generates an impressive ceramic with a flexural strength on the order of monolithic (untoughened) alumina but with a toughness some 5 to 8 times larger.

While there is a remarkable improvement to the mechanical properties of the material, the mechanical properties of the materials produced using this technique still should be able to be further improved, according to micromechanical analysis.[11] Since the shear strength of nickel is significantly higher than PMMA, the modeling results indicate that the fracture toughness should increase along with the strength of the material. However, the materials produced in this study cannot match the fracture toughness found in some of the freeze-cast alumina/PMMA systems.[7] There may be several reasons for this. First, the ceramic content of the freeze-cast alumina/PMMA materials have a significantly lower ceramic content at ~80 vol%, leaving a higher ductile phase to improve the fracture toughness of the material. Whereas it is clear that the inter-brick displacements essential for toughness in freeze-cast alumina/PMMA materials occur within the polymer phase, with associated inelasticity, damage and tearing of the PMMA, in the alumina/Ni materials processed up until now, these displacements have occurred at the mortar/brick interfaces. This may be acceptable for toughness as it still permits inter-brick displacements but the interface failure “short-circuits” the benefits of the higher tensile and shear strength of the metal mortar, and more importantly results in low flexural strengths. Although the evidence in Fig. 6 suggests the inter-brick displacements in the present slip-cast/SPS compliant-phase ceramics occur within the metallic mortar phase rather than along the brick/mortar interfaces, we are not completely certain that this is always the case as the nickel layers are very thin and at times discontinuous (Fig. 5e), such that the nickel content in the current materials may be too low to act as a completely effective “lubricating” layer between the platelets. This issue still remains the “Achilles heel” of these brick-and-mortar ceramic structures – that of an effective metallic mortar with definitive strong bonding to the ceramic bricks - which has, as yet, to be satisfactorily realized. This implies that if the theoretical predictions for these synthetic nacre-like ceramics are right, there still may be compliant-phase ceramics that can be processed with even larger combinations of strength and toughness that have been recorded to date. This remains the grand challenge in the development of new bioinspired lightweight structural materials in the image of natural nacre.

Nevertheless, the results of this work illustrate how critical it is to incorporate an understanding of metal wetting on ceramics to create damage tolerant bioinspired ceramic with a metallic lubricating phase. The mechanical properties of our Ni+NiO-alumina ceramics have acceptably high strength and very high fracture toughness relative to other efforts in creating a bioinspired ceramic with a <10 vol% metallic phase (Fig. 7). On the basis of theoretical modeling,[14] these microstructural metrics match the optimal design for a nacre-like compliant-phase ceramic with a high volume fraction of ceramic, micrometer-scale ceramic bricks with a large aspect ratio (>10), and a metallic mortar. Slip-casting has been used previously to create nacre-like ceramics with a metallic mortar, but this involved magnetically-assisted procedures[39,86] and the toughness of the resulting alumina/copper or alumina/nickel materials were significantly lower than the ceramic materials developed here. Coextrusion methods have also been successful in achieving nacre-like structures with high volume fractions (>90 vol.%) of ceramic bricks and a metallic mortar, but these structures tend to be far coarser, with brick dimensions in the hundreds of micrometers. Ni-compliant-phase alumina ceramics processed this way can display good toughness exceeding 11 MPa·m$^{1/2}$, but invariably have very low flexural strengths of 110-160 MPa.[71] Indeed, this is the first nacre-like ceramic with a metallic mortar that displays the combination of an ambient-temperature strength comparable to monolithic alumina but with a four-fold increase in fracture toughness, a material which was only made possible by the use of NiO-coated, as well as Ni-coated, particles and rapid SPS processing at the correct temperature.

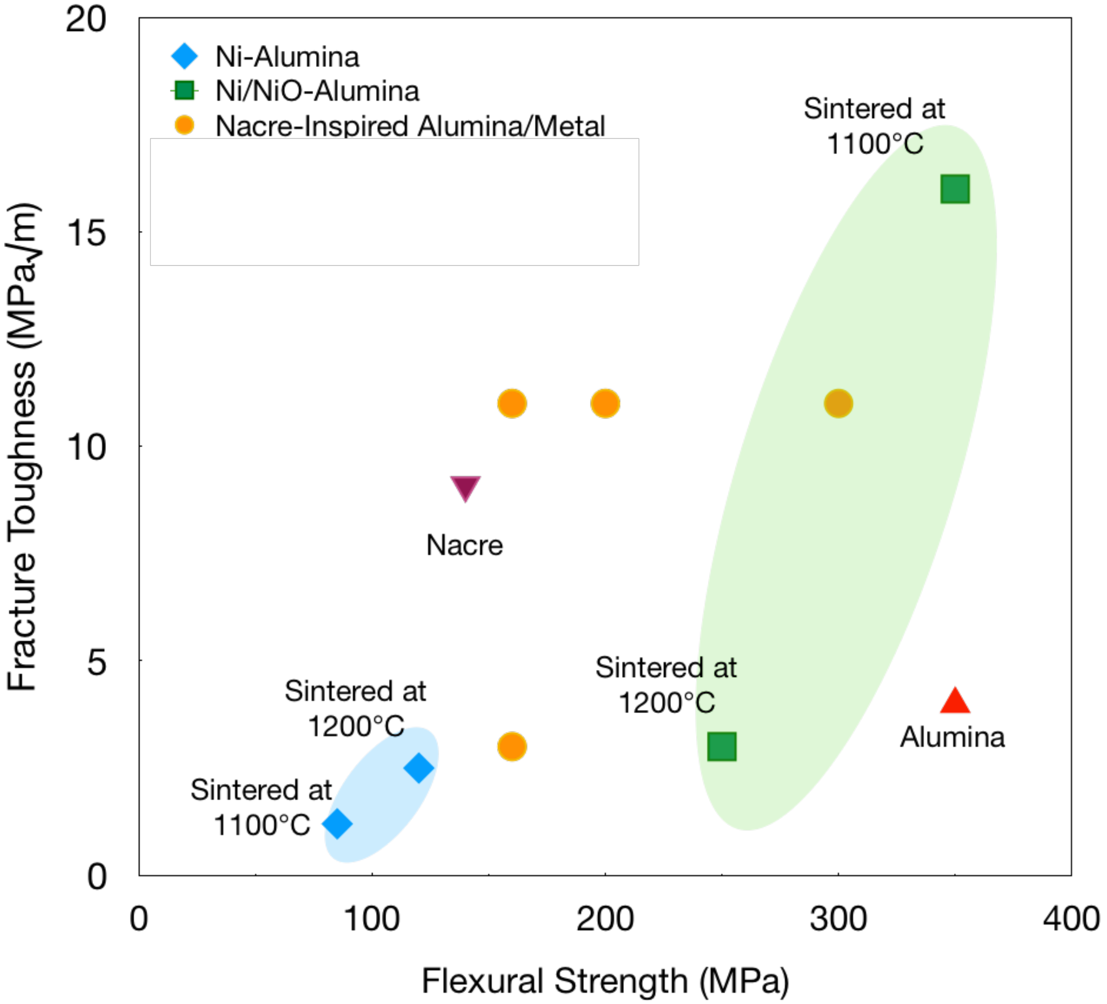

Figure 7: Comparison of materials produced in this study to other nacre-inspired alumina/metal composites. The reported mechanical properties of bioinspired (nacre-like) alumina ceramics containing less than 10 vol.% metallic mortar are compared to samples discussed in this chapter to illustrate how the composition, processing, and sintering temperature can affect their damage-tolerance (strength and toughness).[5,39,71,84,86–88]

SECTION 4.4. CONCLUSIONS

Using heterogeneous precipitation to form Ni- and NiO-coated micrometer-scale alumina platelets, with dimensions comparable to the mineral bricks in natural nacre, we have used slip casting to align the platelets into a brick-like configuration followed by spark-plasma sintering to create a nacre-like, brick-and-mortar, alumina ceramic structure comprising a high volume (~95 vol.%) of ceramic and 150-nm thin inter-brick layers of nickel acting as the mortar.

Based on the structural and mechanical characterization of these bioinspired structures, the following conclusions can be made:

1. Spark plasma sintering provides an effective way to sinter these materials while avoiding grain growth and nickel dewetting. However, although this was successfully achieved in the present work by sintering at 1100°C, sintering at a higher temperature (1200°C) caused the dewetting of the nickel which balled-up into discrete spheres, with the result that the material suffered a total loss in toughness through failed sudden catastrophic fracture.
2. Conversely, for the 1100°C SPS compliant-Ni phase alumina ceramics processed in this study, a flexural strength of ~300 MPa was achieved which is comparable to that of monolithic alumina, even with the inclusion of the nickel phase. Moreover, akin to natural nacre, the brick-and-mortar structure generated several extrinsic toughening mechanisms, notably ceramic brick pull-out leading to crack bridging and crack deflection, which resulted in stable cracking, R-curve behavior and a toughness of almost 16 $\mathrm{MPa{\cdot}m^{1/2}}$, four times larger than monolithic alumina.
3. The damage-tolerant properties of these compliant (metallic) phase ceramics may be further improved by maintaining a continuous metallic layer between the ceramic bricks, with a sufficiently strong ceramic-metal interface to ensure that all the micrometer-scale inter-brick displacements, which are essential for toughness, are confined to within the metallic layer. We believe that this will lead to even higher fracture toughness in bioinspired, nacre-like, ceramics, without compromising their strength.

Chapter 5

Summary and Future Work

Nacre has the brick-and-mortar microstructure that imparts damage-tolerance by using the mineral bricks for strength and the biopolymeric mortar to promote some degree of ductility and hence toughness. The sliding behavior within the mortar is essential for toughening, but it must be limited to retain the strength of the material. This is possible through a combination of features, such as the presence of ceramic bridges that connect the platelets, the nano-asperities on the platelet surfaces, and the tensile and shear strength of the biopolymers that act as a glue between the platelets[2]. There are multiple scales of features within the design of this very simple brick-and-mortar microstructure that enables high strength and toughness for this material. This study uses two processing approaches to recreate the microstructure of nacre with a metallic compliant phase. The processing approaches are top-down and bottom up approaches introduce different challenges to replicating the toughening mechanisms of this material.

In the top-down approach, a freeze-cast alumina scaffold is pressurelessly infiltrated with a BMG-forming alloy. The results indicate that pressureless metal infiltration is possible with BMG-forming alloy because it reactively wets the surface of alumina in approximately 10 seconds. The near-perfect wetting combined with how its viscosity is so sensitive to temperature makes it feasible to infiltrate a freeze-cast brick-and-mortar ceramic. However, there is a tradeoff between strength and toughness between materials infiltrated at 1273 K and 1153 K. This is caused by differences in interfacial strength between the two materials. When the material is infiltrated at 1153 K, the crack tends to be more tortuous and deflects along the interface between the ceramic and metallic phases. This leads to stable crack behavior and higher fracture toughness. However, its flexural strength is very low. This tradeoff occurs because as the material fails along the interface between the metallic and ceramic phases, it prevents the metallic mortar phase from dissipating any local stress concentrations. On the other hand, when the materials are infiltrated at 1273 K, the interfacial strength is higher and the flexural strength is comparable to monolithic alumina. It has a lower fracture toughness because its bricks tend to fail before any deformation occurs within the metallic phase because the mortar strength exceeds the strength of the bricks. As a result, tuning interface means tuning its macrostructural properties because the toughness of these materials is driven by the interfacial layer.

The bottom-up processing approach has illustrated potential in creating a nacre-like material by coating alumina platelets with nickel and sintering it together rapidly using spark plasma sintering. Slip casting has successfully aligned the platelets together. The addition of alumina platelets coated with nickel oxide in the slurry has provided enough oxygen within the highly reductive sintering conditions to limit dewetting between the nickel and alumina phases. Once the material has been sintered under the appropriate conditions, the material can replicate the damage tolerance found in nacre. Therefore, the critical components to create a nacre-like ceramic are good alignment between platelets, limited nickel dewetting, and adhesion between the brick and mortar.

As a result, under the appropriate sintering conditions, the bottom-up processing approach has several advantages compared to the top-down approach. It allows more control over the interfacial bonding conditions according to coating composition or what has been added to the slurry during casting. There are also less barriers to incorporating the mortar phase. Viscosity of the melt, interfacial reactions, and capillary pressures are limiting factors to how well infiltration methods can mimic the microstructural features and damage tolerance of its natural counterparts. The bottom-up processing technique can also recreate the size-scale of the brick-and-mortar microstructures or the hierarchical features of its natural counterpart, unlike its top-down processing counterparts.

Computational models reveal the potential to create new materials with unprecedented combinations of properties by using the design principles to mimic the strength and toughening mechanisms active in nacre. However, the materials produced in this work has not yet met the full potential set by these computational models. In the future, it would be beneficial to continue exploring the bottom-up processing techniques by incorporating roughness on the platelet surfaces, adding alumina nanoparticles in the slurry during casting to encourage bridging between platelets, recreating the bottom-up processing approach with platelets with various aspect ratios, and incorporating a thicker layer of nickel by depositing thicker layers of nickel on the surface of the alumina. Finally, these materials should be tested under high temperatures to find its properties in extreme environments. By meeting the projected strength and toughness found in computational models, these materials are extremely beneficial for aerospace, defense, and energy applications.

References:

1. Wegst, U. G. K., Bai, H., Saiz, E., Tomsia, A. P. & Ritchie, R. O. Bioinspired structural materials. *Nat Mater* **14**, 23–36 (2015).
2. Meyers, M. A., Chen, P.-Y., Lin, A. Y.-M. & Seki, Y. Biological materials: Structure and mechanical properties. *Prog. Mater. Sci.* **53**, 1–206 (2008).
3. Liu, Z., Meyers, M. A., Zhang, Z. & Ritchie, R. O. Functional gradients and heterogeneities in biological materials: Design principles, functions, and bioinspired applications. *Prog. Mater. Sci.* **88**, 467–498 (2017).
4. Shao, Y., Zhao, H.-P., Feng, X.-Q. & Gao, H. Discontinuous crack-bridging model for fracture toughness analysis of nacre. *J. Mech. Phys. Solids* **60**, 1400–1419 (2012).
5. Sarikaya, M., Gunnison, K. E., Yasrebi, M. & Aksay, I. A. Mechanical Property-Microstructural Relationships in Abalone Shell. in *Symposium R – Materials Synthesis Utilizing Biological Processes* **174**, (1989).
6. Launey, M. E. & Ritchie, R. O. On the Fracture Toughness of Advanced Materials. *Adv. Mater.* **21**, 2103–2110 (2009).
7. Song, F., Soh, A. K. & Bai, Y. L. Structural and mechanical properties of the organic matrix layers of nacre. *Biomaterials* **24**, 3623–3631 (2003).
8. Evans, A. G. *et al.* Model for the robust mechanical behavior of nacre. *J. Mater. Res.* **16**, 2475–2484 (2001).
9. Smith, B. L. *et al.* Molecular mechanistic origin of the toughness of natural adhesives, fibres and composites. *Nature* **399**, 761–763 (1999).
10. Barthelat, F., Tang, H., Zavattieri, P., Li, C. & Espinosa, H. On the mechanics of mother-of-pearl: A key feature in the material hierarchical structure. *J. Mech. Phys. Solids* **55**, 306–337 (2007).
11. Begley, M. R. *et al.* Micromechanical models to guide the development of synthetic 'brick and mortar' composites. *J. Mech. Phys. Solids* **60**, 1545–1560 (2012).
12. Barthelat, F. Designing nacre-like materials for simultaneous stiffness, strength and toughness: Optimum materials, composition, microstructure and size. *J. Mech. Phys. Solids* **73**, 22–37 (2014).

13. Espinosa, H. D., Rim, J. E., Barthelat, F. & Buehler, M. J. Merger of structure and material in nacre and bone – Perspectives on de novo biomimetic materials. *Prog. Mater. Sci.* **54**, 1059–1100 (2009).
14. Munch, E. *et al.* Tough, bio-inspired hybrid materials. *Science* **322**, 1516–20 (2008).
15. Bouville, F. *et al.* Strong, tough and stiff bioinspired ceramics from brittle constituents. *Nat. Mater.* **13**, 508–514 (2014).
16. Launey, M. E. *et al.* Designing highly toughened hybrid composites through nature-inspired hierarchical complexity. *Acta Mater.* **57**, 2919–2932 (2009).
17. Rempel, A. & Worster, M. . The interaction between a particle and an advancing solidification front. *J. Cryst. Growth* **205**, 427–440 (1999).
18. Naglieri, V., Bale, H. A., Gludovatz, B., Tomsia, A. P. & Ritchie, R. O. On the development of ice-templated silicon carbide scaffolds for nature-inspired structural materials. *Acta Mater.* **61**, 6948–6957 (2013).
19. Deville, S., Saiz, E., Nalla, R. K. & Tomsia, A. P. Freezing as a Path to Build Complex Composites. *Science* **311**, 515–518 (2006).
20. Deville, S. Freeze-Casting of Porous Ceramics: A Review of Current Achievements and Issues. *Adv. Eng. Mater.* **10**, 155–169 (2008).
21. Bai, H. *et al.* Bioinspired Hydroxyapatite/Poly(methyl methacrylate) Composite with a Nacre-Mimetic Architecture by a Bidirectional Freezing Method. *Adv. Mater.* **28**, 50–56 (2015).
22. Fukasawa, T., Deng, Z.-Y., Ando, M., Ohji, T. & Goto, Y. Pore structure of porous ceramics synthesized from water-based slurry by freeze-dry process. *J. Mater. Sci.* **36**, 2523–2527 (2001).
23. Fukasawa, T., Ando, M., Ohji, T. & Kanzaki, S. Synthesis of Porous Ceramics with Complex Pore Structure by Freeze-Dry Processing. *J. Am. Ceram. Soc.* **84**, 230–232 (2001).
24. Lloyd, D. J. Particle reinforced aluminium and magnesium matrix composites. *Int. Mater. Rev.* **39**, 1–23 (1994).
25. Launey, M. E. *et al.* A novel biomimetic approach to the design of high-performance ceramic–metal composites. *J. R. Soc. Interface R. Soc.* **7**, 741–753 (2010).

26. Roy, S. & Wanner, A. Metal/ceramic composites from freeze-cast ceramic preforms: Domain structure and elastic properties. *Recent Adv. Exp. Appl. Res. Compos. Mater.* **68**, 1136–1143 (2008).
27. Garcia-Cordovilla, C., Louis, E. & Narciso, J. Pressure infiltration of packed ceramic particulates by liquid metals. *Acta Mater.* **47**, 4461–4479 (1999).
28. Mattern, A. *et al.* Preparation of interpenetrating ceramic–metal composites. *Eng. Ceram. 2003* **24**, 3399–3408 (2004).
29. Ferraro, C. *et al.* Strong and tough metal/ceramic micro-laminates. *Acta Mater.* **144**, 202–215 (2018).
30. Schroers, J., Samwer, K., Szuecs, F. & Johnson, W. L. Characterization of the Interface Between the Bulk Glass Forming Alloy Zr41Ti14Cu12Ni10Be23 with Pure Metals and Ceramics. *J. Mater. Res.* **15**, 1617–1621 (2011).
31. Shen, P., Zheng, X.-H., Lin, Q.-L., Zhang, D. & Jiang, Q.-C. Wetting of Polycrystalline α-Al2O3 by Molten Zr55Cu30Al10Ni5 Metallic Glass Alloy. *Metall. Mater. Trans. A* **40**, 444–449 (2009).
32. Kai, W. *et al.* Air oxidation of a Zr58Cu22Al12Fe8 bulk metallic glass at 350–550°C. *14th Int. Symp. Metastable Nano-Mater. ISMANAM-2007* **483**, 519–525 (2009).
33. Löffler, J. F. Bulk metallic glasses. *Intermetallics* **11**, 529–540 (2003).
34. Dandliker, R. B., Conner, R. D. & Johnson, W. L. Melt infiltration casting of bulk metallic-glass matrix composites. *J. Mater. Res.* **13**, 2896–2901 (1998).
35. Choi-Yim, H., Schroers, J. & Johnson, W. L. Microstructures and mechanical properties of tungsten wire/particle reinforced Zr57Nb5Al10Cu15.4Ni12.6 metallic glass matrix composites. *Appl. Phys. Lett.* **80**, 1906–1908 (2002).
36. Travitzky, N. Processing of ceramic-metal composites. *Adv. Appl. Ceram.* **111**, 286–300 (2012).
37. Locatelli, M. R., Tomsia, A. P., Nakashima, K., Dalgleish, B. J. & Glaeser, A. M. New strategies for joining ceramics for high-temperature applications. in *Key Engineering Materials* **111**, 157–190 (Trans Tech Publ, 1995).
38. Shen, X., Jing, M., Li, W. & Li, D. Fabrication of Fe-, Ni- and FeNi-coated Al2O3 core-shell microspheres by heterogeneous precipitation. *Powder Technol.* **160**, 229–233 (2005).

39. Xu, Z. *et al.* Bioinspired Nacre-Like Ceramic with Nickel Inclusions Fabricated by Electroless Plating and Spark Plasma Sintering. *Adv. Eng. Mater.* **20**, 1700782 (2018).
40. Gupta, T. K., Lange, F. F. & Bechtold, J. H. Effect of stress-induced phase transformation on the properties of polycrystalline zirconia containing metastable tetragonal phase. *J. Mater. Sci.* **13**, 1464–1470 (1978).
41. Currey, J. D. Mechanical Properties of Mother of Pearl in Tension. *Proc. R. Soc. B Biol. Sci.* **196**, 443–463 (1977).
42. Barthelat, F. Nacre from mollusk shells: a model for high-performance structural materials. *Bioinspir. Biomim.* **5**, 035001–035001 (2010).
43. Espinosa, H. D. & Barthelat, F. Nacre composites, methods of synthesis, and methods of use. *US Patent US8067078B1* (2012).
44. Corni, I. *et al.* A review of experimental techniques to produce a nacre-like structure. *Bioinspir. Biomim.* **7**, 031001–031001 (2012).
45. Wegst, U. G. K., Schecter, M., Donius, A. E. & Hunger, P. M. Biomaterials by freeze casting. *Philos. Trans. R. Soc. Lond. Math. Phys. Eng. Sci.* **368**, 2099–2121 (2010).
46. Michaud, V. & Mortensen, A. Infiltration processing of fibre reinforced composites: governing phenomena. *Compos. Part Appl. Sci. Manuf.* **32**, 981–996 (2001).
47. Michaud, V. & Mortensen, A. On measuring wettability in infiltration processing. *Scr. Mater.* **56**, 859–862 (2007).
48. The Theory of Infiltration: 1. the Infiltration Equation and... : Soil Science. Available at: http://journals.lww.com/soilsci/Fulltext/1957/05000/The_Theory_of_Infiltration__1__the_Infiltration.2.aspx. (Accessed: 12th May 2014)
49. Suresh, S., Mortensen, A. & Needleman, A. *Fundamentals of Metal-Matrix Composites*.
50. Li, J.-G. Wetting and Interfacial Bonding of Metals with Ionocovalent Oxides. *J. Am. Ceram. Soc.* **75**, 3118–3126 (1992).
51. Lou, H. B. *et al.* 73 mm-diameter bulk metallic glass rod by copper mould casting. *Appl. Phys. Lett.* **99**, 051910 (2011).
52. Ishikawa, T., Paradis, P.-F. & Yoda, S. Noncontact surface tension and viscosity measurements of rhenium in the liquid and undercooled states. *Appl. Phys. Lett.* **85**, 5866–5868 (2004).

53. Schmitz, J., Brillo, J. & Egry, I. Surface tension of liquid Cu and anisotropy of its wetting of sapphire. *J. Mater. Sci.* **45**, 2144–2149 (2010).
54. Wurster, S., Motz, C. & Pippan, R. Characterization of the fracture toughness of micro-sized tungsten single crystal notched specimens. *Philos. Mag.* **92**, 1803–1825 (2012).
55. ASTM Standard E1820 *Standard Test Method for Measurement of Fracture Toughness*. (ASTM International, 2016).
56. Mauro, N. A., Blodgett, M., Johnson, M. L., Vogt, A. J. & Kelton, K. F. A structural signature of liquid fragility. *Nat. Commun.* **5**, 4616 (2014).
57. Wadhwa, P., Heinrich, J. & Busch, R. Processing of copper fiber-reinforced Zr41.2Ti13.8Cu12.5Ni10.0Be22.5 bulk metallic glass composites. *Scr. Mater.* **56**, 73–76 (2007).
58. Lee, J. I., Kim, S. Y. & Park, E. S. In-situ synthesis and mechanical properties of Zr-based bulk metallic glass matrix composites manipulated by nitrogen additions. *Intermetallics* **91**, 70–77 (2017).
59. Mukherjee, S., Johnson, W. L. & Rhim, W. K. Noncontact measurement of high-temperature surface tension and viscosity of bulk metallic glass-forming alloys using the drop oscillation technique. *Appl. Phys. Lett.* **86**, 014104 (2004).
60. Keene, B. J. Review of data for the surface tension of pure metals. *Int. Mater. Rev.* **38**, 157–192 (1993).
61. Saiz, E., Cannon, R. M. & Tomsia, A. P. High-Temperature Wetting and the Work of Adhesion in Metal/Oxide Systems. *Annu. Rev. Mater. Res.* **38**, 197–226 (2008).
62. Ahn, K. J., Seferis, J. C. & Berg, J. C. Simultaneous measurements of permeability and capillary pressure of thermosetting matrices in woven fabric reinforcements. *Polym. Compos.* **12**, 146–152 (1991).
63. Mukherjee, S., Schroers, J., Zhou, Z., Johnson, W. . & Rhim, W.-K. Viscosity and specific volume of bulk metallic glass-forming alloys and their correlation with glass forming ability. *Acta Mater.* **52**, 3689–3695 (2004).
64. Molina, J. *et al.* Pressure infiltration of liquid aluminium into packed SiC particulate with a bimodal size distribution. *Acta Mater.* **50**, 247–257 (2002).

65. Rodríguez-Guerrero, A., Narciso, J., Louis, E. & Rodríguez-Reinoso, F. Decreasing the infiltration threshold pressure of Al–12wt% Si into alumina particle compacts by Sn or Pb layers. *Compos. Sci. Technol.* **68**, 75–79 (2008).
66. Mayer, G. Rigid Biological Systems as Models for Synthetic Composites. *Science* **310**, 1144 (2005).
67. Srinivasa Rao, B. & Jayaram, V. Pressureless infiltration of Al–Mg based alloys into Al2O3 preforms: mechanisms and phenomenology. *Acta Mater.* **49**, 2373–2385 (2001).
68. Saiz, E., Cannon, R. M. & Tomsia, A. P. Reactive spreading: adsorption, ridging and compound formation. *Acta Mater.* **48**, 4449–4462 (2000).
69. Ryu, C. W., Kang, D. H., Jeon, S., Lee, G. W. & Park, E. S. Accurate quantification of glass-forming ability by measuring effective volume relaxation of supercooled melt. *APL Mater.* **5**, 106103 (2017).
70. Hofmann, D. C. *et al.* Designing metallic glass matrix composites with high toughness and tensile ductility. *Nature* **451**, 1085–1089 (2008).
71. Wilkerson, R. P. *et al.* A Novel Approach to Developing Biomimetic ("Nacre-Like") Metal-Compliant-Phase (Nickel–Alumina) Ceramics through Coextrusion. *Adv. Mater.* **28**, 10061–10067 (2016).
72. Bai, H., Polini, A., Delattre, B. & Tomsia, A. P. Thermoresponsive composite hydrogels with aligned macroporous structure by ice-templated assembly. *Chem. Mater. Publ. Am. Chem. Soc.* **25**, 4551–4556 (2013).
73. Bai, H., Chen, Y., Delattre, B., Tomsia A.P. & Ritchie, R.O. Bioinspired large-scale aligned porous materials assembled with dual temperature gradients. *Sci. Adv.* **1**, e1500849 (2015).
74. Hunger, P. M., Donius, A. E. & Wegst, U. G. K. Platelets self-assemble into porous nacre during freeze casting. *J. Mech. Behav. Biomed. Mater.* **19**, 87–93 (2013).
75. Porter, M. M., McKittrick, J. & Meyers, M. A. Biomimetic Materials by Freeze Casting. *JOM* **65**, 720–727 (2013).
76. Das, P. *et al.* Nacre-mimetics with synthetic nanoclays up to ultrahigh aspect ratios. *Nat. Commun.* **6**, 5967 (2015).
77. Libanori, R., Erb, R. M. & Studart, A. R. Mechanics of Platelet-Reinforced Composites Assembled Using Mechanical and Magnetic Stimuli. *ACS Appl. Mater. Interfaces* **5**, 10794–10805 (2013).

78. Bonderer, L. J., Studart, A. R. & Gauckler, L. J. Bioinspired Design and Assembly of Platelet Reinforced Polymer Films. *Science* **319**, 1069–1073 (2008).
79. Erb, R. M., Libanori, R., Rothfuchs, N. & Studart, A. R. Composites Reinforced in Three Dimensions by Using Low Magnetic Fields. *Science* **335**, 199–204 (2012).
81. ASTM D790 *Standard Test Methods for Flexural Properties of Unreinforced and Reinforced Plastics and Electrical Insulating Materials*. (ASTM International, 2017).
82. Gonzalez, E. J. & Trumble, K. P. Spontaneous Infiltration of Alumina by Copper-Oxygen Alloys. *J. Am. Ceram. Soc.* **79**, 114–120 (1996).
83. Barham, N. L., Kaplan, W. D. & Rittel, D. Static and dynamic mechanical properties of alumina reinforced with sub-micron Ni particles. *Mater. Sci. Eng. A* **597**, 1–9 (2014).
84. Lawn, B. R., Freiman, S. W., Baker, T. L., Cobb, D. D. & Gonzalez, A. C. Study of Microstructural Effects in the Strength of Alumina Using Controlled Flaws. *J. Am. Ceram. Soc.* **67**, c67–c69 (1984).
85. Kruzic, J. J., Cannon, R. M. & Ritchie, R. O. Effects of Moisture on Grain-Boundary Strength, Fracture, and Fatigue Properties of Alumina. *J. Am. Ceram. Soc.* **88**, 2236–2245 (2005).
86. Ferrand, H. L., Bouville, F., Niebel, T. P. & Studart, A. R. Magnetically assisted slip casting of bioinspired heterogeneous composites. *Nat. Mater.* **14**, 1172–1179 (2015).
87. Kruzic, J. J., Cannon, R. M. & Ritchie, R. O. Effects of Moisture on Grain-Boundary Strength, Fracture, and Fatigue Properties of Alumina. *J. Am. Ceram. Soc.* **88**, 2236–2245 (2005).
88. Wilkerson, R. P. *et al.* A study of size effects in bioinspired, “nacre-like”, metal-compliant-phase (nickel-alumina) coextruded ceramics. *Acta Mater.* **148**, 147–155 (2018).